Ordering and Fluctuations
in Smectic Membranes

Ordering and Fluctuations in Smectic Membranes

Proefschrift

ter verkrijging van de graad van doctor aan de
Technische Universiteit Eindhoven, op gezag van de
Rector Magnificus prof.dr. R.A. van Santen, voor een
commissie aangewezen door het College voor
Promoties in het openbaar te verdedigen
op woensdag 12 december 2001 om 16.00 uur

door

Andrea Fera

geboren te Cagliari, Italië
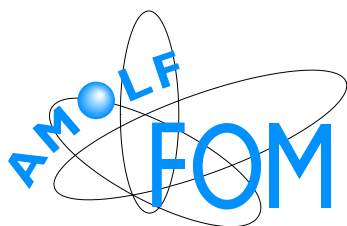
Dit proefschrift is goedgekeurd door de promotoren:

prof.dr.ir. W. H. de Jeu

en

prof.dr. D. Frenkel

Non per un Dio, ma nemmeno per gioco
Fabrizio de André

Era un mondo adulto... si sbagliava da professionisti!
Paolo Conte

This thesis is based on the following articles.

Chapter 3:

D. Sentenac, A.N. Shalaginov, A. Fera, and W.H. de Jeu, *On the instrumental resolution in x-ray reflectivity experiments*,
J. of Appl. Crystall. **33**, 130 (2000).

D. Sentenac, A. Fera, R. Opitz, B.I. Ostrovskii, O. Bunk, and W.H. de Jeu, *X-ray scattering from freely suspended smectic films: resolution and other effects*,
Physica B **283**, 232 (2000).

Chapter 4:

A. Fera, I.P. Dolbnya, R. Opitz, B.I. Ostrovskii, and W.H. de Jeu, *Crystalline smectic B films as fluctuating systems: static and dynamic x-ray scattering*,
Phys. Rev. E **63**, R020601 (2001).

Chapter 5:

A. Fera, B.I. Ostrovskii, D. Sentenac, I. Samoilenko, and W.H. de Jeu, *Layer-by-layer crystallization and the role of fluctuations in free standing smectic films*,
Phys. Rev. E **60**, R5033 (1999).

Chapter 6:

A. Fera, I.P. Dolbnya, G. Grübel, H.G. Muller, B.I. Ostrovskii, A.N. Shalaginov, and W.H. de Jeu, *Complex Dynamic behaviour of fluctuating smectic-A films as studied by scattering with coherent x-rays*,
Phys. Rev. Lett. **85**, 2316 (2000).

I. Sikharulidze, I.P. Dolbnya, A. Fera, A. Madsen, B.I. Ostrovskii, and W.H. de Jeu, *Smectic membranes in motion: approaching the fast limits of x-ray photon correlation spectroscopy*,
Phys. Rev. Lett. *submitted*.

Other publications:

A. Fera, R. Opitz, W.H. de Jeu, B.I. Ostrovskii, D. Schlauf, and C. Bahr, *Structure of freely suspended chiral smectic films as determined by x-ray reflectivity and optical ellipsometry*,
Phys. Rev. E **64**, 021702 (2001).

Contents

Chapter 1

Introduction

In this chapter we introduce the liquid crystal phases and the samples used for the experiments described in this thesis. Basic aspects of surface ordering and fluctuations are introduced, including the influence of interfaces, which play an important role in smectic membranes. In the last paragraph the main experimental achievements are summarized.

1.1 Liquid crystals

In a molecular crystal in general the molecules possess both *orientational* and *positional* order. The centers of mass are constrained to occupy specific sites on a lattice, while the molecular axes point in specific directions. In this situation, the positional as well as the orientational correlation function of the molecules approach a constant in the limit of infinite separation. This can be contrasted with a liquid in which the molecules diffuse randomly with their molecular axes tumbling. In that situation the orientational and positional order decay exponentially, with a range of typically few molecular diameters. When a fully ordered molecular crystal is heated, at the melting point the long-range orientational and positional order is lost and the isotropic liquid is obtained. Liquid crystal phases, as the name already suggests, possess mechanical and symmetry properties intermediate between solids and liquids. In this thesis the focus is on *thermotropic* liquid crystalline phases [1–3]. They are formed by melting specific organic molecular crystals that do not undergo a direct transformation to a liquid; instead they pass through intermediate states called *mesomorphic* or *liquid crystalline* phases. Molecules that show stable mesomorphic states over a certain temperature range are anisotropic, either
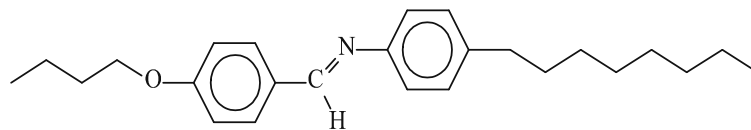
K 33 CrB 48.5 SmA 63.5 N 78 I

Figure 1.1: *Structural formula and phase transition temperatures of 4O.8.*

Constant	d (nm)	B (N/m^2)	K (N)	γ (N/m)	C$_{44}$ (N/m^2)	η_3 (kg/(m·s))
Value	2.85	10^7	$2.5 \cdot 10^{-11}$	0.020 [4]	$1.0 \cdot 10^5$ [5]	0.039 [6]

Table 1.1: *Material constants of 4O.8.*

elongated or disc-like. In this thesis only liquid crystal phases formed by elongated molecules are considered. These molecules (also known as *calamitic* liquid crystals) possess a rigid core, usually but not necessarily aromatic, and often flexible tails. They are typically $2-4$ nm long and $0.3-0.6$ nm wide. As an example we can take the compound abbreviated as 4O.8, which plays a central role in this thesis (see fig. 1.1).

The main subdivision of thermotropic liquid crystals is into *nematic* and *smectic* mesophases (see fig. 1.2). In the nematic phase the centers of mass of the molecules are randomly distributed but on average the molecules are aligned with their long axes parallel to each other, leading to a preferred direction in space. In this sense one can truly speak of an anisotropic liquid. The (local) direction of alignment is described at each point by a unit vector **n**, called the director. The direction of **n** is arbitrary and in practice imposed by external constraints such as external fields or surfaces. The positional correlation of the centers of mass of the molecules decays in liquid-like fashion, but the associated correlation length differs in the directions parallel ($\parallel$) and perpendicular ($\perp$) to **n**: $\zeta_\parallel \neq \zeta_\perp$. The director is (usually) an axis of uniaxial symmetry. Moreover **n** and $-$**n** are equivalent, which means that asymmetric molecules have the same probability to point their heads up or down. Finally in the nematic phase the molecules must be achiral, or if not, the system must be racemic. Optically active molecules give rise to additional chiral ordering, leading to the chiral nematic (or cholesteric) phase, which has a helical structure. Such molecules are not considered in this thesis.

Smectic phases have not only nematic-like orientational order but also positional order in at
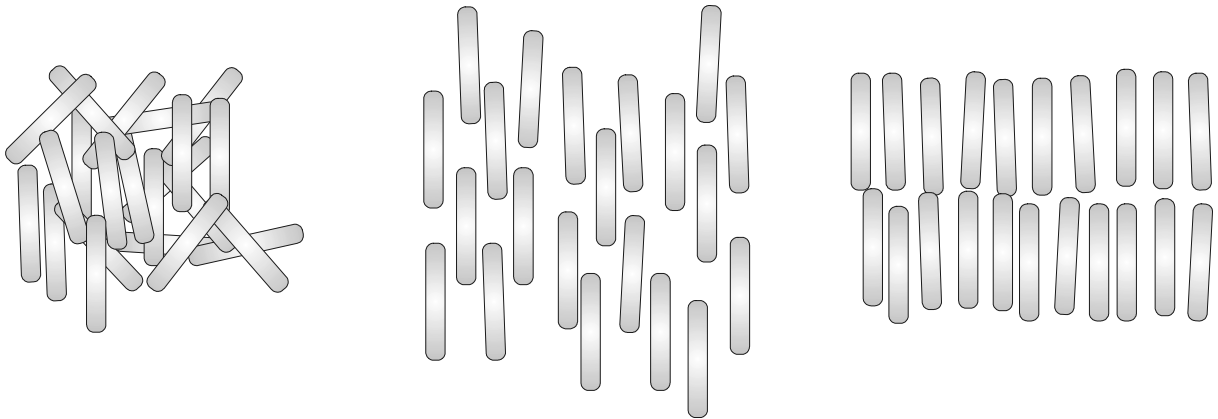
Figure 1.2: *Schematic representation of the molecular arrangements in liquid crystals. From the left: the isotropic (liquid) phase, the nematic phase and the smectic A phase. For simplicity the elongated molecules are represented as cylinders.*

least one direction: the centers of mass of the molecules are (on average) arranged in equidistant planes. This is the common aspect of the various types of smectic phases, that are mutually distinguished by further additional ordering. The layer structure is, in general, very loose: the molecules have an appreciable probability of deviating from their equilibrium positions. Smectic phases can occur when a nematic phase is cooled or they can be formed directly from the isotropic liquid. The different types of smectic phases are indicated as SmA, SmB,..., SmI. They can be divided into two classes that differ in the orientation of **n** with respect to the layer normal: orthogonal and tilted smectic phases. In addition some organization of the centers of mass of the molecules within the layers can occur. In the following the description will be restricted to the orthogonal smectic phases relevant to this thesis.

The simplest orthogonal smectic phase, the smectic A (SmA), consists of stacks of two-dimensional (2D) liquid layers (see fig. 1.2). The director is perpendicular to the layers and defines the *z*-direction. Analogously to the nematic phase, in the SmA phase long-range orientational order exists along **n**, with additional positional order. The smectic layers have no long-range ordering (liquid-like). Like for nematics the orientation of **n** (and thus of the layers) is imposed by external conditions.

Cooling down a SmA phase, a smectic B phase can occur. The smectic B phase is characterized by a limited positional order and long-range bond-orientational order. Locally the
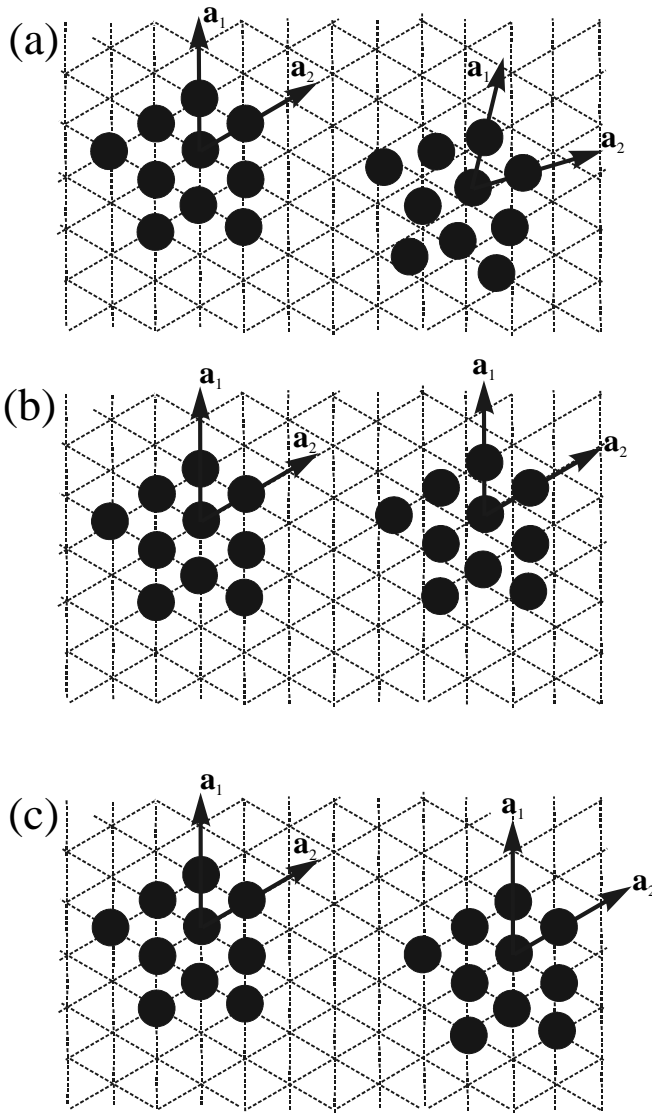
Figure 1.3: *Top view of the molecular arrangement in a smectic layer.*

(a) *Smectic A phase: the molecules form clusters with short-range positional and orientational order.*

(b) *Smectic B phase: the molecules possess still short-range positional order, but there is long-range bond-orientational order, i.e. the clusters conserve the orientation of the lattice vectors.*

(c): *Crystalline B phase. The molecules occupy equilibrium positions on the lattice (long-range positional order).*

centers of mass of the molecules are organized in clusters, which have a triangular lattice in the plane of the layers (see fig. 1.3). The positional correlation length is limited, of the order of ~ 10 nm. However, the orientations of the clusters possess long-range ordering, which is called bond-orientational order. The clusters diffuse in a liquid-like fashion within the layers. This phase is also known in the literature as the hexatic B phase.

Finally, upon cooling down the hexatic phase a solid phase may appear, in which the translational freedom of the clusters is absent (see fig. 1.3). This crystalline B phase is a truly 3D crystalline phase with long-range positional and orientational correlations in and between the layers [7]. The coupling between the crystalline layers is nevertheless very weak as indicated by
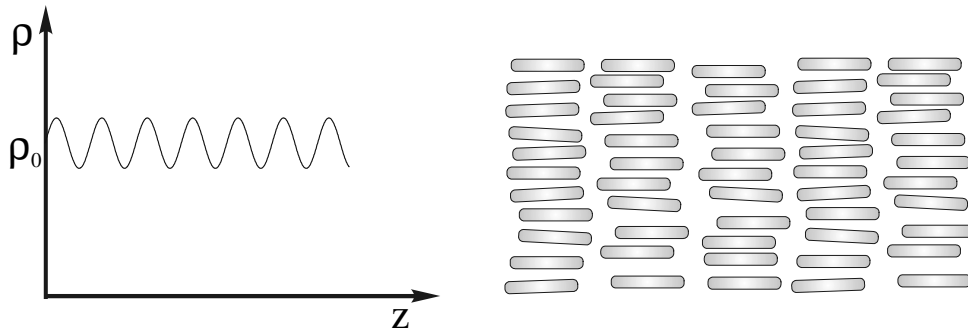
Figure 1.4: *Schematic representation of the smectic layers and the corresponding (electron) density projected along the z-axis.*

the low intensity of the corresponding x-ray reflections. Furthermore the shear elastic constant between the layers, C_{44}, is approximately two orders of magnitude smaller than the other elastic constants [5, 8].

1.2 Smectic ordering

In SmA liquid crystals the molecules are aligned along the normal to the layers, which we define as the z-axis. The centers of mass of the molecules move around their equilibrium positions in the one-dimensional lattice, and in a first approximation the density along z can be pictured as a sinusoidal wave, see fig. 1.4. It is important to realize that while we speak in a loose way about smectic layers, in fact there is not more than a weak density modulation [2, 3]. The average deviation from the equilibrium position can be described by a distribution function $f(z)$ of the centers of mass of the molecules. Expanding $f(z)$ in a Fourier series we obtain [9]:

$$f(z) = \frac{2}{d} \sum_{n=0}^{\infty} \tau_n \cos(nq_0 z) \quad , \tag{1.1}$$

in which d is the smectic layer spacing, $n = 1, 2, 3 \cdots$ and $q_0 = 2\pi/d$. The τ_n are the smectic order parameters defined as [10]

$$\tau_n = \langle \cos(nq_0 z) \rangle. \tag{1.2}$$

The lowest order smectic parameter τ_1 is related to the amplitude of the mass density wave in fig. 1.4. It is usually called *the* smectic order parameter. The higher order parameters τ_n indicate the deviation from a sinusoidal shape of the density modulation.
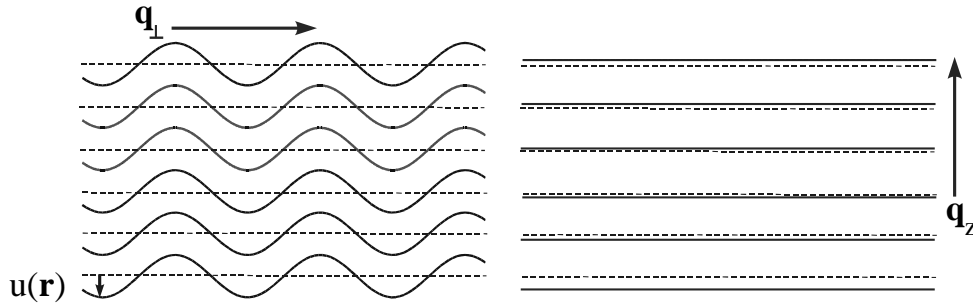
Figure 1.5: *Schematic representation of bending (left) and compression (right) of the smectic layers. The broken lines represent the equilibrium positions of the layers. $u(\mathbf{r})$ is the displacement from the equilibrium position. For each case the corresponding wave-vector is shown, for which $q_i = |\mathbf{q}_i| = 2\pi/\lambda_i$, with $i = \perp, z$ and λ_i representing the wavelength of the fluctuation.*

An x-ray scattering experiment probes the (electron) density modulation along a specific direction in space (see ch. 2). Because of the layered structure, in smectics the intensity scattered along the z-axis in the reciprocal space shows Bragg-like peaks [1, 11]. The intensity of the first Bragg peak is proportional to $|\tau_1|^2$ [9]. An analogous relation can be given for $|\tau_2|^2$ and the second-order Bragg peak. Hence the intensity ratio of the second to the first-order Bragg peaks gives in principle a direct indication of the deviation of the density modulation from a sinusoidal shape.

1.3   Smectic fluctuations

In a continuous approach the smectic phase can be described as a stack of two-dimensional (2D) layers. The layers can slide freely with respect to each other [2]. Their fluctuations can be described by two elastic constants, one for compression (B) and one for bending (K) of the layers. These modes of fluctuation are shown in fig. 1.5. A compressional mode changes the smectic layer spacing and can be considered as a "real" elasticity: the associated elastic constant is large (see tab. 1.1). The associated wave vector is directed along the layer normal; hence its maximum value is $2\pi/L$, where L is the sample thickness. A bending mode fluctuates in the plane of the layers. It conserves the layer spacing and its maximum wavelength is the lateral dimension of the sample. In a bulk sample the fluctuations are not limited by boundary conditions. Hence the undulations will not be conformal through the sample and necessarily

couple to the compressional modes.

The thermally excited fluctuations of smectic A can be described by the Landau-de Gennes theory. As a final result the average squared displacement of the layers from their equilibrium position $\langle u^2(\mathbf{r}) \rangle$ diverges logarithmically with the sample size L (Landau-Peierls instability):

$$\langle u^2(\mathbf{r}) \rangle \sim \frac{T}{\sqrt{KB}} \ln\left(\frac{L}{d}\right). \qquad (1.3)$$

Hence for $L \to \infty$ the long-range order of the smectic A density modulation is destroyed by the thermal fluctuations. This will be discussed in some detail in sec. 4.2.1.

The (slow) logarithmic divergence of thermal fluctuations is typical for a certain class of low-dimensional systems at their so-called marginal dimensionality. A typical example is a two-dimensional solid. The smectic A phase is a 1D ordered system in 3D space, which has similar characteristics. Such systems due not posses true long-range order; instead the positional correlation decays algebraically with the distance r as $r^{-\eta}$ (η is small and positive) [2, 3]. The associated density-density correlation function can be studied by x-ray scattering. The scattered intensity of a true crystal shows δ-function type Bragg peaks with diffuse tails due to the Debye-Waller broadening. Instead, for smectic systems only singularities are observed in the x-ray intensity, which are the signature of an algebraically decaying distribution [12, 13].

1.4 Free Surfaces and ordering

In liquid crystals a free surface often stabilizes a higher ordered phase that is either observed in the bulk at lower temperatures or not observed in the bulk at all. Such surface induced *ordering* can be contrasted to surface melting, which corresponds to surface *disorder* [14]. Outside the field of liquid crystals surface ordering has also been found in linear alkanes and alcohols [15–17]. Naively one would expect a free surface to be more disordered than the bulk material, due to the breaking of molecular bonds at the interface ("missing neighbor" effect). However, microscopic interactions close to the surface may be quite different from those in the bulk. As a result, the surface may order before the bulk, or may even exhibit ordering phenomena of a different type than the bulk material. Examples can be found in many types of liquid crystal. At temperatures somewhat above a nematic-SmA transition usually smectic layers are formed at a free surface [18, 19]. Upon approaching the SmA phase from the high-temperature isotropic phase, either a finite number of successive layering transitions [20] or a continuous growth of

the surface SmA phase occurs [21, 22]. In the case of a SmA-SmC transition a free surface usually induces a tilt, causing the SmC phase to grow continuously from the surface into the SmA interior of the film as the bulk transition temperature is approached from above [23] . In ch.5 we shall discuss in detail the case of crystallization (CrB) starting at the outermost layers of a SmA membrane and proceeding in a layer-by-layer fashion inwards [24, 25].

Also when no higher-ordered phase is stabilized, a surface will have its effect on the smectic A phase. To discuss this point we can follow the approaches from the two previous sections. Starting from the smectic distribution function (eq. 1.1), one would intuitively expect the distribution to narrow upon approaching the surface. The centers of mass of the molecules nearest to the surface will have an increased tendency to be located in the center of the first smectic layer. This would correspond to an increase in the smectic order parameter. So far no full theoretical description of these effects has been given. However, smectic order parameter profiles with an increased value at the surface have been postulated in several cases to explain experiments [26, 27].

The free surface has been taken into account in the Landau-de Gennes theory by extending the bulk free energy with surface terms that depend on the surface tension (γ) [28]. As a result the bulk fluctuations can be either damped or enhanced. In this context a parameter ν has been defined that described the competition between bulk elasticity and surface tension:

$$\nu = \frac{\gamma}{\sqrt{BK}} \quad .$$
(1.4)

When $\nu > 1$, the fluctuations at a surface are quenched, while surface enhanced fluctuations occur for $\nu < 1$. Both situations have been observed experimentally in SmA membranes [25, 29, 30].

1.5   Smectic membranes

Due to their layered structure, smectic A phases can be freely suspended over an aperture in a frame, similar to the soap bubbles. In such a film the smectic layers align parallel to the two free surfaces and the film is flattened due to the surface tension, which minimizes the surface area of the film. Freely suspended films can be considered as *smectic membranes* consisting of stacks of smectic layers. This property of smectic mesophases has been known since the beginning of the last century and was used in ref. [31] as an argument for the existence of

layers in smectic liquid crystals. However, only in the 1970s smectic membranes found an extensive usage in experimental studies [32]. They can be made as thin as two layers up to thousands of layers. The interest in thin films of molecular size was primarily motivated by the fact that they provide model systems to study the effects of reduced dimensionality on phase transitions and fluctuations, and interfacial phenomena. X-ray diffraction studies of the melting of thin smectic membranes at the SmB-SmA transition showed that the SmB phase of the compound 4O.8 has three-dimensional long-range positional order and therefore is a true crystalline phase [8]. Somewhat later an hexatic SmB phase was observed in thick films of the compound abbreviated as 65OBC, which shows the characteristic diffraction pattern of six diffuse-like arched maxima [33]. Also the shear modulus was found to vanish in this phase. A whole series of subsequent measurements of smectic membranes has unambiguously identified the hexatic phase as a state of matter [34].

These findings have triggered off numerous structural, calorimetric, optical and mechanical studies of smectic membranes, that have been crucial to our current understanding of liquid crystalline phase behavior. This made it possible to address important issues in condensed matter physics like three- to two-dimensional crossover, melting in two dimensions, fluctuation phenomena at the critical dimensionality, multicriticality, surface ordering, etc. A key issue is the thickness dependence of smectic phase diagrams. In smectic membranes the thickness of the film comes into play as an additional parameter, expanding the richness of the bulk liquid crystal phase diagrams [32,34]. There are numerous reports of the surface enhanced ordering in smectic membranes discussed in the previous section. The surface ordered domain can penetrate either continuously into the film or in a layer-by-layer fashion, thus reflecting differences in the interfacial interactions.

Important questions about the stability of smectic membranes were first extensively addressed in ref. [35]. In this work it is stressed that smectic membranes can exchange matter with the meniscus, which connects the film to the frame and acts as a reservoir. From this point of view, the meniscus plays an important role of fixing the chemical potential (or the pressure) in the film. Additionally there is an effective attractive interaction between the free surfaces, that stabilizes smectic ordering in the films heated above the bulk SmA-nematic transition [26, 36]. In this thesis we will exploit smectic membranes as suitable systems to be studied with x-ray reflectivity methods. This allows to address quantitatively several of the questions addressed above.

1.6   This thesis

This thesis presents experimental results on smectic membranes of N-(4-*n*-butoxy-benzi-lidene)-4-*n*-octylaniline, usually abbreviated as 4O.8. Its properties are summarized in tab. 1.1. The outline of the thesis is as follows. Chapter 2 introduces the concepts necessary to understand the x-ray experiments. In chapter 3 the experimental equipment, including the x-ray set-ups, is described and the types of scans performed are introduced. Quantitative analysis requires knowledge of the instrumental resolution function which is also described in some detail. Finally we discuss the box-model used in the analysis of the specular reflectivity data.

Chapter 4 describes results for the time-averaged height-height correlation function of the thermal fluctuations, which has been studied by means of specular and diffuse x-ray reflectivity [37–39]. The diffuse reflectivity results of SmA membranes of thicknesses ranging from six to 80 layers can be satisfactorily described by the Landau-de Gennes theory extended with surface terms. The analysis of the specular results provides a profile of the thermal fluctuations through the membrane, which is more pronounced than predicted by hydrodynamic theory. In order to explain this result, a considerable additional contribution from the local fluctuations has to be assumed. The diffuse reflectivity results for CrB membranes show a spectral dependence rather similar to that of the SmA phase. Conversely, the profile of the thermal fluctuations through the film shows for CrB no dependence on the thickness. These results indicate that CrB membranes fluctuate dynamically rather similarly to SmA ones.

In chapter 5 the layer-by-layer crystallization observed in smectic membranes of 4O.8 is discussed. Specular reflectivity has been used to study the associated thermal fluctuations in 8-layer membranes. Each of the steps is preceded by the formation of an intermediate layer-by-layer with in-plane hexatic ordering. We find an unusually large reduction of the fluctuations after the emergence of only the first hexatic top layer. The fluctuation profiles over the film are in all cases quenched at the surfaces though less so after each crystallization step. This behavior supports theoretical arguments that the hexatic order is reduced by out-of-plane smectic layer fluctuations.

In chapter 6 results are discussed for the time-dependent displacement-displacement correlation function in SmA and CrB membranes as studied by x-ray photon correlation spectroscopy (XPCS). We have demonstrated the feasibility of XPCS experiments with 8 keV x-rays on thin films leading to relaxation times in the microsecond range. For such SmA membranes we re-

solved both an oscillatory and a damping behavior of the correlation function. This can be contrasted with literature results that show only a simple exponential decay in thick films. In agreement with recent models [40], our results indicate that the inertial term in the dynamic equations cannot be disregarded anymore in thin films for which the surface contribution becomes important. In addition the dynamic nature of the CrB fluctuations has been confirmed by XPCS.

Chapter 2

X-ray Scattering

The first part of this chapter focuses on the basic quantities and definitions regarding x-ray reflectivity. Recently, some excellent monographs on x-ray reflectivity have appeared [37–39], which give a complete overview on the subject. Hence here only a short presentation will be given, aimed at understanding the analysis of the experimental data presented in the later chapters. In the next section we will consider the intensity of an x-ray beam reflected at a sharp planar interface. Then an expression will be derived for the intensity of an x-ray beam reflected by a smectic membrane in vacuum following the interactive matrix formalism due to Parratt. In the third section this result will be simplified using the first Born approximation, which leads to an expression that is more convenient from a computational point of view. The fourth section explains how to calculate the reflected intensity from (real) rough interfaces within the first Born approximation. Finally, in the last part of this chapter, x-ray photon correlation spectroscopy will be introduced, which technique has been used to measure the intensity-intensity time autocorrelation function of smectic membranes.

2.1 Reflectivity from a sharp flat interface

First a planar electromagnetic wave propagating in vacuum will be considered incident on a *sharp* interface and reflected back (fig. 2.1) [11]. The incident wave (*i*), the reflected wave (*o*) and the transmitted wave (*t*) must be of the form:

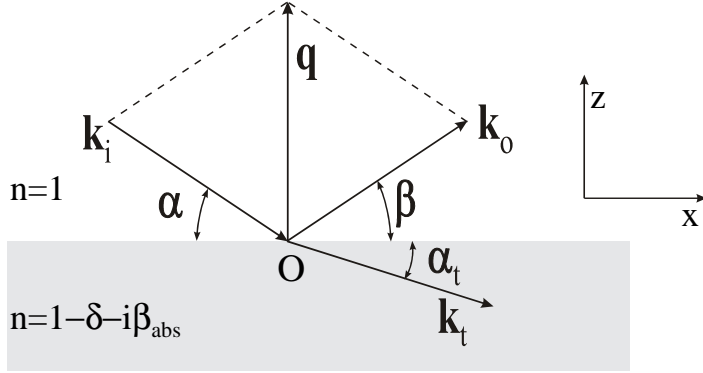$$\Psi_j = A_j \, e^{i\mathbf{k}_j \cdot \mathbf{r}} \tag{2.1}$$

Figure 2.1: *Schematic representation of the scattering of an incoming electromagnetic plane wave at a sharp interface of a material with vacuum.*

where $j = i$, o or t. The wavenumber k_j is related to the wavelength by $\lambda_j = 2\pi/k_j$. Since the refractive index of a material (n) is the ratio between the wavelength of the electromagnetic wave inside that material and in vacuum [11], in the case of elastic scattering it follows that:

$$k = |\mathbf{k}_i| = |\mathbf{k}_o| = \frac{|\mathbf{k}_t|}{n}. \tag{2.2}$$

All the amplitudes A_j have to be such that both Ψ and $\nabla\Psi$ are continuous across the interface. These two conditions may be expressed by:

$$\text{Continuity of } \Psi: \qquad A_i + A_o = A_t, \tag{2.3}$$

$$\text{Continuity of } \nabla\Psi: \qquad A_i\mathbf{k}_i + A_o\mathbf{k}_o = A_t\mathbf{k}_t. \tag{2.4}$$

Writing down explicitly the x and z components of $\mathbf{k}_j$ in eq. 2.4 and inserting them in eq. 2.3 one obtains:

$$\alpha = \beta \quad, \tag{2.5}$$

$$n\cos\alpha_t = \cos\alpha \quad, \tag{2.6}$$

which are known as the Snell-Descartes laws. In the following the so-called specular case will be considered, defined by $\alpha = \beta = \theta$.

The refractive index of a material n is a complex quantity that can be written as [11]:

$$n = 1 - \delta + i\,\beta_{abs}. \tag{2.7}$$

The real part of n depends on the electron density ρ of the material: $\delta = (r_e\rho\lambda^2/2\pi)$, where $r_e = 2.8 \cdot 10^{-6}$ nm (the classical radius of the electron). The imaginary part of n describes the absorption: $\beta_{abs} = \mu\lambda/4\pi$, where μ is the linear absorption coefficient. For all the materials

14

studied in this thesis $\delta \approx 10^{-6}$ and $\beta_{abs} \approx 10^{-8}$, so that the wavelength inside the material is almost indistinguishable from that in vacuum. According to eq. 2.7 $n < 1$, which implies that the incoming radiation will be totally reflected for incident angles smaller than a critical angle θ_c. This angle can be calculated applying the Snell-Descartes' law for $\alpha_t = 0$. Neglecting the absorption term, one obtains:

$$\cos\theta_c = n = 1 - \delta. \tag{2.8}$$

For small angles $\cos\theta_c$ can be approximated by $(1 - \theta_c^2/2)$, and eq. 2.8 becomes:

$$\theta_c \approx \sqrt{2\delta} = \lambda\sqrt{\rho r_e/\pi}. \tag{2.9}$$

Hence the critical angle of a material is a direct measurement of the (average) electron density. For the materials studied in this thesis $\theta_c \approx 0.15°$.

For $\alpha < \theta_c$ the refractive index is purely imaginary. The reflected beam is associated with an evanescent standing wave traveling parallel to the surface inside the material. Such an evanescent wave has an exponentially damped amplitude inward along the surface normal. It can be used to study the structure of a material at the interface [41]. This technique is known as *grazing incidence diffraction*. For $\alpha > \theta_c$ the incoming intensity is divided in three parts: the transmitted wave, the reflected wave and the evanescent wave. The intensity of the evanescent wave decreases exponentially with α: for $\alpha > 3\theta_c$ it becomes negligible [41].

The reflectivity R is given by the ratio of the intensity of the incoming and the reflected wave, respectively. It can be calculated from eq. 2.3 and eq. 2.4 [11, 37]. For small incoming angles (i.e. $\sin\theta \approx \theta$) and an incident wave polarised parallel to the surface R takes the form:

$$R(\theta) = \left|\frac{A_o}{A_i}\right|^2 = \left|\frac{\theta - \sqrt{\theta^2 - \theta_c^2 - 2i\beta_{abs}}}{\theta + \sqrt{\theta^2 - \theta_c^2 - 2i\beta_{abs}}}\right|^2. \tag{2.10}$$

In the same way $T(\theta)$, the ratio between the transmitted and the incoming intensity, can be derived:

$$T(\theta) = \left|\frac{A_t}{A_i}\right|^2 = \left|\frac{2\theta}{\theta + \sqrt{\theta^2 - \theta_c^2 - 2i\beta_{abs}}}\right|^2. \tag{2.11}$$

In fig. 2.2a the influence of β_{abs} on the reflected intensity is shown. One can see that the absorption only plays a role in the vicinity of θ_c. For the materials studied in this thesis β_{abs} is of the order of $\delta/100$.

In order to compare experiments at different wavelengths, the x-ray intensity is usually expressed in terms of the wave-vector transfer $\mathbf{q} = \mathbf{k}_o - \mathbf{k}_i$. For specular reflectivity $\mathbf{k}_i$, $\mathbf{k}_o$ and
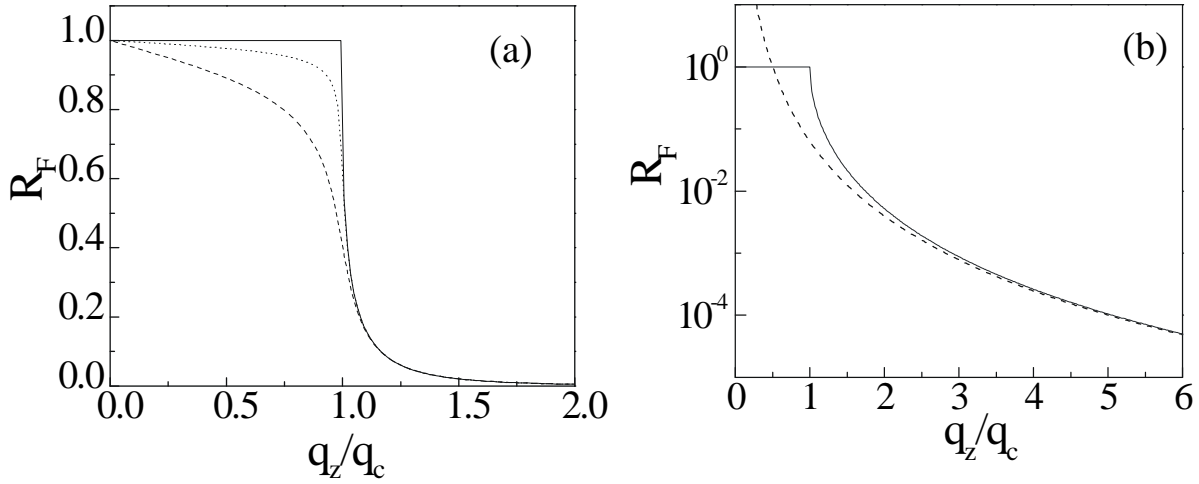
Figure 2.2: *Fresnel reflectivity at a typical soft matter-vacuum interface ($q_c = 0.2$ nm^{-1}) for $\lambda = 0.154$ nm. (a) Effect of the absorption: $\beta_{abs} = 0$ (solid line); $\beta_{abs} = \delta/50$ (dotted line) and $\beta_{abs} = \delta/10$ (broken line). (b) Comparison between the exact result of eq.2.13 (solid line) and the approximated asymptotic behaviour of eq.2.14 (broken line).*

$\mathbf{k}_t$ are in the same plane (the scattering plane), which also contains the surface normal, so that:

$$|\mathbf{q}| \equiv |\mathbf{q}_z| = 2k\sin\theta. \tag{2.12}$$

Neglecting from now on absorption, we can write eq.2.10 as:

$$R(q_z) = \left| \frac{q_z - \sqrt{q_z^2 - q_c^2}}{q_z + \sqrt{q_z^2 - q_c^2}} \right|^2 . \tag{2.13}$$

Eq.2.13 is known as the Fresnel reflectivity of a single sharp interface, usually written as R_F. For $q \gg q_c$, it can be approximated by:

$$R_F = R(q_z) \approx \left(\frac{q_c}{2q_z} \right)^4 = \frac{16\pi^2 \rho^2 r_e^2}{q_z^4} . \tag{2.14}$$

Fig.2.2b shows that the difference between eq.2.10 and the approximated asymptotic behaviour of eq.2.14 becomes important only around q_c.

In a reflectivity experiment the rapid fall-off in intensity as a function of the incoming angle limits the q_z-range that is accessible experimentally. For this reason synchrotron radiation is often used. Then the dynamical range of intensities that can be reached is about 10 orders of magnitude, corresponding to a q_z-range of approximately 10 nm^{-1}. The radiation produced

by a synchrotron is polarised in the plane of the ring. Hence for vertical samples (horizontal scattering plane) eq.2.13 is valid. Part of the experiments reported in this thesis were carried out at the in-house rotating anode set-up, which produces unpolarised Cu-K$_\alpha$ radiation. This requires a polarization correction factor P$= [1 + \cos(2\alpha)]/2$ to be applied to eq.2.13. However, for the small incoming angles accessed experimentally, this value is quite close to 1 (P$= 0.992$ for $\alpha_i = 5°$, the largest angle used). For this reason, P will be neglected in the following.

Eq.2.13 cannot be used directly to interpret the intensity observed from real experiments. There are several reasons for that: (a) the sample surface is never ideally flat; (b) the incoming beam is not perfectly monochromatic; (c) the actual angles are defined only within the instrumental resolution. The surface roughness will be considered in sec.2.4. Effects (b) and (c) can be included in the instrumental resolution function to be discussed in sec.3.4.

2.2 Dynamical matrix formalism

An x-ray beam incident on a surface can penetrate for several micrometers into the material. At each (abrupt) variation of *n* reflection and refraction will occur. In the case of a layered structure or a thin film multiple reflections occur at each interface. A continuous variation of *n* can be conveniently approximated by a series of layers that are assumed to be homogeneous, and treated accordingly. The dynamical matrix formalism, derived by Parratt in 1954, is a recursive approach, which can be used in order to apply eq.2.3 and eq.2.4 systematically. In this section, the results of the dynamical method will be summarized, aiming at understanding the interpretation of the experimental curves presented in the next chapters. A more complete derivation can be found in the original work of Parratt [42] or in one of the recent monographs on x-ray reflectivity [37–39].

Let us consider an x-ray beam incident on a smectic membrane of thickness L in vacuum, fig.2.3. Such a membrane consists of a stack of liquid layers. An x-ray beam impinging on the surface is reflected at each interface, corresponding to a change in the refractive index. At each interface eq.2.3 and eq.2.4 must be satisfied and multiple reflections have to be taken into account. Each layer *j* is defined by its thickness $d_j = z_{j-1} - z_j$ and refractive index $n_j = 1 - \delta_j$. Inside each layer we define A_j^T, the amplitude of the propagating electromagnetic wave, and $q_{z,j}$, the z-component of the wavevector transfer inside that layer. We identify the vacuum surrounding the membrane with layer 1 and layer $N+1$, respectively. The incoming intensity is
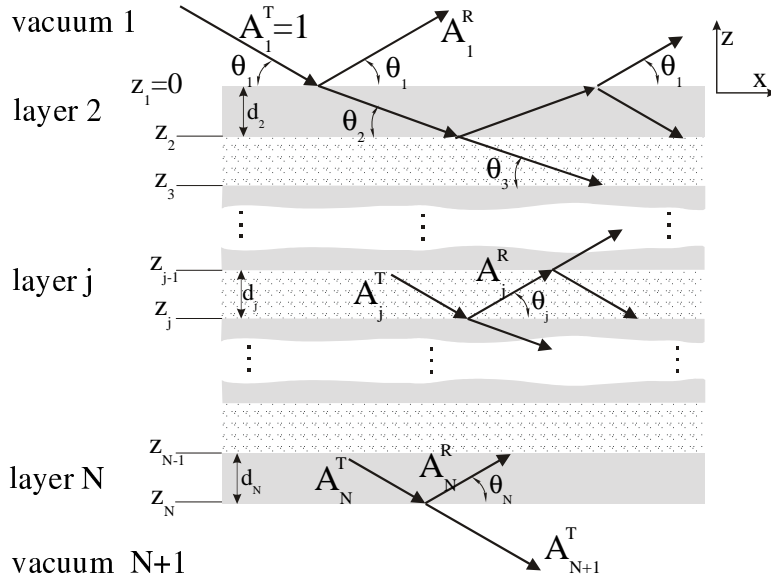
17

Figure 2.3: *Schematic representation of a smectic membrane of $N-1$ layers (i.e. N interfaces) in vacuum. The vacuum surrounding the membrane has been denoted as layer 1 and layer $N+1$. The incident intensity is normalized: $A_1^T = 1$.*

normalized by putting $A_1^T = 1$. A_1^R is the amplitude of the wave reflected back in the vacuum. It results from the coherent superposition of the wave reflected at the first interface with vacuum with the other ones reflected at each interface inside the membrane. These last ones carry the information about the structure of each interface.

For each single layer the Fresnel coefficient $r_{j,j+1}$ can be defined analogously to eq. 2.13:

$$r_{j,j+1} = \frac{q_{z,j} - q_{z,j+1}}{q_{z,j} + q_{z,j+1}}. \tag{2.15}$$

Following [38] one can define X_{j+1} as the ratio between A_{j+1}^R and A_{j+1}^T, so that X_j can be written as:

$$X_j = \frac{A_j^R}{A_j^T} = exp(-iq_{z,j}z_j)\frac{r_{j,j+1} + X_{j+1}exp(iq_{z,j+1}z_j)}{1 + r_{j,j+1}X_{j+1}exp(iq_{z,j+1}z_j)}. \tag{2.16}$$

Because the smectic membrane is considered in vacuum, it follows that $X_{N+1} = 0$. Using this as starting point for the recursion, A_j^R and A_j^T inside all layers can be found. The total reflected intensity is found after iterating N times eq. 2.16:
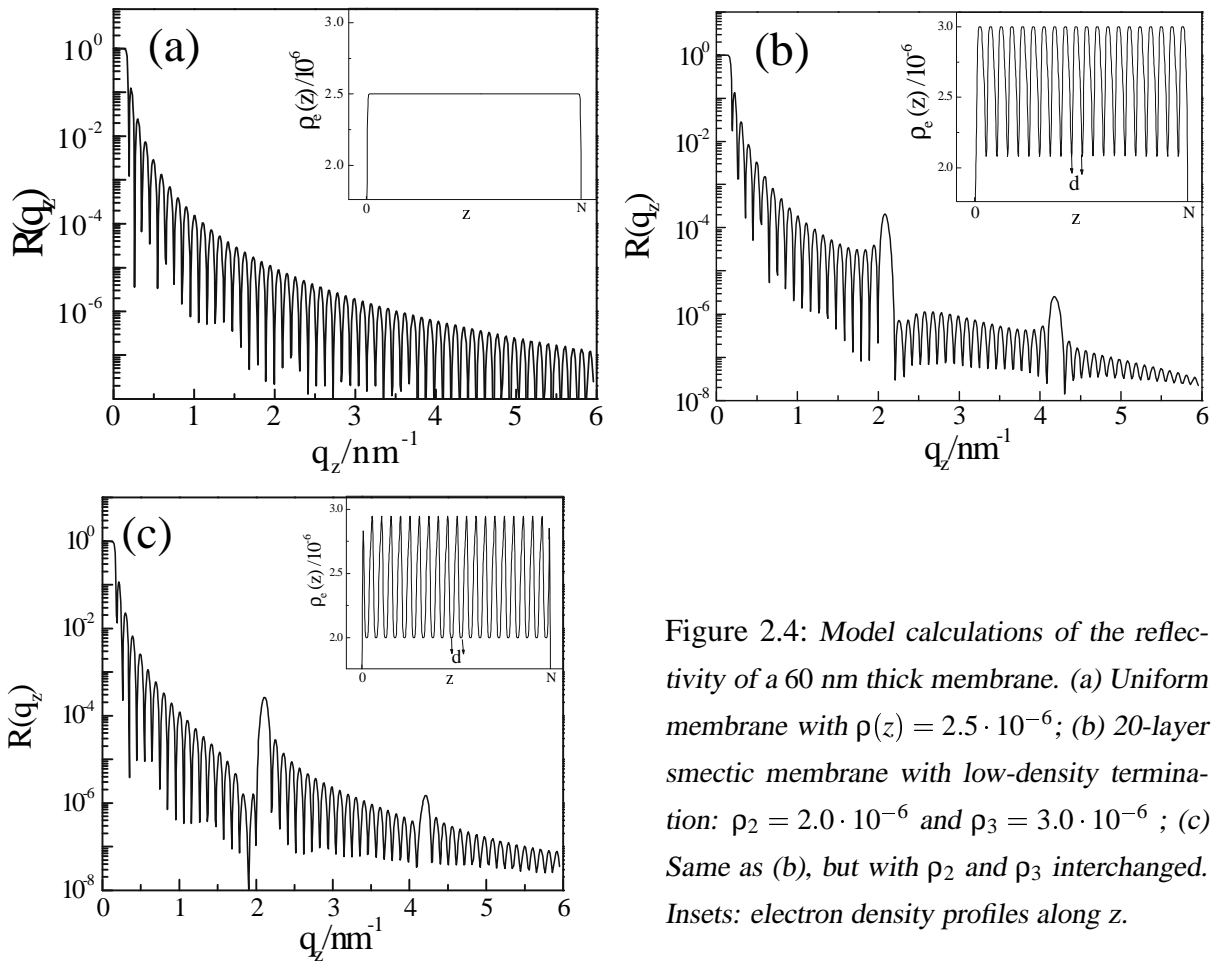
$$R(q_z) = |X_1|^2. \tag{2.17}$$

18

Figure 2.4: *Model calculations of the reflectivity of a* 60 *nm thick membrane. (a) Uniform membrane with* $\rho(z) = 2.5 \cdot 10^{-6}$; *(b) 20-layer smectic membrane with low-density termination:* $\rho_2 = 2.0 \cdot 10^{-6}$ *and* $\rho_3 = 3.0 \cdot 10^{-6}$; *(c) Same as (b), but with* ρ_2 *and* ρ_3 *interchanged. Insets: electron density profiles along z.*

In conclusion from a reflectivity experiment one is able to reconstruct the structure of a multilayer in terms of d_j and n_j.

Disregarding for a moment the internal structure of the film, only the (large) discontinuities at the two interfaces with vacuum are left in fig.2.3. From eq.2.16 and eq.2.17 the reflectivity curve now results from the interference of the two waves reflected at $z = 0$ and at $z = L$, with $L = \sum_{j=2}^{N} d_j$. $R(q_z)$ will then show a series of maxima and minima corresponding to constructive and destructive interference of the waves reflected at the top and at the bottom of the film (Kiessig fringes). The separation of two successive maxima is $\Delta q_z = 2\pi/L$. Fig.2.4a shows a calculation of the intensity reflected from a uniform membrane in which the Kiessig fringes are clearly visible. In smectic membranes there is an additional layer structure. Hence Bragg-like peaks are found at a $q_z = 2m\pi/d$, with $m = 0, 1, 2, \ldots$ (see fig.2.4b and c). The phase of the electron density modulation determines in the reflectivity curve the position of the minimum

relative to the first Bragg peak. When the electron density of the outermost layer is higher than that of the next one, the reflected intensity shows a minimum before the first Bragg peak. This minimum is positioned after the first Bragg peak in the opposite case. This is illustrated in fig. 2.4b and c and the corresponding electron density profiles in the insets.

2.3 Reflectivity in the first Born approximation

Though the dynamical formalism has the advantage of being exact, in many practical cases it is acceptable to make approximations in calculating the reflected intensity. The *kinematical* theory or *first Born approximation* greatly simplifies the expressions of sec. 2.2. In this paragraph such a simplified expression for the reflected intensity will be derived step-by-step from eq. 2.16. The basic assumption is that the amplitude of the transmitted wave is taken equal to that of the incident wave [11, 37, 38]. Consequently, also multiple scattering is disregarded. These assumptions are applicable in the case of weak scatterers, as it is the case for liquid crystal membranes, for $q_z \gg q_c$; for $q_z \lesssim q_c$ the above-mentioned assumptions are never valid. In eq. 2.16 multiple reflections are taken into account by the cross term, $(r_{j,j+1}r_{j+1,j+2})$. Neglecting this term allows to rewrite eq. 2.17 as (remembering that $z_1 = 0$):

$$R(q_z) = \left| \sum_{j=1}^{N} r_{j,j+1} exp(iq_{z,j}z_j) \right|^2 . \tag{2.18}$$

The second step is to neglect refraction effects at each interface. This corresponds to changing the phase factor of eq. 2.18 to the simpler expression $exp(iq_z z_j)$. This assumption can be justified by the fact that $n_j \approx 1$, which is equivalent to $\lambda_t \approx \lambda_i$. Again this substitution has rather dramatic consequences in the proximity of the critical angle [37]. If refraction can be neglected, the momentum transfer inside the material does not vary significantly from one layer to the next. Hence for $q_z \gg q_{c,j}$ the Fresnel coefficient in eq. 2.18 can be expanded:

$$r_{j,j+1} = \frac{q_{z,j}^2 - q_{z,j+1}^2}{(q_{z,j} + q_{z,j+1})^2} \approx \frac{q_{c,j+1}^2 - q_{c,j}^2}{4q_z^2} = \frac{4\pi r_e(\rho_{j+1} - \rho_j)}{q_z^2} \tag{2.19}$$

By substituting 2.19 in 2.18 one finally obtains:

$$R(q_z) = \sum_{j=1}^{N} \left| r_{j,j+1} exp(iq_z z_j) \right|^2 = \frac{16\pi^2 r_e^2}{q_z^4} \sum_{j=1}^{N} \left| (\rho_{j+1} - \rho_j) exp(iq_z z_j) \right|^2 \tag{2.20}$$

Any system can be sliced in an infinite number of layers. Hence the summation in eq. 2.20 can be written as an integral over z of the electron density gradient. In doing so, we also rewrite the factor before the summation using eq. 2.14:

$$R(q_z) = R_F \left| \int_{-\infty}^{+\infty} \frac{d\rho(z)}{dz} exp(iq_z z) dz \right|^2 . \tag{2.21}$$

The validity of the Born approximation is limited to $q_z \gtrsim 3q_c$. In this thesis, it will be used in ch. 4 for the calculation of the intensity of the transverse diffuse scans (see ch. 3) at the first Bragg position, for which this condition is well fulfilled. The range of validity of eq. 2.21 can be extended by taking refraction at the first interface (vacuum/membrane) into account by replacing in eq. 2.21 q_z with $q'_z = \sqrt{q_z^2 - q_c^2}$ [43].

Eq. 2.21 is only a particular case of the first Born approximation. An expression valid not only for the intensity reflected along q_z but describing the intensity S($\mathbf{q}$) scattered over the full solid angle can be written analogously to eq. 2.21 [11]:

$$S(\mathbf{q}) = \int d^3 r d^3 r' \exp(i\mathbf{q} \cdot (\mathbf{r} - \mathbf{r}')) \langle \rho(\mathbf{r}')\rho(\mathbf{r}) \rangle . \tag{2.22}$$

where the electron density gradient along z has been substituted by the 3D density-density correlation function $\langle \rho(\mathbf{r}')\rho(\mathbf{r}) \rangle$. The integral is carried out over the illuminated volume. Eq. 2.22 makes clear that $S(\mathbf{q})$ is the Fourier transform of the density-density correlation function.

2.4   Reflectivity from rough interfaces

Real interfaces are never perfectly sharp as assumed so far. The roughness of an interface can have various origins. For example, on solid surfaces imperfections are always present while thermal fluctuations occur at a liquid-air interface. Roughness produces a lateral variation of the electron density and therefore causes scattering of part of the incoming radiation away from the specular direction, fig. 2.5. This intensity, measured at non-zero values of $q_\perp$ (where $\perp = x, y$), is the so-called *diffuse* or *off-specular* reflectivity. It carries information about the lateral structure or roughness of the interface.

An interface can be described by a function which defines at each point the distance to a reference plane, as indicated in fig. 2.5. Such function is called the height distribution function of the interface, written as $h(\mathbf{r}_\perp)$, where the positional vector $\mathbf{r}$ has components $(\mathbf{r}_\perp, z)$ and z is
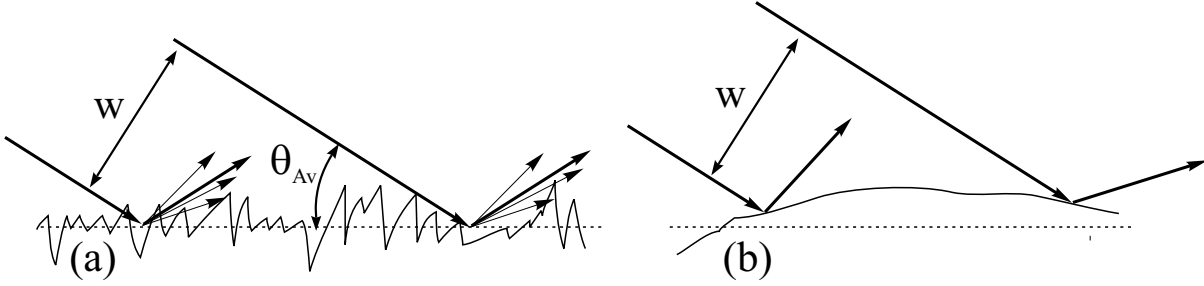
Figure 2.5: *Schematic representation of different types of roughness in relation to the beam size* w. *(a) microscopic roughness: over the illuminated area an average interface can be defined; (b) macroscopic curvature of the interface: the incoming angle varies continuously over the illuminated area, and an average interface can only be defined over a much larger footprint.*

perpendicular to the interface. In a x-ray reflectivity experiment it is not possible to determine $h(\mathbf{r}_\perp)$ directly; only the corresponding height-height correlation function is accessible [37, 38]:

$$g(\mathbf{r}_\perp - \mathbf{r}'_\perp) = \langle [h(\mathbf{r}_\perp) - h(\mathbf{r}'_\perp)]^2 \rangle \quad , \tag{2.23}$$

where $\langle \ldots \rangle$ denotes statistical average. If the height distribution is normal, then it is described by a Gaussian random variable and the r.m.s. roughness σ is equal to:

$$\sqrt{g(\infty)} = \sqrt{2}\sigma \quad , \tag{2.24}$$

where 2σ is the full-width at $1/e$ of the maximum of the Gaussian height distribution.

Smectic membranes are fluid-like in the plane of the smectic layers, i.e. there is no static roughness. Hence the layers fluctuate around their equilibrium position and the "dynamic roughness" is given by the average amplitude of such fluctuations; in the following the latter term will be used. As a consequence of the fluctuations the average value of $\rho(z)$ becomes continuous across the interface. Consequently a specular reflectivity scan contains information on the r.m.s. amplitude of the fluctuations. It will be clear that such a fluctuation-averaged interface cannot be distinguished from a (static) graded interface of the same shape. In practice an error function has been a useful choice to approximate the shape of $\rho(z)$. Conveniently, its first derivative is a Gaussian function, so that the r.m.s. amplitude of the height distribution is given by eq.2.24. The expression for the specular intensity can then be found simply by multiplying
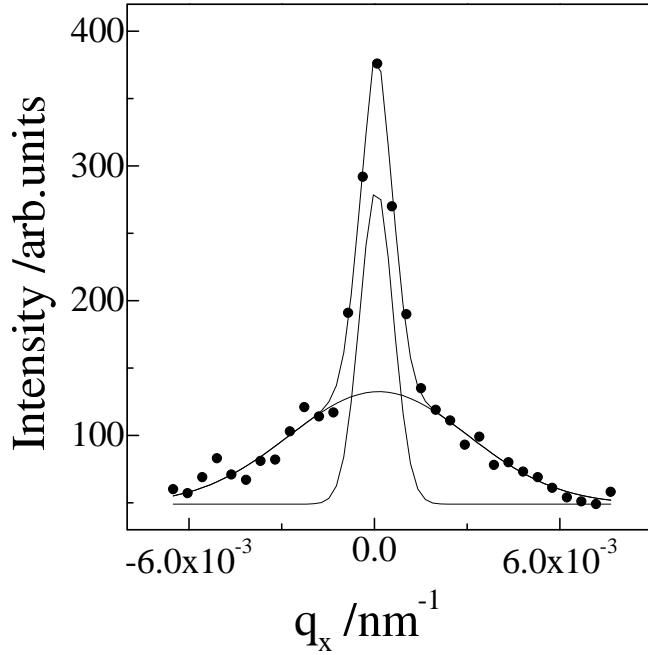
Figure 2.6: *Rocking scan of a 38-layer smectic membrane at $q_z = 6.2$ nm^{-1} (i.e. $2.8q_0$). The total intensity is fitted by a superposition of two Gaussian functions. The central narrow Gaussian function can be identified with the specular reflectivity; the underlying broader one with the diffuse scattering.*

eq. 2.21 with a Debye-Waller factor:

$$R(q_z) = R_F \left| \int_{-\infty}^{+\infty} \frac{d\rho(z)}{dz} exp(iq_z z) exp(-q_z^2 \sigma^2) dz \right|^2 \tag{2.25}$$

The averaging procedure just described applies to the situation of fig. 2.5a where a reference plane can be defined. In contrast, fig. 2.5b shows a modulation of the surface with a wavelength comparable to the illuminated area. Then a statistical averaging over the height distribution of the interface cannot be done in order to take into account the decrease of the specular intensity. In this situation the shape of the interface must be precisely known in order to correct the reflected intensity.

2.4.1 Intensity reflected outside the scattering plane

A specular reflectivity scan alone does not allow to discriminate between the two situations shown in fig. 2.5: a q_x scan or *rocking* scan is needed. In a rocking scan the detector is fixed at an angle 2θ and the sample is rotated with respect to the incoming beam: $\alpha + \beta = 2\theta$ (see sec. 3.3). For small angles, the variation of q_z is practically negligible, so that a rocking scan is equivalent to a q_x scan. An example is shown in fig. 2.6. These data can be fitted by the superposition of two Gaussian functions. The central narrow Gaussian function is the so-called

specular scattering. The wider less intense peak in fig.2.6 can also be fitted to a Gaussian function. This is the *diffuse* scattering. If the distribution of the fluctuations of the interface is normal, this is also of Gaussian shape [37, 38, 43].

The Gaussian line shape is given by the convolution of the scattered intensity with the experimental resolution function $\mathcal{R}$, which depends on the geometry of the experiment and on the wavelength dispersion, as it will be shown in sec.3.4. Knowing $\mathcal{R}$ one can discriminate between the situations of fig.2.5a and fig.2.5b. For a perfect interface, a perfectly parallel incoming beam and infinitely narrow slits, the narrow Gaussian in fig.2.6 would degenerate into a δ-function. For a perfect interface, finite slit sizes and an incoming beam with a Gaussian intensity distribution around the incoming angle (i.e. with a Gaussian resolution function) a Gaussian peak would be found. The same peak shape also results from a rocking scan made with a Gaussian beam on an interface of the type of fig.2.5a. However, if distortions of the interface on a scale comparable with the width of the resolution function are present in the illuminated area (fig.2.5b), the shape of a rocking curve cannot be described by the resolution function anymore. In our case, such a situation can be generated by residual curvature of the membrane (cf. sec.3.1.2). Such a contribution is referred to as *mosaicity*. During a specular or a rocking scan the footprint - and thus the mosaicity - changes. In order to measure the mosaicity of the sample, high resolution rocking scans have to be made at different positions along the specular ridge. For the experiments presented in this thesis, the mosaicity was always at least a factor of 5 smaller than the resolution used in the actual experiments. Hence the influence of its possible variation with the footprint can be disregarded.

In the following an expression for the intensity measured in a q_x-scan will be derived starting from eq.2.22. As the smectic membranes considered here are axially symmetric around z, the same expression holds for q_y-scans. Though the discussion will be focussed on (fluctuating) smectic membranes, the same type of reasoning can be applied to any multilayer system [37,38]. Let us first consider a single fluctuating liquid interface. Such an interface can be described by the displacement function $u(\mathbf{r}_\perp)$, which defines the displacement of each point of the interface with respect to a reference plane. Here we consider only displacements averaged over a certain time t; in sec.6.2 a treatment of the time dependence of the fluctuations is presented. Analogously to eq.2.23 the displacement-displacement correlation function of a single liquid interface can be written as:

$$g(\mathbf{r}_\perp - \mathbf{r}'_\perp) = \langle [u(\mathbf{r}_\perp) - u(\mathbf{r}'_\perp)]^2 \rangle \qquad . \qquad (2.26)$$

Generalizing this expression to a multilayer system and choosing a reference $r_\perp = 0$, the displacement-displacement correlation function between two smectic layers reads:

$$g_{m,n}(\mathbf{r}_\perp) = \langle u_m(0)u_m(0)\rangle + \langle u_n(\mathbf{r}_\perp)u_n(\mathbf{r}_\perp)\rangle - 2\langle u_m(0)u_n(\mathbf{r}_\perp)\rangle = 2\sigma^2 - 2G_{m,n}(\mathbf{r}_\perp) \quad . \text{ (2.27)}$$

Here m and n indicate two arbitrary layers from the smectic membrane. Central to the considerations is the determination of the function $G_{m,n} = \langle u_m(0)u_n(\mathbf{r}_\perp)\rangle$ to be discussed in some details in sec. 4.2.

The electron density of a smectic multilayer can be expressed in terms of the layer displacement:

$$\rho(\mathbf{r},t) = \sum_n \rho_s(z - nd - u_n(\mathbf{r}_\perp)) = \int dz' \sum_n \rho_s(z')\delta(z - z' - nd - u_n(\mathbf{r}_\perp)) \quad . \qquad \text{(2.28)}$$

In this equation the sum is carried over the layers indexed by n, ρ_s is the electron density of a single layer and d is the smectic layer spacing. If the random displacements u_n of the layers are Gaussian, eq. 2.22 becomes:

$$S(\mathbf{q}) = |\rho_s(q_z)|^2 \int d^2\mathbf{r}_\perp \sum_{m,n} \exp\left[iq_z(m-n)d + i\mathbf{r}_\perp \cdot \mathbf{q}_\perp - \frac{1}{2}q_z^2 g_{mn}(\mathbf{r}_\perp)\right], \qquad \text{(2.29)}$$

From eq. 2.29 information on the spectral dependence of the displacement-displacement correlation function can be extracted by a scan along $\mathbf{q}_\perp$.

2.5 Coherence of x-rays

2.5.1 Coherence lengths

Throughout this chapter perfect plane waves were implicitly assumed, which is obviously an idealization. In this section we discuss these limitations by recalling the concept of the *coherence length* of a beam. A real x-ray beam deviates from the ideal case in two ways: it is not perfectly monochromatic and does not propagate in a perfectly well defined direction. For a beam of electromagnetic waves incident on a surface the coherence length can be defined as the distance over which the phase is conserved [11, 44]. Thus the *longitudinal* coherence length (ξ_l) is defined as the maximum distance at which two points along the direction of propagation of the beam are in phase. This length (expressed in wavelength units) must be inversely

proportional to the degree of monochromaticity ($\Delta\lambda/\lambda$) of the beam. Hence:

$$\xi_l \approx \frac{\lambda^2}{\Delta\lambda}. \tag{2.30}$$

The degree of monochromaticity of a typical x-ray monochromator is of the order of 10^{-4}, which leads for the CuK$_\alpha$ radiation ($\lambda = 0.154$ nm) to a value $\xi_l \approx 1.5\ \mu$m.

The *transverse* coherence length (ξ_t) is defined in the plane perpendicular to the direction of propagation. It is inversely proportional to the source size s scaled with the wavelength, and directly proportional to the distance R from the source [11, 44]:

$$\xi_t \approx \frac{\lambda R}{2s}. \tag{2.31}$$

A synchrotron source is asymmetric because of the relativistic narrowing of the emitted cone in the vertical (V) direction [44]. At the ESRF the dimensions of the source at ID10 are 760 μm in the horizontal plane and 53 μm in the vertical plane [45]. From these values and with $\lambda = 0.154$ nm and $R \approx 46$ m, we calculate a transverse coherence length of about 5 μm and approximately 70 μm in the horizontal and vertical plane, respectively. At BW2 at the Hasylab the horizontal source size is 5.2 mm in the horizontal plane, and 1.2 mm in the vertical plane. With $R \approx 30$ m, this leads to $\xi_l = 1.5\ \mu$m, while it is $\xi_t = 0.5\ \mu$m in the horizontal and $\xi_t = 2.0\ \mu$m in the vertical direction, respectively. The projected coherence length at the first Bragg position ($\alpha \approx 1.5°$) becomes approximately 20 and 75 μm for vertical and horizontal membranes, respectively.

2.5.2 Partial coherence and reflectivity experiments

An x-ray beam impinging on a smectic membrane defines an illuminated volume and a coherence volume. The transverse coherence area is given by the product of the two transverse coherence lengths projected on the sample surface. Along the beam, coherent illumination means that the maximum path length difference Δ for x-rays in the sample has to be smaller or equal to ξ_l. It will be clear that in general the resulting coherence volume is anisotropic. The ratio between the dimensions of the coherence volume and those of the illuminated volume determines what is measured in a scan along a particular direction. When the coherence volume is smaller than the illuminated volume, the total intensity measured by the detector is the sum of the intensities scattered in each "coherence domain" of the sample: the phase information is

lost. In the reverse case, the signal results from the sum of the single amplitudes of the scattered photons: the phase information is conserved.

In the z direction perpendicular to a smectic membrane, the maximum path length difference Δ is reached for waves reflected at the top and bottom interfaces. This interference generates a modulation of the scattered intensity known as "Kiessig fringes". The quantity Δ depends on the thickness of the membrane and on the incoming angle via $\Delta = 2L\sin\alpha$. For a 1000-layer membrane $L \approx 3$ μm. In practice, $\alpha \lesssim 10°$ which gives a maximum value of $\Delta \approx 1$ μm. As calculated above, $\xi_l \approx 1.5$ μm and Kiessig fringes can be observed for all the q_z scans presented in this thesis. It is intuitively clear that additional requirements are imposed on the detector slits during a q_z-scan. If the slits are too wide, an averaging of the reflected intensity occurs at the detector and again no fringes can be measured. The maximum distance Δ_M over which the interference is still measurable after this averaging depends on the detector settings and on the scattering geometry. Along the z direction it can be expressed as $\Delta_M \approx \lambda/2\Delta\beta$, where $\Delta\beta$ is the detector angular acceptance [37]. In sec. 3.4.3 the detector angular acceptance for the scattering geometries used in this thesis will be discussed. Typically $\Delta\beta \approx 0.01°$, which corresponds to $\Delta_M \approx 1$ μm, which is of the same order of magnitude as Δ. In conclusion, for films not only ξ_l but also the detector settings limit the maximum thickness measurable experimentally via the interference fringes.

Along the surface of a smectic membrane ($\perp$ direction) the illuminated area is in general much larger than the coherence area. The transverse coherence length projected on the sample surface defines the width of "coherence domains". Only waves reflected within a coherence domain interfere. The total intensity measured at the detector results from the sum of the intensities of all the domains. Thus during a $q_\perp$-scan the intensity is averaged at the sample and no interference effect can be measured independently of the detector settings. Nevertheless, an additional averaging is also done at the detector, depending on the scattering geometry and on the slits settings, similarly to q_z-scans.

2.5.3 X-ray Photon Correlation Spectroscopy

In order to observe interference effects when an x-ray beam impinges on a surface, it is necessary to reduce the dimensions of the beam such that the illuminated volume is of the same order of magnitude as the coherence volume. The coherently reflected waves then interfere creating a pattern of so-called *speckles*, characterized by an in-plane momentum transfer and

an intensity. This pattern is a function of the lateral distance between the individual scatterers in the illuminated volume. If the surface is a fluctuating (liquid) interface the intensity of the speckles will fluctuate according to the instantaneous relative distances between the scatterers in the coherence volume. The movement of the scatterers with respect to each other can be studied by analyzing the intensity variations of a single speckle in time. At delay times (τ) short compared to the typical time scale (τ_0) of the system, the intensity is correlated with the initial intensity. Conversely, for very large τ the position of the scatterers will be independent from the initial one. At intermediate times a transition is observed corresponding to τ_0.

The above description of a photon correlation spectroscopy experiment can be formalized by introducing the intensity-intensity time autocorrelation function. It can be written as a function of the delay time τ between two successive observations: $\langle I(\mathbf{q},t)I(\mathbf{q},t+\tau) \rangle$, in which $I(\mathbf{q}, t)$ is the intensity at a given time t and at a given position in the reciprocal space $\mathbf{q}$. Usually the normalized correlation function is used and the time axis is set such that the origin coincides with the beginning of the experiment, so that one obtains:

$$G^{(2)}(\mathbf{q},\tau) \;=\; \frac{\langle I(\mathbf{q},0)I(\mathbf{q},\tau) \rangle}{\langle I(\mathbf{q},0)\rangle^2}. \tag{2.32}$$

In practice, x-ray photon correlation spectroscopy (XPCS) experiments are performed with a pinhole of dimensions comparable to ξ_t (i.e. $\sim 10\,\mu$m in diameter) selecting a cone of radiation emitted from a source. In this way the dimensions of the illuminated area are of the same order of magnitude as the coherence area. In fact the pinhole can be considered as a new coherent source of radiation, which creates the well-known Fraunhofer diffraction pattern on a far-field screen [11]. The zeroth order maximum of the modulation is selected by putting a collimating pinhole about 25 cm after the first one. It is evident that this procedure cuts down a great deal of the emitted intensity and such experiments are only possible at a third generation synchrotron source. Beamline ID10 at the ESRF is able to deliver $\sim 10^{15}$ photons·cm^{-2}·s^{-1} at the sample, while in a coherent experiment typical fluxes are $\sim 10^9$ photons ·cm^{-2}·s^{-1}.

The coherent photon flux emitted by a source scales with the source brilliance ($\mathcal{B}$) and the wavelength squared :

$$I_{coh} \propto \lambda^2 \mathcal{B}. \tag{2.33}$$

From this equation it is evident that soft x-rays can be used advantageously over hard ones. Unfortunately, their application is limited by the increased absorption, which creates several other problems. Ref. [6] shows first results for the dynamics of smectic membranes obtained with

soft x-rays (i.e. $\lambda \approx 4.4$ nm). In ch. 6 we shall demonstrate the possibility to use conventional 8-10 keV x-rays for this purpose. The latter energies correspond to wavelengths around 0.1 nm. XPCS in this energy region has been used in several studies of the dynamics of hard and soft matter [46–48] with some emphasis on the relatively slow dynamics (ms range) of colloidal systems.

Chapter 3

Experimental

In this chapter the ingredients needed to perform the experiments and the analysis of the experimental data will be discussed. In the first section the sample preparation and handling are considered. The second section concerns the experimental setups used for the reflectivity experiments to be discussed in ch. 4 and ch. 5 and for the XPCS measurements to be presented in ch. 6. The third and fourth sections concern the geometry of the reflectivity scans and the modelling of the reflected intensity including the resolution function, respectively.

3.1 Sample environment

3.1.1 The compound 4O.8

All the experiments presented in this thesis have been performed on smectic membranes of N-(4-*n*-butoxy-benzilidene)-4-*n*-octylaniline, (4O.8). Its molecular structure and phase diagram are shown in fig. 3.1. This molecule belongs to the class of the *Schiff bases*. The last step of its synthesis is the dehydration reaction shown on the top of fig. 3.1. In the presence of water the equilibrium moves towards the left. Hence, to prevent degradation, the sample was stored at room temperature and 10^{-3} atm in the presence of Silica-gel. Batches of the compound could be conserved in such a way for years without observing any changes in the transition temperatures reported in fig. 3.1. Two batches of 4O.8 were used for all the experiments: the first one was obtained from Aldrich and additionally purified via several recrystallization steps by Dr. R. Eidenschink (Nematel, Mainz); the second one was obtained by Frinton Laboratories Inc. and used as received. The transition temperatures of both batches are reported in fig. 3.1.
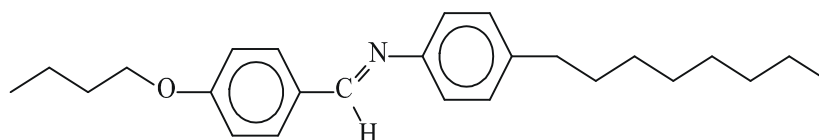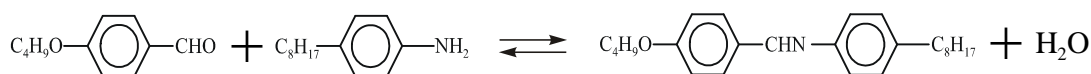
$$\text{K 33 CrB 48.5 SmA 63.5 N 78 I}$$

Figure 3.1: *(Top) The equilibrium reaction in the last step of the synthesis of 4O.8 . The equilibrium can be moved towards the right by decreasing the concentration of water. (Bottom) Molecular structure and bulk transition temperatures of 4O.8.*

3.1.2 Sample holders

The smectic membranes[1] were spanned over a rectangular hole with sharp edges in a polished plate (cf. fig.3.2a). Holders were made of brass or of stainless or hardened steel (Impax). The edges were spark cut and subsequently the holders were polished with 1μm Diaplast. No broadening of the rocking scans due to changes in the mosaic was observed in dependence of the material of the frame. All holders were cleaned in acetone in an ultrasonic bath shortly before spreading a membrane. The smectic membranes were spanned manually. The $15°$ angle with the upper surface ensures that the film hangs in the vicinity of the upper face of the sample holder. This requirement is important because for grazing incidence of the x-ray beam and membranes hanging below the surface of the holder, part of the sample is not accessible (fig. 3.2b). The shadowed region is given by: $s = h/\tan\alpha$. In practice only membranes hanging at a distance $0 \leq h \lesssim 50$ μm were accepted for experiments, which corresponds to a maximum value $s \approx 6$ mm at a minimum incident angle $\alpha = 0.5°$. Shadowing is equally important at the detector side, and thus the usable area of a film hanging at a distance h from the upper surface is diminished by $2s$.

In practice shadowing could be neglected by choosing the dimensions of the sample holder conveniently (a and b in fig.3.2a). The lowest value of α determines the maximum value of the illuminated area (footprint), which is given by $f = w/\sin\alpha$, where w is the beam width. Typical

---

[1]In this and the next section we will closely follow ref. [27] because of the similarity of the instrumentation.
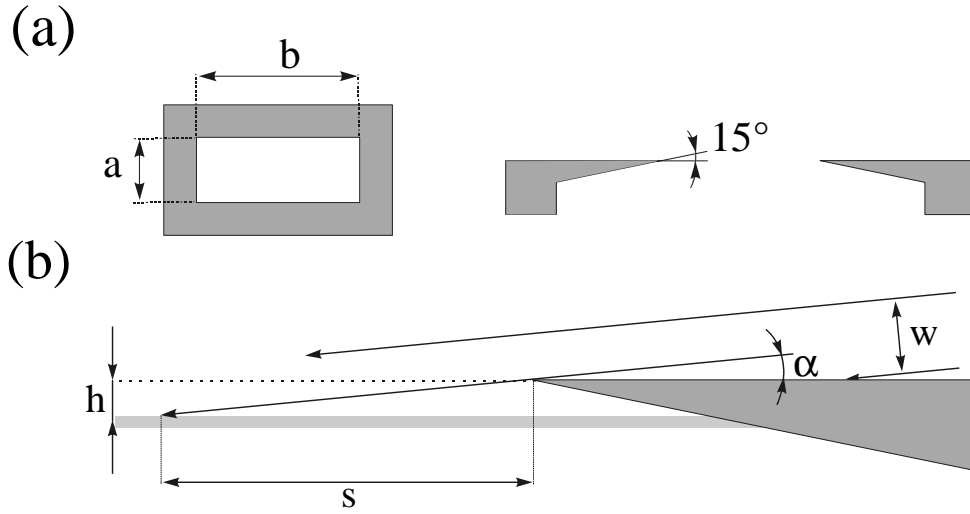
Figure 3.2: (a) *Top and side view of rectangular sample holders. Different sizes have been chosen for different experiments (see text).* (b) *Magnification of a film hanging at a distance* h *below the surface of the holder: the part of the film not accessible to the beam (s) is a function of both* h *and the incoming angle* α*;* w *is the incident beam width.*

specular reflectivity scans were performed with $0.5° \lesssim \alpha \lesssim 6°$ and a beam width $w = 100 \, \mu$m, which corresponds to a spread in f between 11 and 1 mm during the experiments. Values of $a = 10$ mm, $b = 23$ mm were chosen. Hence, for a film hanging 50 μm below the upper surface $(b - 2s) \approx 11$ mm. In many cases the shadowing was below this value so that it was possible to extend the range accessible experimentally down to $\alpha \approx 0.4°$. In the vertical direction, the illuminated area is given by the beam size of typically 5 mm and stays constant during the experiments. Hence the value of $a = 10$ mm allows shifting the sample vertically if desired.

Some trials were also done with circular (diameter= 55 mm) and with *kingsize* rectangular holders (dimensions $a = 40$ mm and $b = 70$ mm; see fig. 3.2). Membranes between three and 20 smectic layers did not show any different behaviour with respect to the corresponding ones in the smaller frames. Nevertheless we did not succeed in making thicker films on these holders.

The sample holders presented so far do not allow to control the thickness of the membrane once it is formed. For this reason a conceptually different sample holder with moving blades has been developed, fig. 3.3. In such a frame the membranes are obtained by separating slowly the movable parts, which were previously wet with the LC material. The frame is built from a block of hardened steel of suitable dimensions polished on the long side from which also the
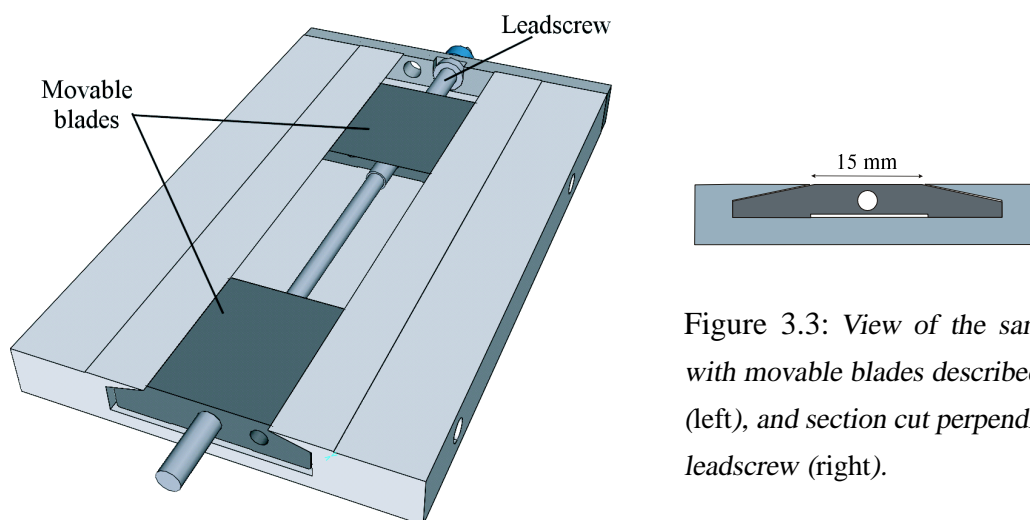
Figure 3.3: *View of the sample holder with movable blades described in the text* (left), *and section cut perpendicular to the leadscrew* (right).

two smaller blades are spark-cut. Finally, the sharp edges are polished and the two smaller blades are mounted on a leading screw, which runs parallel to the long direction of the original block. By moving the lead screw the distance between the small blades can be varied. An important aspect is that the small blades are moving in the single-piece construction containing the rigid larger blades. This ensures a good planarity of the system and thus a good mosaicity of the samples.

The membranes obtained with the various types of sample holders described in this section always give resolution limited rocking curves (cf.sec.2.4.1 and sec.3.3) over a footprint up to ~ 8 mm and at an incoming divergence of the beam typically of the order of $\approx 0.045°$. Usually such scans were performed at few positions along q_z ; typically: $0.5\ q_0$, q_0 and $1.5\ q_0$.

3.1.3 Ovens and temperature controls

During an x-ray experiment the sample holder plus the smectic membrane is inserted in a copper two-stage oven consisting of a cylindrical inner and outer part. A side-view of the ovens is shown in fig.3.4. The sample holder is confined to its position in a rectangular frame in the inner oven by two screws. Both ovens have Kapton windows allowing the reflected x-ray beam to pass at angles between $0°$ and $70°$ in the plane parallel to the sample surface, while angles between $0°$ and $12°$ are accessible in the perpendicular plane. The ovens can be mounted on a base plate in two ways: with the axis of rotation either parallel or perpendicular to the plane of
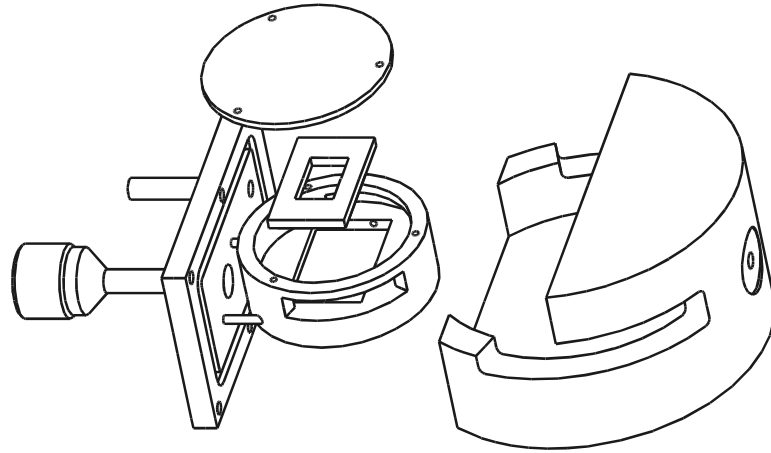
Figure 3.4:   *View of the sample inner (left) and outer oven (right) used in the experiments. The holder is also shown.*

the film, thus allowing experiments with an horizontal and vertical scattering plane, respectively.

The temperature of each oven was measured by a platinum resistor positioned close to the oven center. Heating resistors were attached to the respective outer walls. The temperatures were regulated to $0.1°C$ using Eurotherm PID controllers. During the measurements the temperature of the outer oven was set 2-3°C below that of the inner one. Finally, the ovens were evacuated to $\sim 5 \times 10^{-3}$ atm in order to reduce air scattering and possible sample degradation.

3.1.4   The art of making smectic membranes

To obtain a smectic membrane a spreader is moved over a hole in a holder, which has been previously wet with the LC compound in the SmA phase, as shown in fig. 3.5. The spreading is done by hand, with the holder mounted in the inner oven. During the spreading the environmental temperature is controlled by inserting the whole set-up in a large preparation oven. The LC material can be highly viscous in the SmA phase, which hinders a constant slow spreading process. This is needed to prevent breaking of the membrane before the spreading is completed. In order to reduce the viscosity of the material the temperature is usually set $2 - 3°C$ below the clearing point. In this way usually relatively thin membranes are obtained ($N \lesssim 20$ layers). Thicker membranes require lower temperatures. Membranes with a desired number of layers can be selected also by adjusting the amount of compound collected as well as the spreading speed: putting more material on the spreader and moving it slowly over the frame selects thicker
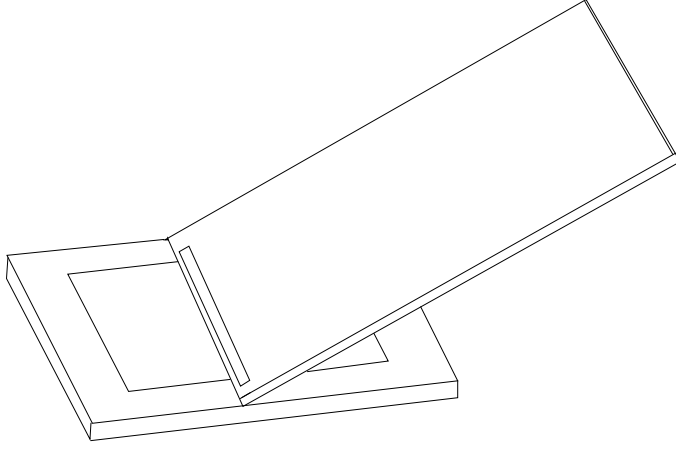
Figure 3.5: *Preparation of a smectic membrane by moving a spreader over a sample holder.*

membranes.

The thickness of the membrane can be checked in situ with an optical reflectometer. It consists of an optical fiber mounted perpendicular to the film surface, which transmits a white beam produced by a tungsten lamp. The light reflected by the film (I_{out}) is collected by six optical fibers arranged around the first one. The intensity is spectrally analyzed by a diffracting prism and measured as a function of λ by an array of photodiodes. The ratio between the reflected and the incoming intensity (I_{in}) is given by [49]:

$$\frac{I_{out}}{I_{in}} = \frac{f \sin^2(2\pi D/\lambda)}{1 + \sin^2(2\pi D/\lambda)} \qquad \text{with} \qquad f = \frac{\left(n_{\parallel}^2 - 1\right)^2}{4n_{\parallel}^2} \quad . \tag{3.1}$$

Eq. 3.1 contains only two adjustable parameters: f and D. The former parameter is a function of the refractive index perpendicular to the smectic layers ($n_{\parallel}$); for $400 < \lambda < 800$ nm an average value of $n_{\parallel} = 1.55$ has been used. The latter parameter is given by $D = n_{\parallel}dN$, where N is the number of smectic layers and d is the smectic layer spacing. The accuracy of this technique depends on the thickness. For membranes of thickness between 20 and 100 layers the error is ± 1 layer. For thicker membranes the accuracy is about 1%; for thinner membranes, the error is 1-2 layers. In the latter case, part of the visible wavelengths spectrum is not reflected, so that the range available for fitting becomes smaller and the error increases.

If the membrane survives the first 30 minutes the inner oven can be covered with its lid and transferred from the preparation oven to the outer x-ray oven, previously heated and mounted on the x-ray stage. Next both ovens are evacuated and the sample is left for annealing. During this period islands that may be present on the surface of the film disappear. The equilibration time can vary between a few minutes and several hours. Smectic membranes that survive the

evacuation are in general stable for several days up to some weeks. Equilibration is best per-
formed mounting the membrane vertically. In this way the Brownian motion of any island is
biased by the gravitational field and the membrane equilibrates faster.

With the above-mentioned kingsize sample holders we never succeeded in obtaining thick
membranes. This is probably due to the fact that the probability of forming holes is quite high
during the (manual) spreading on large openings. Such holes force the film either to thin or, in
the worst case, to collapse. In order to reduce the probability of hole formation, the membranes
were usually prepared at very high temperatures in the SmA phase. Only using the holder
with movable blades membranes can be obtained at temperatures just above the lower limit
of existence of the SmA phase. In this case the speed of spreading can be slow and the high
viscosity is not a problem anymore. Hence, in this way also thick films with a large area can be
obtained. The membranes are prepared by closing the movable blades until only a gap of ~ 0.5
mm is left. Then the LC compound is deposited on the gap and the film is formed by (slowly)
moving the two small blades apart. Membranes up to 20 μm thick and with an area bigger than
4 cm^2 have been obtained in this way.

3.2   X-ray setups

Various diffractometers and x-ray sources have been used to perform the experiments presented
in the later chapters. The experiments described in ch. 4 were partly done at the in-house
rotating anode set-up, and partly at beamline BW2 of the Hasylab (Hamburg, Germany). The
coherent x-ray experiments presented in ch. 6 were performed at ID10A of the ESRF (Grenoble,
France).

3.2.1   In-house setup

X-rays are obtained from a Rigaku RU-300H generator [27] operated at 18 kW. The generator
is computer controlled via an IEEE-488 interface by a program in *Basic*, which monitors the
status of the generator and can provide a restart in case of power trips. Measurements were
made using a triple axis spectrometer schematically shown in fig. 3.6a. The x-rays leave the
anode housing through a beryllium window, pass through an evacuated flight path and enter
the monochromator housing. The monochromator crystal is placed on a turntable at 400 mm
from the source. It consists of a single bent pyrolytic graphite (002) crystal (20 $\times$ 20 mm^2,
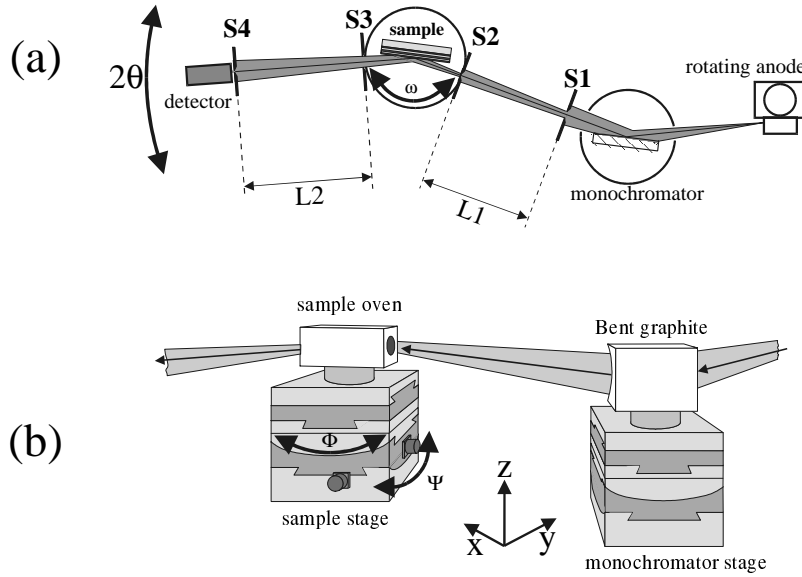
Figure 3.6: *(a) Top-view of the two circle diffractometer and the rotating anode x-ray source; (b) Details of the sample and monochromator stages showing the beam path.*

115 mm vertical radius), which focuses the beam in the *xz*-plane onto the sample. The Cu-K$_{\alpha 1}$ and Cu-K$_{\alpha 2}$ lines are not separated in this moderate resolution setup [50]. The average Cu-K$_\alpha$ wavelength is 0.154 nm, leading to a wave vector $|\mathbf{k}| = 40.75$ nm^{-1}.

Slits S_1 to S_4 are adjustable both in the vertical and in the horizontal direction, but they are motorized only in the scattering plane (the *xy*-plane). The pre-sample slits $S2$ are Huber (H3013) slits, with an accuracy of 10 μm. The incident divergence of the beam in the *xy*-plane (see sec.3.4), $\Delta \alpha_i$, is defined by slits $S1$ and $S2$, set at 0.4 mm and 0.1 mm, respectively, and separated by $L1 = 450$ mm. This leads to $\Delta \alpha \approx 0.045°$ FWHM. A detector scan in the plane of incidence resulted in $\Delta \beta \approx 0.055°$ FWHM determined by $S4 = 0.5$ mm, situated in front of the Cyberstar scintillation detector at a distance detector-sample $L2 = 450$ mm (see sec.3.4). S3 is set to 1.0 mm in order to reduce background scattering from the sample position.

All slits are wide open vertically, while S2 was set at 5 mm. The beam size on the sample is $\backsim 0.12 \times 5$ mm^2 (H$\times$V). In the scattering configuration described, the incident beam intensity is $8 \cdot 10^7$ counts/sec. The background scattering at intermediate angles is near the dark-count levels of the scintillation counter of 0.1 counts/sec as a result of the absence of a substrate as well as the use of an evacuated sample oven. This allows a dynamic range of nearly nine orders of magnitude in the measured intensity.

3.2.2 BW2 at the Hasylab

The principal optical elements of beamline BW2 consist of a plane pre-mirror and a double crystal focusing monochromator consisting of Si(111)-crystals [51]. In our experimental configuration, focusing was achieved only in the vertical direction. The incoming beam energy was set between 9 and 10 keV.

The experimental hutch hosts a multi-purpose diffractometer especially designed for surface x-ray diffraction. The incoming beam size and the detector acceptance can be defined using slits. The beam sizes used are reported in tab.3.2 for the different scattering configurations. When a horizontal scattering plane was used, the components of the resolution function (see sec. 3.4) were set to: $\Delta q_x \approx 4 \cdot 10^{-4} \cdot q_z$, $\Delta q_y \approx 0.02$ nm^{-1} and $\Delta q_z \approx 0.04$ nm^{-1}. This configuration is particularly suitable for so-called δ-scans (see sec.3.3) because Δq_y is reduced due to the focusing of the monochromator. For the 80 and the 107-layer membranes it was necessary to increase the resolution along q_z in order to be able to determine the thickness from the Kiessig fringes. For these samples we used a vertical scattering plane (i.e. horizontal membranes). The resolution components were: $\Delta q_x \approx 2 \cdot 10^{-4} \cdot q_z$, $\Delta q_y \approx 0.05$ nm^{-1} and $\Delta q_z \approx 0.01$ nm^{-1}.

3.2.3 ID10A at the ESRF

The XPCS experiments were performed at the high-brilliance undulator beamline ID10A (TROIKA I) of the ESRF [45]. The beamline was equipped with a Si(111) monochromator in a horizontal scattering geometry (i.e. vertical membranes) set at 7.8 keV. A diffractometer very similar to the in-house triple axis set-up was used. The bandwidth is in this situation $\Delta\lambda/\lambda = 10^{-4}$.

A scheme of the experimental geometry is given in fig.3.7. The longitudinal coherence length was $\xi_l = \lambda^2/\Delta\lambda \approx 1.5$ μm (see sec.2.5). The source size of width $s \approx 730 \times 53$ μm^2 at a distance $R \approx 46$ m from the sample leads a transverse coherence length $\xi_t = \lambda R/(2s) \approx 5$ μm in the horizontal plane and to $\xi_t \approx 70$ μm in the vertical direction. During the experiment, the membranes were mounted vertically (i.e. horizontal scattering plane). A circular pinhole of 12 μm diameter was placed about 0.25 m upstream of the sample to provide a collimated and partially coherent beam. A set of guard slits of 20×20 μm^2 in front of the sample was used to limit the parasitic incoherent scattering from the primary pinhole. An analyzing aperture of 40×40 μm^2 was placed in front of the detector at 1.2 m from the sample. These dimensions
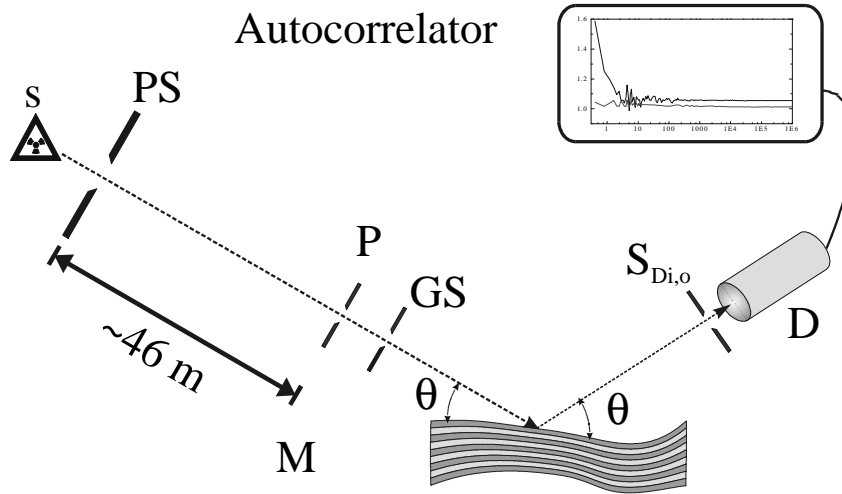
Figure 3.7: *Scheme of the experimental geometry for XPCS at ID10A. The beam emerges from the source (s) with a size determined by the primary slits (PS). A 12 μm pinhole (P) selects the coherent part; subsequently 20×20 μm² guard-slits (GS) limits the (incoherent) parasitic radiation. The coherent radiation specularly reflected by the (fluctuating) sample is collected by the detector (D) and finally sent to the autocorrelator. The 40×40 μm² slits ($S_{D_{i,o}}$) in front of the detector reduce the incoherent scattering (see sec.2.5).*

are chosen such that the aperture is roughly of the size of a single speckle (see sec.2.5). The photon flux was about 2×10^8 photons/s at 100 mA ring current. The synchrotron was operated in the 16-bunch mode during the experiment. The degree of coherence was determined to be of the order of 15%. The resolution of our set up was given by $\Delta q_z = \Delta q_y \approx 10^{-3}$ nm^{-1} and $\Delta q_x \approx 10^{-4} \cdot q_z$ nm^{-1}. The thickness of each membrane was determined from the Kiessig fringes in the specular reflectivity (see sec.2.2). From rocking curves, the mosaicity of the films was found to be typically of the order of $0.005°$ (FWHM) over a typical illuminated area at $\alpha \approx 1.5°$ of 0.5×0.015 mm². Note that due to the 12 μm pinhole the illuminated area is much smaller than used before (cf. sec.3.1.2).

The intensity-intensity time correlation function $G^{(2)}(q,t)$ was recorded at the first Bragg position. The reflected radiation was measured with a fast scintillation counter based on Yttrium-Aluminium-Perovskite (YAP) doped with Ce. The YAP-detector was coupled to a charge-sensitive amplifier followed by a low-level threshold discriminator, which finally resulted in a time resolution of approximately 120 ns. To determine the auto-correlation function the arrival times of all individual pulses from the detector were stored in a buffer memory and subsequently
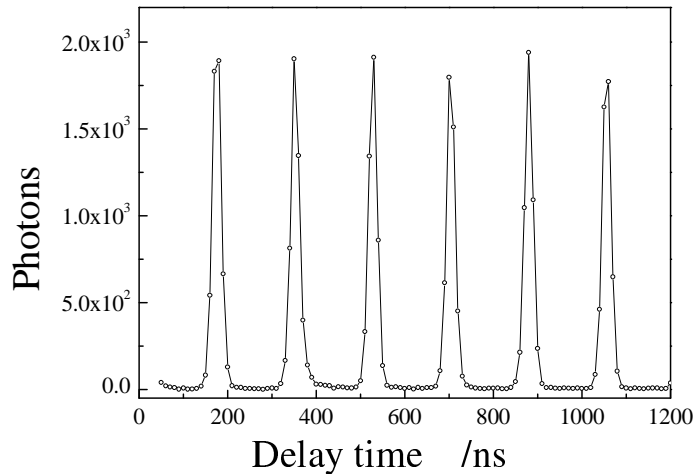
Figure 3.8: *Bunch structure of the synchrotron ring at the ESRF in the 16-bunch mode, as measured by the in-house correlator with a time resolution of 10 ns. In order to construct the correlation function the pulsed structure has been integrated out.*

transferred to a hard disc via a micro-Enable card (Silicon Software GmbH). These times were digitized to the accuracy of the clock frequency (100 MHz). The stored data were used to construct the auto-correlation function using appropriate software.

The time resolution of our measurements was limited by the 16 bunch mode of the synchrotron source, in which electron bunches are equally spaced in the storage ring at 176 ns intervals, fig. 3.8. The bunch structure of the incoming photons could be well resolved and integrated out in order to construct the correlation functions reported in ch. 4. In spite of the high time resolution, data at times faster than about 700 ns are less reliable due to various limitations in the detection electronics. The counting rate $\langle I \rangle$ was typically 5-10 kHz.

The correlation function from the film was normalized via division by a reference correlation function. In this way residual correlations in the beam could be eliminated. As reference a NiC multilayer was used with a periodicity of 3.6 nm, comparable to the smectic layer spacing of 4O.8. The correlation function from the multilayer did not display any dynamic effects and could not be distinguished from the behavior recorded for the direct beam at different stages of the experiment. The statistical error has been calculated from the photon counting statistics, which gives at low count rates:

$$\Delta G^{(2)}(t) = \sqrt{\frac{G^{(2)}(t)}{\langle I \rangle^2 T \, \Delta t}}, \tag{3.2}$$
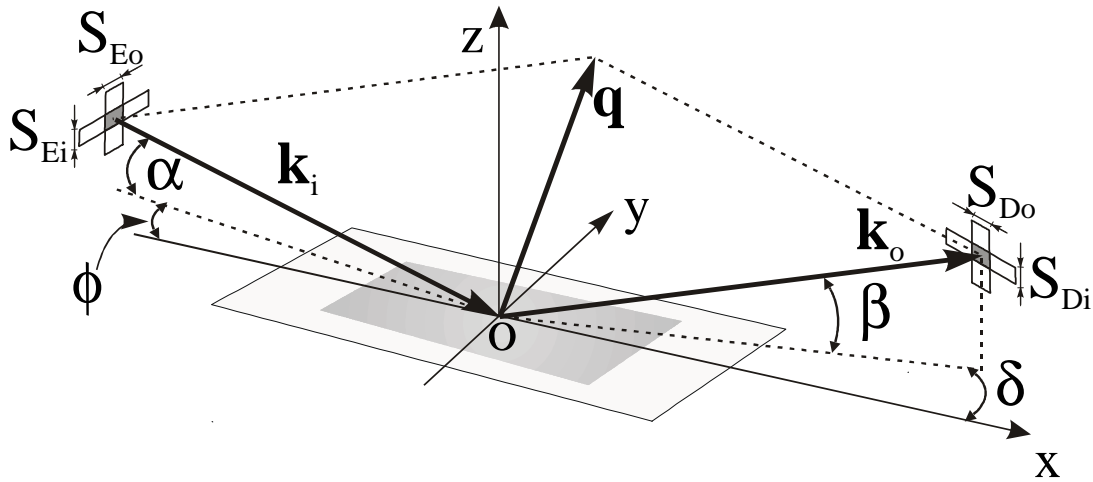
41

Figure 3.9: *General scattering geometry. The incidence plane is defined by the incident wave-vector* $\mathbf{k}_i$ *and the surface normal* (Oz)*; the scattering plane is defined by the scattered wave-vectors* $\mathbf{k}_o$ *and* $\mathbf{k}_i$*; the wave-vector transfer is* $\mathbf{q} = \mathbf{k}_o - \mathbf{k}_i$.

where T is the total counting time and Δt the sampling interval. For our experiments typically $\langle I \rangle \approx 5$ kHz, $T \approx 3600$ s and $\Delta t \approx 180$ ns, which leads to about 1% accuracy. This error is still considerable in relation to the variations in G(t) to be considered (cf. ch. 6). For larger delay times the accuracy could be improved by integrating over larger time intervals.

3.3 Reflectivity scans

The scattering configuration is depicted in fig. 3.9. In order to map the intensity distribution in the reciprocal space three different types of scans can be used. Tab. 3.1 indicates for each type the angle(s) scanned, the angular constrains during the scan and the corresponding q-component(s) in the reciprocal space. First scans with $\delta = 0$ (i.e. in the scattering plane) will be considered. *Specular reflectivity* scans map the reciprocal space along $\mathbf{q}_z$. Fig. 3.10a shows the variation of the scattering vector and the corresponding angles during such a scan. In the reciprocal space only q_z varies, while in the direct space α and β are varied together with $\alpha = \beta = \theta$. In a typical scan the angular range probed is $0.4° \lesssim \alpha \lesssim 5°$, which corresponds to a q_z variation over the interval $0.5 \lesssim q_z \lesssim 7$ nm^{-1}.

In fig. 3.10b the geometry of a q_x-*scan* or *rocking scan* is shown. This is done by fixing the

Reflectivity scan type	Variable angles	Angular constrains	q-components
Specular	α, β	$\alpha = \beta = \theta, \quad \delta = 0$	q_z
rocking scan	$\omega = \alpha - \beta$	$\alpha + \beta = 2\theta, \quad \delta = 0$	$q_x \, (q_z)$
δ-scan	δ	$\alpha = \beta = \theta$	$(q_x) \, q_y$

Table 3.1: *Different types of reflectivity scans with associated angle variations. The corresponding component(s) of* **q** *varying during the scans are given in the last column (minor variations between brackets).*

detector at an angle $2\theta = \alpha + \beta$ while the sample is rocked in the beam. The rocking angle is defined as $\omega = \alpha - \beta$ and the corresponding values of the wave vector transfer are:

$$q_x = 2k\sin\theta \cdot \sin\omega \ , \tag{3.3}$$

$$q_z = 2k\sin\theta \cdot \cos\omega \ . \tag{3.4}$$

The ω-range accessible experimentally is limited by: $-\theta \leq \omega \leq \theta$. Outside this range, the intensity collected by the detector is zero because the sample surface blocks either the incoming or the outgoing beam. Since the specular intensity falls off as θ^{-4} (see sec.2.1), in practice it was never possible to measure a rocking scan for $\theta \gtrsim 3°$. This leads to the maximum momentum transfer accessible experimentally with such type of scans of about 0.23 nm^{-1}. From eq.3.4 it can be seen that in this situation q_z is almost constant: for $\omega = \theta = 3°$, $q_z = 4.459$ nm^{-1} and its variation is $6 \cdot 10^{-3}$ nm^{-1}. During a rocking scan the illuminated area of the sample changes. Therefore, all scans have been corrected for this geometrical effect by dividing the scattered intensity by $\sin\alpha$.

The physical limitations of rocking scans can be avoided by making so-called δ-scans. Such measurements are performed by choosing a (convenient) q_z position on the specular ridge and then varying δ (see fig.3.9). In fact, during these scans both q_x and q_y are varied, while q_z is kept constant:

$$q_x = 2k\cos\theta(\cos\delta - 1) \ , \tag{3.5}$$

$$q_y = k\cos\theta\sin\delta \ . \tag{3.6}$$

Only the background level limits the δ-range accessible experimentally. At the Hasylab, max-
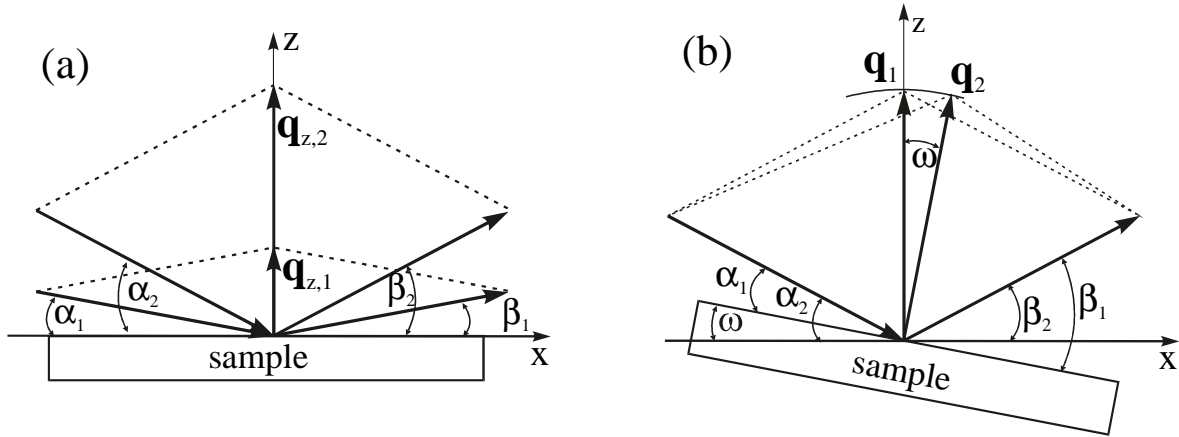
Figure 3.10: *(a): Specular scan along q_z. (b) Transverse diffuse (rocking) scans in which $\omega = \alpha - \beta$ is varied while $\alpha + \beta = 2\theta$ is kept constant. The accessible q_x range for rocking scans is limited by $-\theta \leq \omega \leq \theta$*

imum δ-values of about $10°$ have been reached, which correspond to $q_y \approx 2$ nm^{-1} . In that situation the variation of q_x is only about 2%. As smectic membranes possess axial symmetry around the z-axis, the information from rocking scans and δ-scans (mainly q_x and q_y, respectively) is equivalent. In ch.4 results from both types of scans will be combined resulting in an interval of in-plane wavelengths probed ranging from about 50 μm down to approximately 2 nm.

3.4 Resolution function

X-ray reflectivity and surface diffraction are powerful techniques to probe normal and in-plane structures at the molecular scale [37, 39], and x-ray diffuse scattering has been shown to be very useful in determining the interfacial properties of thin liquid films such as the surface tension and bending elasticity modulus [38, 52]. In all these experiments, the experimental resolution must be carefully taken into account as the physical information is intimately mixed up with it. The origin of the resolution stems from the properties of the particular scattering geometry pictured in fig. 3.9 for a *z*-axis set-up. The vector $\mathbf{k}_i$ defines the direction of the beam incident on the sample; the plane defined by the (Oz) axis and $\mathbf{k}_i$ is called the plane of incidence. The direction of $\mathbf{k}_i$ is experimentally defined by α and ϕ. The incident beam has in general a rectangular

cross section defined by two orthogonal sets of slits S_{E_i} and S_{E_o} perpendicular to $\mathbf{k}_i$ (pre-sample slits). The scattered vector $\mathbf{k}_o$ is defined by the position of the detector at the angles β and δ; the plane defined by $\mathbf{k}_i$ and $\mathbf{k}_o$ is called the scattering plane. The detector entrance is defined by two orthogonal sets of slits S_{D_i} and S_{D_o} perpendicular to $\mathbf{k}_o$. The experimental resolution includes the wavelength dispersion, the beam angular divergence and the detector acceptance angles. In other words, $\mathbf{k}_i$ and $\mathbf{k}_o$ are not ideally defined, but dispersed. The dispersion relative to $\mathbf{k}_i$ depends on the optical set-up before the sample (source, monochromator etc.). The dispersion relative to $\mathbf{k}_o$ comes from purely geometrical considerations. It is due to the existence of acceptance angles as defined by the detector slits and the illuminated area on the sample (footprint).

The measured scattered intensity I results from averaging over the angular deviations and can be expressed as a function the wave-vector transfer $\mathbf{q} = \mathbf{k}_o - \mathbf{k}_i$. It can be written as the convolution of the scattering function S with a resolution function $\mathcal{R}$ describing the distribution of the deviations $\mathbf{q}'$ around $\mathbf{q}$:

$$I(\mathbf{q}) = \int S(\mathbf{q} - \mathbf{q}') \mathcal{R}(\mathbf{q}') d\mathbf{q}'. \tag{3.7}$$

This formalism is appealing because it allows the advantageous use of the reciprocal space representation of the scattering function S. In the first Born approximation, S has been defined in eq. 2.22. Note that eq. 3.7 is valid only in the incoherent limit. The effects of partial coherence have their importance especially when using synchrotron radiation. Though they have been discussed in refs. [53,54], the effect of incorporating them in the resolution formalism still have to be investigated.

So far, calculations of $\mathcal{R}$ have been limited to specific situations like specular reflectivity [55], detector scans in the plane of incidence [56] and Bragg diffraction [39]. In these geometries the incident and the scattering plane coincide and eq. 3.7 boils down to simply averaging the scattering function over a resolution area in the plane of incidence. More complicated scattering geometries associated with surface diffraction [57] or scattering out of the plane of incidence [27], require averaging over a full resolution volume. In such situations, $\mathcal{R}$ has not always been clearly analyzed. Following closely refs. [58,59] we present in this section a general method to calculate $\mathcal{R}$. In sec. 3.4.1, a general form for the resolution function is derived, taking into account the deviations associated with the detector acceptance angles. In sec. 3.4.2, useful expressions relating reciprocal and direct space mean square deviations are derived for the scattering geometries used in this thesis. In sec. 3.4.3, a suitable method is given to determine the

mean square values of the experimental parameters.

3.4.1 General resolution function

Let us start with the description of dispersions relative to $\mathbf{k}_i$ and $\mathbf{k}_o$ by introducing random deviations α', ϕ' and β', δ' around the angles α, ϕ, β and δ, respectively. In what follows we assume that α', ϕ', β', and δ' can be described by a Gaussian distribution and are statistically independent. In this case they are fully described by their mean square deviations:

$$\Delta\alpha^2 = \langle(\alpha')^2\rangle, \qquad \Delta\phi^2 = \langle(\phi')^2\rangle \tag{3.8}$$

$$\Delta\beta^2 = \langle(\beta')^2\rangle, \qquad \Delta\delta^2 = \langle(\delta')^2\rangle \tag{3.9}$$

Furthermore, we assume the random deviations to be small. This allows use of linear relation between the angular deviations and $\mathbf{q}'$. From fig. 3.9 the relation between $\mathbf{q}$ and the four angles is:

$$
\begin{cases}
q_x = k\,(\cos\beta\cos\delta - \cos\alpha\cos\phi), \\
q_y = k\,(\cos\beta\sin\delta + \cos\alpha\sin\phi), \\
q_z = k\,(\sin\alpha + \sin\beta).
\end{cases}
\tag{3.10}
$$

For the sake of simplicity, we assume the beam to be ideally monochromatized, so that we can disregard the wavelength dispersion. After taking the partial derivatives we obtain:

$$
\begin{cases}
q_x' = k\,[\alpha'\sin\alpha\cos\phi + \phi'\cos\alpha\sin\phi - \beta'\sin\beta\cos\delta - \delta'\cos\beta\sin\delta] \\
q_y' = k\,[-\beta'\sin\beta\sin\delta + \delta'\cos\beta\cos\delta - \alpha'\sin\alpha\sin\phi + \phi'\cos\alpha\cos\phi] \\
q_z' = k\,[\alpha'\cos\alpha + \beta'\cos\beta].
\end{cases}
$$

These linear relations together with the mean square deviations of eq. 3.8 and eq. 3.9 allow to write down the mean square deviations of $\mathbf{q}$:

$$\langle q_x'q_x'\rangle = k^2\,(\sin^2\alpha\cos^2\phi\Delta\alpha^2 + \cos^2\alpha\sin^2\phi\Delta\phi^2 + \sin^2\beta\cos^2\delta\Delta\beta^2 + \cos^2\beta\sin^2\delta\Delta\delta^2)$$

$$\langle q_y'q_y'\rangle = k^2\,(\sin^2\alpha\sin^2\phi\Delta\alpha^2 + \cos^2\alpha\cos^2\phi\Delta\phi^2 + \sin^2\beta\sin^2\delta\Delta\beta^2 + \cos^2\beta\cos^2\delta\Delta\delta^2)$$

$$\langle q_z'q_z'\rangle = k^2\,(\cos^2\alpha\Delta\alpha^2 + \cos^2\beta\Delta\beta^2)$$

$$\langle q_x'q_y'\rangle = k^2\,(-\sin^2\alpha\sin\phi\cos\phi\Delta\alpha^2 + \cos^2\alpha\sin\phi\cos\phi\Delta\phi^2$$
$$+ \sin^2\beta\sin\delta\cos\delta\Delta\beta^2 - \cos^2\beta\sin\delta\cos\delta\Delta\delta^2)$$

$$\langle q_x'q_z'\rangle = k^2\,(-\sin\beta\cos\beta\cos\delta\Delta\beta^2 + \sin\alpha\cos\alpha\cos\phi\Delta\alpha^2)$$

$$\langle q_y'q_z'\rangle = k^2\,(-\sin\alpha\sin\phi\cos\alpha\Delta\alpha^2 - \sin\beta\sin\delta\cos\beta\Delta\beta^2). \tag{3.11}$$

These equations define the elements of the covariant matrix. The general resolution function $\mathcal{R}$, defined as the Gaussian joint-distribution function of the random deviations q'_x, q'_y, q'_z, can be expressed as follows [60]:

$$\mathcal{R}(\mathbf{q}') = \sqrt{\frac{\det A^{-1}}{(2\pi)^3}} \exp\left[-\frac{1}{2}\mathbf{q}' \cdot A^{-1} \mathbf{q}'\right], \tag{3.12}$$

where $A = \langle q'_i q'_j \rangle$. The prefactor in eq. 3.12 is simply a normalization factor. From here on, we assign the eigenvalues of A to be Δq_x^2, Δq_y^2 and Δq_z^2, and let (O, x, y, z) refer implicitly to the eigenvector coordinate system of A. Then the analytical convolution of eq. 3.7 in combination with eq. 2.22 leads to the following general expression for the intensity:

$$I \sim \int d^3r \exp\left(i\mathbf{q} \cdot \mathbf{r} - \frac{1}{2}x^2\Delta q_x^2 - \frac{1}{2}y^2\Delta q_y^2 - \frac{1}{2}z^2\Delta q_z^2\right) \langle \rho(0)\rho(\mathbf{r}) \rangle. \tag{3.13}$$

The next step consists of carrying out the integration in eq. 3.13. The relation between the reciprocal and direct space mean square deviations is not straightforward. In the next section we shall give some useful approximations for the scattering geometries used during the collection of the diffuse reflectivity data presented in this thesis.

3.4.2 Application to rocking scans and δ-scans

Let us consider first scattering geometries where $\mathbf{q}$ stays in the plane of incidence ($q_y = 0$, $\phi = \delta = 0$). This is for example the case for so-called rocking scans (see fig. 3.10). It also applies to detector scans in the plane of incidence for which β is varied while α is kept constant [61]. From eq. 3.11, and keeping only leading order terms, A reads:

$$A/k^2 = \begin{pmatrix} \alpha^2\Delta\alpha^2 + \beta^2\Delta\beta^2 & 0 & \alpha\Delta\alpha^2 - \beta\Delta\beta^2 \\ 0 & \Delta\phi^2 + \Delta\delta^2 & 0 \\ \alpha\Delta\alpha^2 - \beta\Delta\beta^2 & 0 & \Delta\alpha^2 + \Delta\beta^2 \end{pmatrix}. \tag{3.14}$$

It is clear from the covariance matrix that the eigenvalues Δq_x^2 and Δq_z^2 are strongly correlated, while Δq_y^2 is independent. In the limit of grazing angles in the plane of incidence (α, $\beta \lesssim 10^0$), we obtain the following leading order expressions for the reciprocal space mean square deviations:

$$\begin{cases} \Delta q_x^2 \approx k^2 \left[\Delta\alpha^2\Delta\beta^2(\alpha+\beta)^2/(\Delta\alpha^2+\Delta\beta^2)\right] \\ \Delta q_y^2 \approx k^2(\Delta\phi^2+\Delta\delta^2) \\ \Delta q_z^2 \approx k^2(\Delta\alpha^2+\Delta\beta^2) \end{cases}. \tag{3.15}$$

Note that for $\alpha = \beta$ and $\Delta\alpha = \Delta\beta$, we obtain the relation $\Delta q_x^2 = \alpha^2 \Delta q_z^2$ previously obtained in ref. [56]. The condition $\Delta\alpha^2 \to 0$ depends on the beam characteristics and can be realized using synchrotron radiation or variable grating parabolic multilayer optics, which produce highly parallel beams. In this limit the second order must be taken into account leading to $\Delta q_x^2 \approx k^2 (\alpha^2 \Delta\alpha^2 + \beta^2 \Delta\beta^2)^2/4$. During a scan, the eigenvector coordinate system rotates in the plane of incidence. In fact, for the case of rocking scans, the eigenvector coordinate system corresponds approximately to the original one because of the geometrical constraint $|\omega| \le \theta$. Consequently, we can further simplify the calculation of the intensity in eq. 3.13. One can open the detector slit S_{D_o} widely without modifying the relevant inplane resolution Δq_x^2. In this way, Δq_y is sufficiently large to induce a fast decay of $\exp(-y^2 \Delta q_y^2/2)$. Therefore, only the region $y \approx 0$ will contribute to the integral, like in the case of a δ-function. This allows to keep in the integrand only $\langle \rho(0)\rho(x, y = 0, z) \rangle$ and reduces the calculation to a double integration over x and z only. In the reciprocal space representation the resolution function is reduced to a function of q_x and q_z only. Information about q_y is lost as a result of the large smearing in the y-direction, but does not influence the information about q_x. One finally arrives at an expression similar to eq. 3.7:

$$I(q_x, q_z) = \int dq_x' dq_z' \mathcal{R}(q_x', q_z') S(q_x' - q_x, q_z - q_z'), \tag{3.16}$$

but with $\mathcal{R}$ and S defined as

$$\mathcal{R}(q_x, q_z) = \frac{1}{2\pi\Delta q_x \Delta q_z} \exp\left[-\frac{q_x^2}{2\Delta q_x^2} - \frac{q_z^2}{2\Delta q_z^2} \right]$$

$$S(q_x, q_z) = \frac{\sqrt{2\pi}}{\Delta q_y} \int dx dz \exp(iq_x x + iq_z z) \langle \rho(0)\rho(x, y = 0, z) \rangle.$$

Now, let us consider the case of δ-scans (see sec. 3.3). In this situation the detector is moved by an angle δ while $\phi = 0$ (fig. 3.9). In order to optimize the diffuse signal often in addition $\alpha = \beta$ is used. In this way, q_y and q_x are probed over a large and small range, respectively, while q_z is kept constant on the specular ridge, as deduced from eq. 3.10. In this geometry, the scattering cross section is limited by the resolution in all directions in space. From eq. 3.11, and keeping only leading order terms, A reads:

$$A/k^2 = \begin{pmatrix} \alpha^2(\Delta\alpha^2 + \Delta\beta^2) + \delta^2\Delta\delta^2 & -\delta\Delta\delta^2 & \alpha(\Delta\alpha^2 - \Delta\beta^2) \\ -\delta\Delta\delta^2 & \Delta\phi^2 + \Delta\delta^2 & -\alpha\delta\Delta\beta^2 \\ \alpha(\Delta\alpha^2 - \Delta\beta^2) & -\alpha\delta\Delta\beta^2 & \Delta\alpha^2 + \Delta\beta^2 \end{pmatrix}. \tag{3.17}$$

In the limit of grazing angles in the plane of incidence (α, $\beta \lesssim 10^0$), the inplane eigenvalues Δq_x^2 and Δq_y^2 are strongly correlated, while Δq_z^2 does not depend on the inplane resolution. For grazing angles, we obtain the following useful approximations for the reciprocal space mean square deviations:

$$\begin{cases} \Delta q_x^2 \approx & k^2 \left[4\alpha^2\Delta\alpha^2\Delta\beta^2/(\Delta\alpha^2+\Delta\beta^2)+\delta^2\Delta\phi^2\Delta\delta^2/(\delta^2\Delta\delta^2+\Delta\phi^2+\Delta\delta^2)\right] \\ \Delta q_y^2 \approx & k^2(\Delta\phi^2+\Delta\delta^2) \\ \Delta q_z^2 \approx & k^2(\Delta\alpha^2+\Delta\beta^2) \end{cases} \qquad (3.18)$$

Thus, the eigenvector coordinate system is essentially rotated in the plane of the sample. This property is particularly interesting for the study of liquid surfaces and smectic membranes where the correlation function is isotropic in this plane. Note that in the limit $\delta \lesssim 10^0$, $\Delta q_x^2 \approx k^2 \left[4\alpha^2\Delta\alpha^2\Delta\beta^2/(\Delta\alpha^2+\Delta\beta^2)\right]$, implying that $\Delta q_x^2 \ll \Delta q_y^2$. This large difference between Δq_x^2 and Δq_y^2 is interesting because the inplane resolution $\Delta q_\perp^2$, where the symbol $\perp$ stands for the component in the plane of the sample (Oxy), determines the accessible $q_\perp$ range (see also sec. 3.3 and sec. 4.4.2). Hence, for liquid systems the low $q_\perp$ range can be measured by q_x while the high $q_\perp$ range is accessible by q_y, making it possible to record the fluctuation spectrum from macroscopic down to molecular dimensions.

3.4.3 Determination of the dispersion angles

The mean square deviations reported in eq. 3.8 and eq. 3.9 account for the incident beam angular dispersion, directly related to the beam divergence, which depends on the optical settings between x-ray source and sample. As illustrated in fig. 3.9, a rectangular cross section of the incoming beam is defined by two orthogonal sets of slits denoted S_{E_i} and S_{E_o}, respectively, perpendicular to $\mathbf{k}_i$ (pre-sample slits). The detector aperture is limited by two orthogonal sets of slits, S_{D_i} and S_{D_o}, respectively, perpendicular to $\mathbf{k}_o$ (detector slits). Fig. 3.11 defines the acceptance angles β^{max}/β^{min} and $\delta^{max}/\delta^{min}$. They describe the distribution of the specularly reflected intensity viewed by the detector during scanning as well as the intensity angular distribution viewed by the detector for a fixed position. The incident beam profiles were recorded by scanning the detector vertically (δ-scan) and horizontally (β-scan). The profiles obtained with the slit settings listed in tab. 3.2 are shown in fig. 3.12. The recorded intensity, $I(\beta)$ and $I(\delta)$, consist of the convolution of the intrinsic half width at half maximum $HWHM_{i,o}$ of the incident beam (assumed to be Gaussian) with the detector slits $S_{D_{i,o}}$, respectively. For simplicity in the following we refer all the equations to $I(\beta)$; hence only the contributions in the scattering plane will
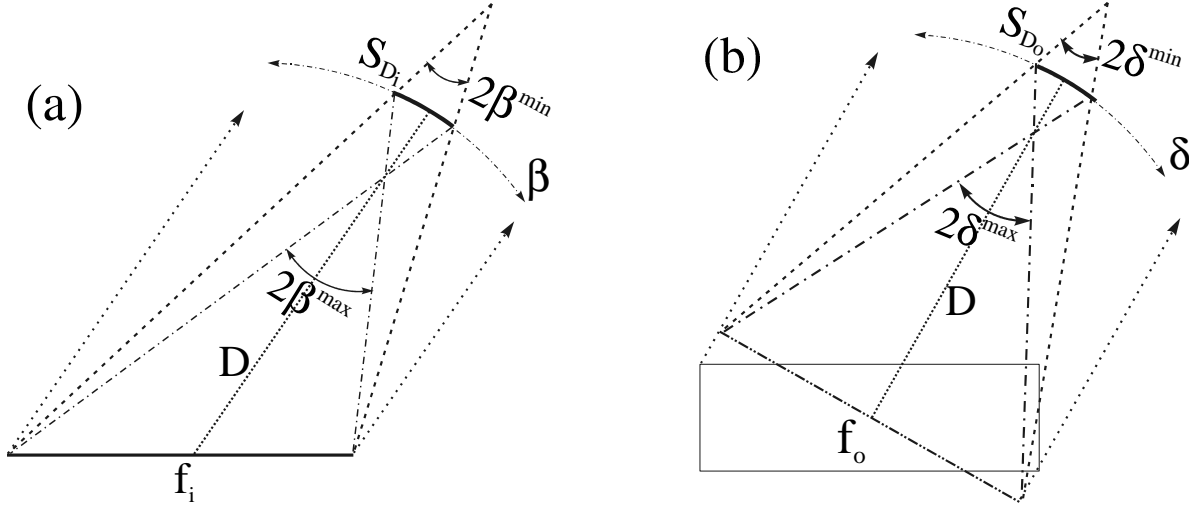
Figure 3.11: *Acceptance angles of the detector in the scattering plane: $2\beta^{min}$ and $2\beta^{max}$ (a), and out of the scattering plane: $2\delta^{min}$ and $2\delta^{max}$ (b). The acceptance angles of the detector entrance are defined by the detector slits $S_{D_{i,o}}$, the footprint $f_{i,o}$ on the sample and the distance D from the detector to the center of the diffractometer.*

be considered. An analogous set of equations can be easily derived for $I(\delta)$, which depends on $HWHM_o$. At a distance D between the detector and the center of the diffractometer (coinciding with O in fig. 3.9) it can be written as:

$$I(\beta) \; = \; I_0 \exp\left(-\frac{\beta^2 \ln 2}{HWHM_i^2}\right) \; * \; \Pi(\beta), \tag{3.19}$$

with:

$$\Pi(\beta) = \begin{cases} 1 & \text{if } 2|\beta| \leq \arctan(S_{D_i}/D) \\ \\ 0 & \text{elsewhere.} \end{cases}$$

To obtain the divergence $\Delta\alpha$ of the beam from the $HWHM_i$ the contribution from the physical width (assumed to be Gaussian) must be removed:

$$\Delta\alpha = (HWHM_i^2/(2\ln 2) - \arctan^2(S_{E_i}/D)/12)^{\frac{1}{2}}. \tag{3.20}$$

The corresponding expression for $\Delta\phi^2$ can be obtained simply by substituting $HWHM_i^2$ with $HWHM_o^2$ and S_{E_i} with S_{E_o} in eq. 3.20. The values obtained for the horizontal and vertical divergences are reported in tab. 3.2.

Type of scan	Slit settings (mm)	Angle settings (°)	$\Delta\alpha$ (°)	$\Delta\phi$ (°)
Rocking scan	$S_{E_i} = 0.1$ $S_{E_o} = 0.2$ $S_{D_i} = S_{D_o} = 0.5$	$\|\omega\| \leq 1.2$ $\phi = \delta = 0$	0.043	0.013
Rocking scan	$S_{E_o} = S_{E_i} = 0.1$ $S_{D_i} = S_{D_o} = 1.0$	$\|\omega\| \leq 1.2$ $\phi = \delta = 0$	0.045	0.011
δ-scan	$S_{E_i} = 0.1$ $S_{E_o} = 0.2$ $S_{D_i} = S_{D_o} = 0.5$	$\alpha = \beta = 1.2$ $\phi = 0$ $0 \leq \delta \leq 8$	0.043	0.013

Table 3.2: *Resolution settings used for the experiments presented in fig. 3.12a (row 1 and 3) and fig. 3.12b (row 2).*

The mean square deviations $\Delta\beta^2$ and $\Delta\delta^2$ are related to the acceptance solid angle of the detector, which depends both on the illuminated area of the sample and the detector slits, as shown in fig. 3.11 . The incident beam divergence can be used to evaluate the effective footprint $f_{i,o}$ in and out of the plane of incidence, respectively. Two accepting angles J^{min} and J^{max} (where $J = \beta, \delta$) define the angular distribution p of the intensity entering the detector aperture. For $D \gg max(f_{i,o} \sin J, S_{D_{i,o}})$, p has a trapezoidal form with top $2J^{min}$ and base $2J^{max}$. Explicitly, p reads:

$$p(J') = \begin{cases} 1/(J^{max} + J^{min}) & \text{if } |J'| < J^{min} \\ (J^{max} - J')/\left[(J^{max})^2 - (J^{min})^2\right] & \text{if } J^{min} > J' > J^{max} \\ 0 & \text{if } |J'| > J^{max} \end{cases} . \qquad (3.21)$$

We replace this trapezoidal distribution by a Gaussian distribution giving the same mean square values, which leads to:

$$\Delta J^2 = \frac{1}{6}\left[(J^{min})^2 + (J^{max})^2\right], \qquad (3.22)$$

with J^{max} and J^{min} given by:

$$\begin{aligned} J^{max} - J^{min} &\approx \frac{max(f_{i,o} \sin J, S_{D_{i,o}})}{D} \\ J^{min} &\approx \frac{|f_{i,o} \sin J - S_{D_{i,o}}|}{2D}, \end{aligned} \qquad (3.23)$$
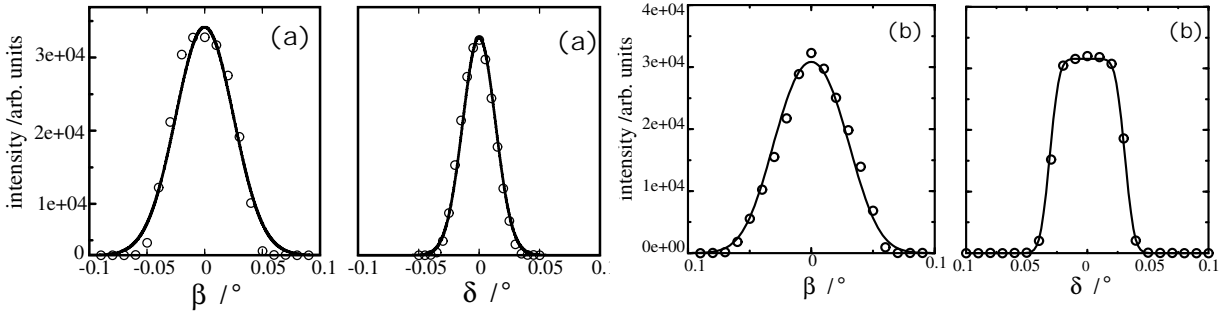
51

Figure 3.12: *Typical beam profiles as used for the rocking scans and for the δ-scans to be discussed in the next chapter. Experimental data (circle) and fits using eq. 3.19 (solid lines) are shown. The corresponding angular dispersions are reported in row 1 and 3 (a) and row 2 (b) of tab. 3.2.*

Note that at large J the possible presence of guard slits, positioned just after the sample to limit the background noise, may lead to a cutoff in the detector acceptance angles [62].

3.5 Fitting specular reflectivity experiments

In sec. 2.2 and sec. 2.4 we have derived formulas that relate the reflected intensity via a convolution with the resolution to the density profile across a smectic membrane. What is left is to explain how to model this electron density profile inside a smectic membrane and subsequently how to perform the fitting to the specular reflectivity data.

In principle two approaches can be used to construct the electron density profile. Phenomenologically it can be expressed in a Fourier series, retaining as many terms as needed for the correct fitting of the data [63]. Alternatively the starting point can be chosen in the molecular formfactor. We shall follow this latter approach.

Smectic A liquid crystals are layered structures in which each smectic layer is about the length of a (stretched) molecule. The electron density modulation is in general due to the central aromatic core having a higher electron density than the alkyl tails. This can be expressed by approximating the electron density profile within a layer by a box-function as shown in of fig. 3.13a. The total thickness of the layer is obviously $d = 2L_1 + L_2$. The box-model must be centro-symmetric because the (asymmetric) molecules have equal probabilities to be oriented up or down [2]. As a comparison fig. 3.13b shows two adjacent molecules of 4O.8 in a smectic layer. The box-model shown in fig. 3.13a is the so-called smectic layer form-factor, that in principle consists of the average of an up and down oriented molecular form factor.
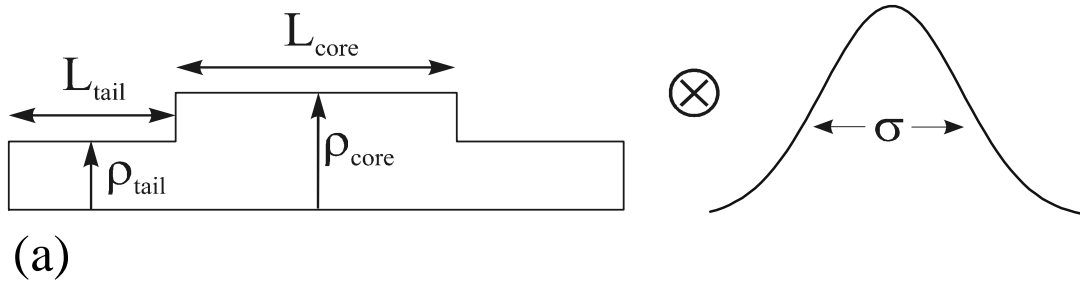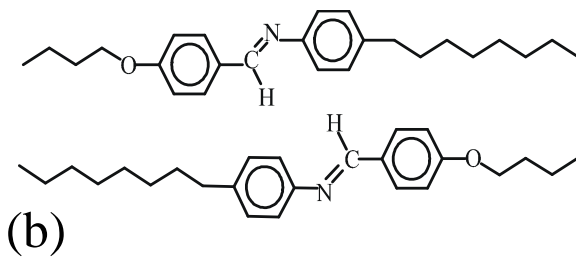
Figure 3.13: *(a) Box model used to represent the electron density of a smectic layer. In order to take the fluctuations into account, it is convoluted with a Gaussian function; σ represents the width of the distribution of the amplitude of the fluctuations. (b) Two molecules of 4O.8 with opposite up-down orientations.*

Using the box model without thermal fluctuations the electron density profile of a two-layers smectic membranes could be approximated as shown in fig. 3.14a. At any finite temperature, the thermal energy is dissipated through a combination of collective fluctuations of the layers and fluctuations of the individual molecules around their centres of gravity [2]. The fluctuations will smear out the electron density distribution as schematically pictured in fig. 3.14b. This effect can be introduced by assuming a normal distribution of the fluctuations and convoluting the box-model with a Gaussian function (fig. 3.13a). The parameter σ indicates the r.m.s. amplitude of the (Gaussian) distribution of the fluctuations amplitudes an can in principle differ for each interface.

To fit the experimental data the REFLAN software package has been used [64, 65]. It calculates the reflected intensity using the recursive matrix formalism discussed in sec. 2.2. Each smectic layer is simulated using the model of fig. 3.13a. The fitting of the experimental data to the calculated structure consists of two successive stages. In the first stage the program finds the local minimum difference corresponding to the initial trial structure. During the second step
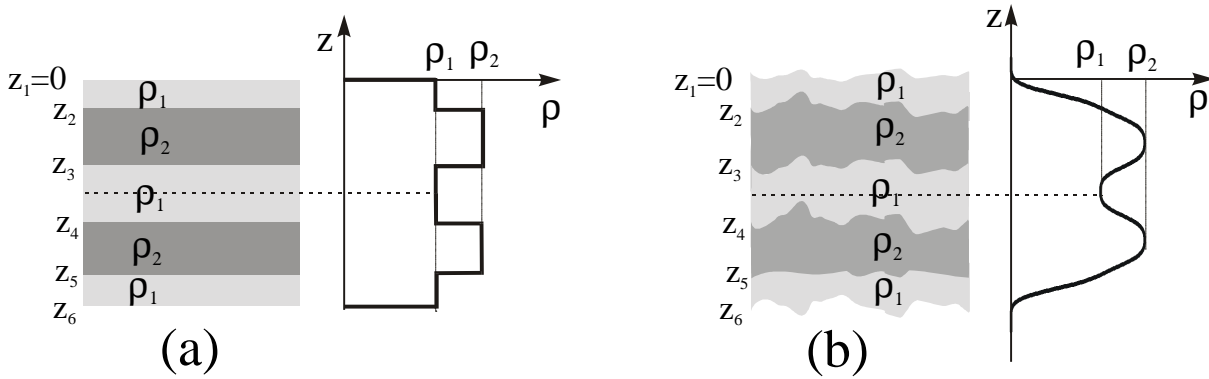
Figure 3.14: *Electron density modulation and corresponding profiles in a two-layer smectic membrane. (a) Without thermal fluctuations, $\rho(z)$ is a discontinuous function of z ; (b) In the presence of fluctuations, $\rho(z)$ becomes continuous.*

this structure is progressively distorted by exploring the whole parameter space and eventually finding the global minimum. The method used is known also as successive descent from local minima. Constraining the parameters makes it possible to bias the process towards physically significant solutions. Before comparing the model function to the experimental data it is convoluted with the resolution (see eq.3.14). During the minimization process the experimental errors are taken into account by weighting the data accordingly.

Chapter 4

Thermal fluctuations in smectic membranes

In this chapter specular and diffuse reflectivity data on smectic membranes of 4O.8 are presented. The fluctuation profiles for SmA membranes of various thickness have been obtained from specular reflectivity experiments. The fluctuation amplitude of the central layers is found to increase with the sample thickness, while it remains approximately constant at the air interfaces. The layer displacement-displacement correlation function $g_{mn}(\mathbf{r}_\perp, z, z')$ has been studied by means of diffuse reflectivity. One single set of fitting parameters can account for the diffuse intensity from all the membranes studied, regardless their thickness. The elastic parameters from fits of the diffuse data were used to calculate hydrodynamic fluctuation profiles through the membranes. These profiles are rather flat compared to the experimental ones.

The reflectivity results for SmA membranes have been compared with the corresponding data in the CrB phase. In this phase, the fluctuation profiles from specular reflectivity hardly change with the sample thickness though still some damping occurs at the air interfaces. The diffuse reflectivity results are very similar to those of the corresponding SmA membranes. These findings indicate that CrB membranes can also be considered as fluctuating systems, which is attributed to the small value of the shear elastic constant C_{44}.

4.1 Introduction

In this chapter results from specular and diffuse reflectivity on SmA membranes as a function of membrane thickness will be discussed. Specular reflectivity is sensitive to the (average) density profile and to the amplitude of the fluctuations of the smectic layers along **n** [63, 66]. Hence the r.m.s. amplitude of the thermal fluctuations of each smectic layer can be extracted from the analysis of the specular reflectivity data (see sec.2.4). By diffuse reflectivity one is able to study the spectral dependence of the interlayer displacement-displacement correlation function, $g_{mn}(\mathbf{r}_\perp, z, z')$ of the smectic layers. In eq.2.29 the x-ray intensity reflected along $q_\perp$ (with $\perp = x, y$) has been expressed as a function of the total interlayer displacement-displacement correlation function, g_{mn}, defined in eq.2.27. The central part of the considerations is the displacement-displacement correlation function $\langle u_m(0)u_n(\mathbf{r}_\perp)\rangle$ and the average layer fluctuation amplitudes $\langle u_n^2(0)\rangle$. In sec.4.2 the Landau-de Gennes theory for fluctuating smectics will be summarized, first for bulk phases. Then in sec.4.2.2 $g_{mn}(\mathbf{r}_\perp, z, z')$ will be given for smectic membranes, in which case the theory is extended with a surface term to take the presence of the free surfaces into account [67]. This model predicts that above a characteristic in-plane wavelength, defined as $R_c = \sqrt{2\gamma L/B}$, SmA membranes fluctuate conformally, i.e. all the layers fluctuate in unison. At shorter wavelengths a cross-over to independent layer fluctuations takes place. This prediction has been confirmed in ref. [30] for SmA membranes of di-heptyl-azoxy-benzene (7AB). However, the amplitude of the fluctuations calculated from the analysis of the diffuse reflectivity, with the extended Landau-de Gennes theory, was considerably smaller than found experimentally by specular reflectivity. To account for this discrepancy a contribution from local fluctuations was postulated in addition to the long-wavelength hydrodynamic fluctuations. The authors conclude that these local fluctuations (originally proposed in [68]) must have a steep profile throughout the thickness of the film. They constitute a significant fraction of the total fluctuations amplitude [66, 68, 69].

In the present study we discuss the specular and the diffuse results as a function of the film thickness. The amplitude of the fluctuations in the center of the SmA membranes diverges faster with film thickness than predicted by the bulk Landau-de Gennes theory [67, 68]. Evidently in the range of thicknesses studied decreasing surface damping and not the Landau-Peierls instability is still the dominant effect.

In the last part of the chapter, the results for SmA membranes are compared to CrB ones. The exact nature of the CrB phase has been an intriguing question for quite some time [34].

In the late seventies of the last century the 3D nature of the long-range positional order has been established by the observation of a solid-like shear response (with elastic constant C_{44}) between the CrB layers [5, 70]. These findings were confirmed by x-ray diffraction [8, 9]. As a consequence, a term proportional to $C_{44}q^2$ occurs in the elastic free energy, which eliminates the Landau-Peierls instability (see sec. 4.2.3). Nevertheless intense diffuse scattering in the vicinity of the Bragg peaks has been observed, tentatively interpreted as due to soft shear waves [8]. Indeed the corresponding shear modulus was found to be few orders of magnitude smaller than the other elastic constants [71]. The reflectivity results presented in this chapter (together with the the XPCS results to be presented in ch. 6) definitively prove the fluctuating nature of CrB membranes. From diffuse x-ray reflectivity the spectral dependence of the fluctuations in the CrB phase is found to be very similar to that in the SmA phase. However, the fluctuation profiles for various film thickness are constant in contrast to the SmA situation.

4.2 Thermal fluctuations, theory

In the following the continuous version of the elastic theory for smectic phases will be outlined [67, 68, 72]. First, the Landau-de Gennes free energy for bulk SmA systems will be introduced. Then the necessary modifications to the free energy for SmA membranes due to the presence of free surfaces will be summarized in sec. 4.2.2. Only the final result will be shown as derived in ref. [67], which will be used for the analysis of the diffuse x-ray reflectivity data. Finally the result for the SmA phase will be compared with the free energy of an hexagonal crystal in the easy-shear approximation in sec. 4.2.3.

4.2.1 Bulk smectic A phase

Smectic layers are two-dimensional fluids; therefore the free energy can be described by the layer displacement $u(\mathbf{r})$ from the equilibrium position $z = nd$. The terms that may enter the free energy must be invariant to operations that leave the system unchanged. Thus, the free energy can only depend on even derivatives of $u(\mathbf{r})$. In the harmonic approximation ∇u is assumed to be small, which means that the layers are neither very much tilted from the x, y-plane nor strongly compressed [2]. These symmetry considerations lead to the following expression for

the Landau-de Gennes free energy [2, 3]:

$$F_B = \frac{1}{2} \int d^3r \left[B \left(\frac{\partial u(\mathbf{r})}{\partial z} \right)^2 + K [\Delta_\perp u(\mathbf{r})]^2 \right], \tag{4.1}$$

where the positional vector $\mathbf{r}$ has components $(\mathbf{r}_\perp, z)$ and z is perpendicular to the interface; $\Delta_\perp$ indicates the Laplacian. Note that the term $(\nabla_\perp u)^2$ is forbidden because the layers can slide on each other without any energy cost. The absence of this term is a reason to take the higher order derivative term into account. The integration is carried out over the volume of the system.

In order to calculate the average layer fluctuation amplitude, $\langle u^2(\mathbf{r}) \rangle$, the free energy has to be transformed to reciprocal space. The displacement $u(\mathbf{r})$ can be written as

$$u(\mathbf{r}) = (2\pi)^{-3} \int d^3q\, u(\mathbf{q}) \exp(i\mathbf{q} \cdot \mathbf{r}) \quad, \tag{4.2}$$

and the free energy becomes

$$F_B = \frac{1}{2(2\pi)^3} \int d^3q \left[Bq_z^2 + Kq_\perp^4 \right] |u(\mathbf{q})|^2. \tag{4.3}$$

The free energy can be written as a sum of contributions $F_B'(\mathbf{q})$ for each wave vector $\mathbf{q}$, because $\langle u(\mathbf{q})u(\mathbf{q}') \rangle = 0$, if $\mathbf{q} \neq -\mathbf{q}'$, so that

$$F_B = \frac{1}{(2\pi)^3} \int d^3q\, F_B'(\mathbf{q}) \quad, \tag{4.4}$$

with

$$F_B'(\mathbf{q}) = \frac{1}{2} \left[Bq_z^2 + Kq_\perp^4 \right] |u(\mathbf{q})|^2. \tag{4.5}$$

According to the equipartition theorem each normal mode (i.e. each independent quadratic term) in the free energy has on average $\frac{1}{2}k_B T$ of energy and therefore

$$\frac{1}{2}k_B T = \frac{1}{2} \left[Bq_z^2 + Kq_\perp^4 \right] \langle |u(\mathbf{q})|^2 \rangle. \tag{4.6}$$

Thus

$$\langle |u(\mathbf{q})|^2 \rangle = \frac{k_B T}{Bq_z^2 + Kq_\perp^4}. \tag{4.7}$$

Assuming that different modes of oscillation are uncorrelated and using eq. 4.2 and eq. 4.6, one can write the mean square value of the amplitude of the layer displacement in the following way:

$$\langle u(\mathbf{r})^2 \rangle = \frac{1}{(2\pi)^3} \int d^3q \langle |u(\mathbf{q})|^2 \rangle = \frac{k_B T}{(2\pi)^3} \int \frac{d^3q}{Bq_z^2 + Kq_\perp^4}. \tag{4.8}$$

Wavelengths larger than the sample size L, normal to the layers, and the sample size W in the plane of the layers, are not possible. Similarly, modes with wavelengths shorter than the layer spacing or lateral molecular spacing a_0 are not allowed. The integration boundaries are $2\pi/W \le q_\perp \le 2\pi/a_0$ and $2\pi/L \le q_z \le 2\pi/d$. As $W \gg L$ and $a_0 < d$, the limits of integration can be expanded: $W \to \infty$ and $a_0 \to 0$. Consequently,

$$\langle u(\mathbf{r})^2 \rangle = \frac{k_B T}{4\pi^2} \int \int dq_z dq_\perp \frac{q_\perp}{Bq_z^2 + Kq_\perp^4} = \frac{k_B T}{8\pi\sqrt{KB}} \ln\left(\frac{L}{d}\right). \tag{4.9}$$

Note that a similar expression but with cutting by W and a_0 can be obtained by integrating over q_z (without cutting) and then over $\mathbf{q}_\perp$. One can see that $\langle u^2(\mathbf{r}) \rangle$ diverges logarithmically with L. This is called the Landau-Peierls instability, as a result of which for large L the fluctuations become of the order of the layer spacing, which means that the layer structure is wiped out. Using the following values $B = 10^6$ N/m^2, $K = 10^{-11}$ N, $k_B T = 5 \times 10^{-21}$ Nm, $d \approx 3$ nm, eq.4.9 gives $\sigma = \langle u^2(0,z) \rangle^{-1/2} \approx 1$ nm for a 1 m thick sample. Therefore, in all practical circumstances the layer displacement amplitude is significantly smaller than the layer spacing and consequently the smectic layers are still well defined.

As a result of the Landau-Peierls instability SmA systems possess algebraic decaying (quasi-long range) order. In other words, the positional correlation of the layers decays as $r^{-\eta}$, where η is small (see ch.1). As a consequence, the x-ray reflections due to the layer structure are not δ-functions as it would be expected for a crystal. Instead singularities in $I(\mathbf{q})$ with algebraic decaying tails are observed [18]. These singularities have the form [73,74]:

$$I(q_\perp = 0, q_z) \quad \sim \quad (q_z - q_m)^{-2+\eta_m} \tag{4.10}$$

$$I(q_\perp, q_z = q_m) \quad \sim \quad q_\perp^{-4+2\eta_m}. \tag{4.11}$$

where η_m and q_m are given by:

$$\eta_m = \frac{q_m^2 k_B T}{8\pi\sqrt{KB}} \qquad q_m = \frac{2\pi m}{d}, \tag{4.12}$$

with $m = 0, 1, 2, \ldots$ In this notation, $q_1 \equiv q_0$ and $\eta \equiv \eta_0 \equiv \eta_1$. This behaviour has been observed in both thermotropic smectics [12] and in lyotropic lamellar phases [13]. There is a finite number of peaks according to eq.4.10; for large q_z where $\eta_m > 2$ one can find cusps in the intensity on the positions of the Bragg peaks instead of the divergences. Thus the maximum intensity of the quasi-Bragg peaks decreases rapidly with increasing m. In fact, in most thermotropic smectics only the first Bragg peak is clearly present, which is expected to be at least partially related to the increasing value of η_m with m.

4.2.2   Smectic A membranes

In order to calculate the displacement-displacement correlation function for smectic membranes the effect of the outer surfaces must be included. The total free-energy can be written as the sum of the bulk contribution (eq.4.1) and a surface contribution F_S that can be expressed as [68]:

$$F_S = \frac{1}{2}\gamma \int d^2r \left[(\nabla_\perp u(\mathbf{r}_\perp, z = L/2))^2 + (\nabla_\perp u(\mathbf{r}_\perp, z = -L/2))^2 \right]. \tag{4.13}$$

The surface terms, which are proportional to the surface tension γ, describe the energy cost associated with an increase of the surface area of the two free surfaces located at $z = L/2$ and $z = -L/2$.

In order to analyze x-ray scattering data from SmA membranes, one needs to express the free energy in terms of the wave-vector transfer in the reciprocal space. The result depends on the displacement-displacement correlation function. An expression has been given in ref. [67] and here only the final result is reported. After defining:

$$\nu = \gamma/\sqrt{KB}, \qquad \lambda = \sqrt{K/B}, \qquad \rho = r_\perp/\sqrt{\lambda L},$$

the correlation function can be written as:

$$g(r_\perp, z, z') = \langle [u(\mathbf{r}_\perp, z) - u(0, z')]^2 \rangle = \frac{k_B T}{8\pi\sqrt{KB}} \int_{\xi_1}^{\xi_0} d\xi \frac{1}{\xi[(1+\nu)^2 - (1-\nu)^2 \exp(-2\xi)]}$$
$$\times \left[f(\xi, 2z, z_0) + f(\xi, 2z', z_0) - 2J_0\left(\rho\sqrt{\xi}\right) f(\xi, z_+, z_-) \right], \tag{4.14}$$

in which the following cut-offs have been introduced $\xi_0 = L\lambda(2\pi/\varepsilon)^2$, $\xi_1 = L\lambda(2\pi/\Lambda)^2$ for the high and low integration limit, respectively. Furthermore $\xi = L\lambda q_\perp^2$, $z_+ = z + z'$ and $z_- = |z - z'|$ (with minimum value z_0) and J_0 is the Bessel function of order zero, while the function f is given by

$$f(\xi, z_+, z_-) = 2(1 - \nu^2) \exp(-\xi)\cosh(\xi z_+/L) + (1+\nu)^2 \exp(-\xi z_-/L)$$
$$+ (1 - \nu)^2 \exp[-\xi(2 - z_-/L)]. \tag{4.15}$$

Eq.4.14 is the expression for the correlation function used in the analysis of the experimental results. A value of $z_0 \simeq d/4$ was chosen to reproduce essentially the results from the original discrete model developed by Hołyst [68]. The integral of eq.4.14 diverges not only with z, but also with the in-plane cut-offs, ε and Λ. Since fluctuations cannot occur with wavelength smaller than the lateral molecular size, for the short-wavelength cut-off $\varepsilon = a_0 = 0.4$ nm has been

chosen. Following ref. [28] a value of $\Lambda = 50\,\mu\text{m}$ was used for all the calculations in the rest of this chapter. It corresponds to the maximum in-plane wavelength of the fluctuations observable experimentally. The chosen value is given by the projection of the transverse coherence length of the x-ray beam at the first Bragg peak position.

In refs. [27, 30] it was shown that in SmA membranes the layers fluctuate conformally (i.e. "unisono") up to in-plane length scales of the order of tens of nm. A characteristic in-plane length R_c can be defined such that below R_c the fluctuations are not conformal. An estimate for R_c for thin SmA membranes has been given in [30]:

$$R_c = \sqrt{2\gamma L/B}. \tag{4.16}$$

This estimate will be compared to the experimental results in sec.4.4.2. From eq.4.16 it is clear that incompressible films are fully conformal: a collection of incompressible layers (corresponding to $B \to \infty$) must fluctuate in unison at all possible wavelengths. Vice versa, R_c is finite for any real values of B. In the high-compressibility limit for SmA membranes fluctuating conformally $g_{mn}(r_\perp)$ does not depend on n,m [67] and:

$$g(r_\perp, z, z') \equiv g(r_\perp) = \frac{k_B T}{2\pi\gamma} \left[\ln(r_\perp/r_0) + K_0(r_\perp/r_0) + c - \ln(2) \right], \tag{4.17}$$

where K_0 is the modified Bessel function, $c \approx 0.5772$ is Euler's constant and $r_0 = (LK/2\gamma)^{1/2}$.

4.2.3 Crystalline smectic B membranes

To take into account for the crystal structure of the CrB phase, one considers the elastic energy associated with the deformations of a 3D hexagonal crystal. These are described by the strain tensor

$$u_{ij} = \frac{1}{2} \left(\nabla_j u_i + \nabla_i u_j \right), \tag{4.18}$$

where $\mathbf{u}$ is the displacement vector. The elastic energy F for solids is quadratic in u_{ij}:

$$F = \frac{1}{2} \int d^3 r K_{ijlm} u_{ij} u_{lm} . \tag{4.19}$$

The structure of the elastic-constant tensor K_{ijlm} depends on the symmetry of the system. A CrB membrane is a uniaxial crystal and the elastic tensor is defined by five elastic constants [3]. The stress tensor can now be expressed as

$$\sigma_{ij} = \frac{\delta F}{\delta u_{ij}} = K_{ijlm} u_{lm} . \tag{4.20}$$

The CrB phase has a finite shear modulus C_{44}, which is abnormally small [5, 71]. For this reason, the conventional analysis of bending [75], which ignores shear, is not valid. Instead all in-plane deformations are neglected, while shear deformations are considered to be well developed (easy-shear approximation). Mathematically, this approximation means that the displacement **u** can be expressed as

$$u_j(\mathbf{r}) = \delta_{jz} u(x, y, z).$$ (4.21)

The corresponding strain tensor elements are:

$$
\begin{aligned}
u_{xz} &= \frac{1}{2}\frac{\partial u}{\partial x}, \; u_{yz} = \frac{1}{2}\frac{\partial u}{\partial y}, \; u_{zz} = \frac{\partial u}{\partial z}, \\
u_{xx} &= u_{yy} = u_{xy} = 0.
\end{aligned}
$$

Using these elements the free energy of a uniaxial crystal becomes

$$F_{uniax} = \frac{1}{2}\int d^3 r \left[C_{33}(\nabla_z u)^2 + \frac{1}{4}C_{44}(\nabla_\perp u)^2 \right].$$ (4.22)

The coefficient C_{33} corresponds to the smectic compressibility coefficient; hence it will be denoted as B, keeping in mind that its value can differ from the SmA one. The shear elastic coefficient C_{44} is finite but small, so it is justified keeping the next-order term with respect to in-plane derivatives, which is the dominant term in the SmA phase. Therefore, the elastic energy of the CrB phase can be written as:

$$F = \frac{1}{2}\int d^3 r \left[B(\nabla_z u)^2 + K(\Delta_\perp u)^2 + \frac{1}{4}C_{44}(\nabla_\perp u)^2 \right].$$ (4.23)

A crucial consequence of shear elastic deformations is that they produce a term proportional to $(\nabla_\perp u)^2$, which is forbidden in the SmA phase in which the layers slide freely. The absence of such a term leads to the Landau-Peierls instability in the SmA phase (see sec.4.2.1), and any finite C_{44} removes the divergence of the mean-square fluctuations with the size of the system. However, the presence of such a term does not affect the layer compression and bending rigidity. In practice, for smectic membranes the main effect of the CrB lattice via C_{44} can be incorporated as an effective renormalization of the surface tension:

$$\gamma_{eff} = \gamma + \frac{LC_{44}}{8}.$$ (4.24)
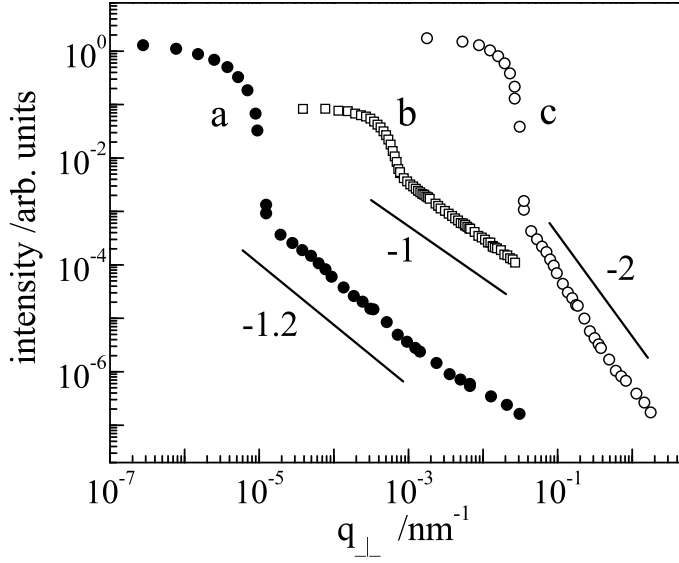
Figure 4.1: *Diffuse reflectivity scans of an 8-layer SmA membrane of 4O.8 measured at $q_z = 2.2$ nm^{-1}. In the rocking scan (b) only q_x is varied, while in the δ-scan both q_x (a) and q_y (c) are varied. The solid lines are best fits as discussed in the text. (b) has been shifted down for clarity.*

4.3 Fitting of diffuse reflectivity data

Starting point for the analysis of the diffuse scans is eq. 2.29, which we shall write for the present purpose in the form:

$$S(\mathbf{q}) = R_F \int d\mathbf{r}_\perp \exp(\iota \mathbf{q}_\perp \cdot \mathbf{r}_\perp) C(q_z, r_\perp), \tag{4.25}$$

where $C(q_z, r_\perp)$ is the layer-layer correlation function given by:

$$C(q_z, r_\perp) = d \sum_{m,n}^{N} \exp\left[\iota q_z(m-n)d - \frac{1}{2} q_z^2 g_{mn}(r_\perp) \right] .$$

Convoluting eq. 4.25 with the resolution (eq. 3.13) leads to the final equation:

$$I(\mathbf{q}) = R_F \left[\int \int dx dy \, C(q_z, r_\perp) \exp\left(\iota(q_x x + q_y y) - \frac{1}{2} x^2 \Delta q_x^2 - \frac{1}{2} y^2 \Delta q_y^2 \right) \right] * \exp\left(-\frac{1}{2} \frac{q_z^2}{\Delta q_z^2} \right) . \tag{4.26}$$

The calculation of R_F has been done in the framework of the first Born approximation, but taking refraction into account by substituting q_z with $q_z' = \sqrt{q_z^2 - q_c^2}$ (see sec. 2.3). In the reflectivity geometry the convolution in the (xy)-plane and in the z-direction can be carried out separately. The subscript $\perp$ represents x in the case of rocking scans, and x, y for δ-scans. Accordingly, either eq. 3.15 or eq. 3.18 can be used for the resolution parameters.

In the case of systems with a finite correlation distance, $C(q_z, r_\perp)$ would decay exponentially to a constant value $C(q_z, \infty) \sim \exp(-q_z^2 \langle u(0)^2 \rangle)$. Integration of this constant with $\exp(\iota \mathbf{r}_\perp \cdot \mathbf{q}_\perp)$

provides a delta-function [43]. In such a situation there are good reasons to split the total intensity into two parts that can be analyzed separately. The first one is the specular reflectivity due to $C(q_z, \infty)$; the second is the diffuse scattering due to $[C(q_z, r_\perp) - C(q_z, \infty)]$ in the integrand. The Landau-Peierls instability modifies the picture considerably for the case of smectic membranes. For these samples $C(q_z, r_\perp)$ decays algebraically as $r_\perp^{-\eta}$ and only the convolution with the resolution function forces the integral in eq.4.26 to converge to a finite value. This creates numerical problems discussed by [58]. The accessible range for the fluctuation spectrum now depends directly on the resolution function.

Fig.4.1 shows a δ-scan and a rocking scan of an 8-layer SmA membrane of 4O.8. By measuring both types of scan, an interval of in-plane wavelengths from about 10 μm down to approximately 5 nm can be investigated. S_{E_i} and S_{E_o} were set to 0.1 and 0.2 mm, respectively, leading to incoming divergences $\Delta\alpha = 0.043°$ m and $\Delta\phi = 0.013°$ (see sec.3.4.3). In addition $S_{D_i} = S_{D_o} = 0.5$ mm was used. Note that the divergence in the the plane of incidence is much larger than in the perpendicular direction, which makes the diffractometer particularly suitable for δ-scans. The data at the high $q_\perp$ range (right curve) relate to the q_y-part of a δ-scan, to the left follows a rocking scan and then at the lowest $q_\perp$-range the q_x-part of the same δ-scan (see sec.3.4). All the curves exhibit a large 'plateau' region at low $q_\perp$, followed by an abrupt fall-off at $q_\perp \simeq \Delta q_\perp$ and a smooth negative slope at higher $q_\perp$. The fall-off separates specular and off-specular dominated regions. This can be understood by geometrical considerations. In the present situation $\Delta q_\perp^2$ is the mean square value of the intensity distribution $I(q_z, q_\perp')$ collected by the detector when scanning around $q_\perp = 0$. Around the center of this distribution, the detector aperture effectively collects the specularly reflected beam. The diffuse region is influenced both by the resolution and the correlation function, where the resolution depends on the specific geometry used. This leads to a further division into two parts. First, there is a region where the logarithmic term in $g(r_\perp)$ is dominant (in between the 'plateau' and high $q_\perp$ regions). In this region, the intensity follows a law close to an algebraic decay of the form:

$$I(q_\perp) \sim \int d\mathbf{r}_\perp \exp(\iota \mathbf{q}_\perp \cdot \mathbf{r}_\perp) r_\perp^{-\eta} \sim q_\perp^{-D+\eta} . \tag{4.27}$$

For the case of 4O.8, $\eta \simeq 0.04$ while $D = 1$ or 2 depending on whether a one or two-dimensional integration is performed. In fig.4.1, the q_y-part of the δ-scan (right curve) follows a law according to $q_\perp^{-2+\eta}$ as a result of the two-dimensional integration needed. For the rocking scan the diffuse part shows a slope of -1 corresponding to a one-dimensional integration and thus a behavior as $q_\perp^{-1+\eta}$. However, to achieve this situation, S_{D_o} had to be increased from 0.5 to 1
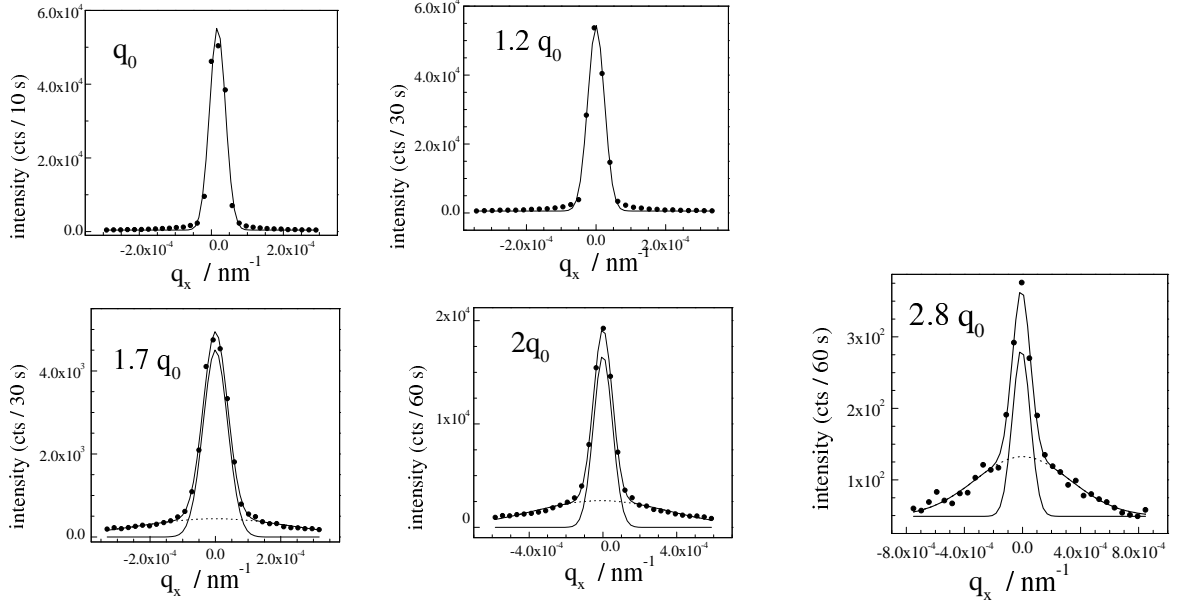
Figure 4.2: *Rocking scans at different q_z positions along the specular ridge for a 38-layer SmA membrane. For $q_z \gtrsim 1.5q_0$ the specular component (full line) has to be evaluated by subtracting the diffuse component (dotted line) (see sec. 2.4.1)*

mm; the resulting divergences are reported in row 2 of tab. 3.2. At the original value S_{Do} the integration over y could still not be fully disregarded and a slope of -1.25 was found, see [59]. The same intermediate value is found in fig. 4.1 for the q_x-part of the δ-scan. Finally, for values of $q_\perp \gtrsim 0.01$ nm^{-1} there is a nonlinear deviation from the algebraic decay. This higher-order effect is mainly due to the bending modulus K in the correlation function, as shown in fig. 4.10. This can be well understood from the simplified form of $g(q_z, r_\perp)$ in eq. 4.17.

4.4 Thermal fluctuations, experimental results

4.4.1 Specular reflectivity

In this section we present specular reflectivity results for smectic membranes of various thickness in the SmA and in the CrB phase. Before analyzing the experimental results in terms of the specular signal, possible diffuse contributions at the specular ridge have to be evaluated. As it has been shown in fig. 2.6 this could lead to some corrections. In fig. 4.2 a series of rocking
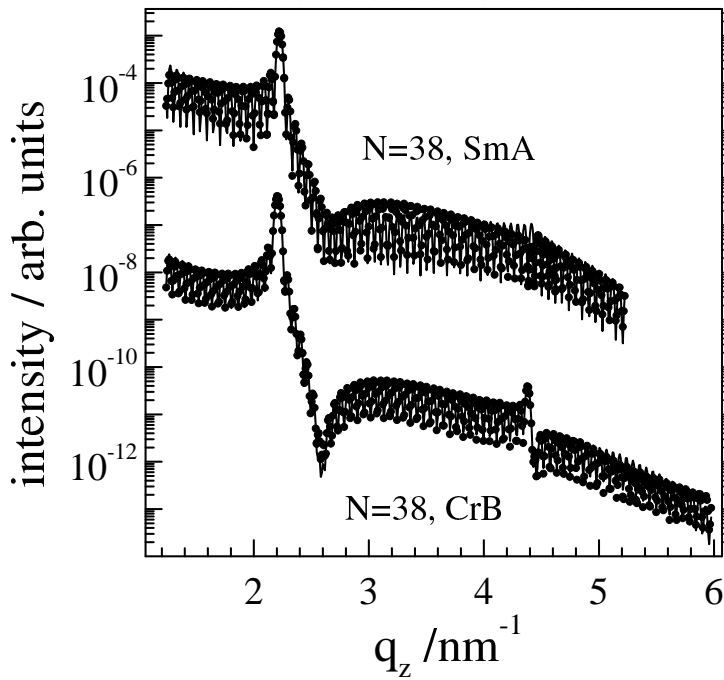
Figure 4.3: *Specular reflectivity data (filled circles) for a 38-layer smectic membrane in the SmA (62.5° C, upper curve) and in the CrB phase (47.0° C, lower curve). The lower curve has been shifted for clarity. The lines represent the best fit to the data.*

scans is shown at different q_z positions together with Gaussian fits corresponding to the specular and diffuse parts, respectively. Evidently only data for $q_z \gtrsim 1.5q_0$ (where q_0 is the first Bragg position) need to be fitted with two Gaussian functions; for smaller q_z the contribution of the diffuse scattering is negligible. For the rocking scans shown in fig.4.2 the specular contribution (central narrow Gaussian) has been separated from the diffuse part, and integrated. As the specular part is resolution limited (in contrast to the diffuse one) this gives the 'real' specular signal at the particular q_z-position. Up to about the second Bragg peak the correction is of the same order of magnitude as the experimental errors. Rocking scans have been repeatedly made and analyzed with similar results for the other membranes studied (with the exception of the 80-layer membrane).

In fig.4.3 the specular reflectivity data for a 38-layer SmA membrane are compared with the corresponding curve measured in the CrB phase. In the CrB phase the Bragg peaks become more intense with respect to the corresponding ones in the SmA phase, while also a deeper minimum appears at q_z just above the Bragg peaks. This is the fingerprint of a decreasing amplitude of the fluctuations through the film upon crystallization. diffuse part of the reflected intensity can be disregarded. The data have been fitted with the iterative matrix solution of the Fresnel equations for the reflectivity of the multilayer system using the box-model for the
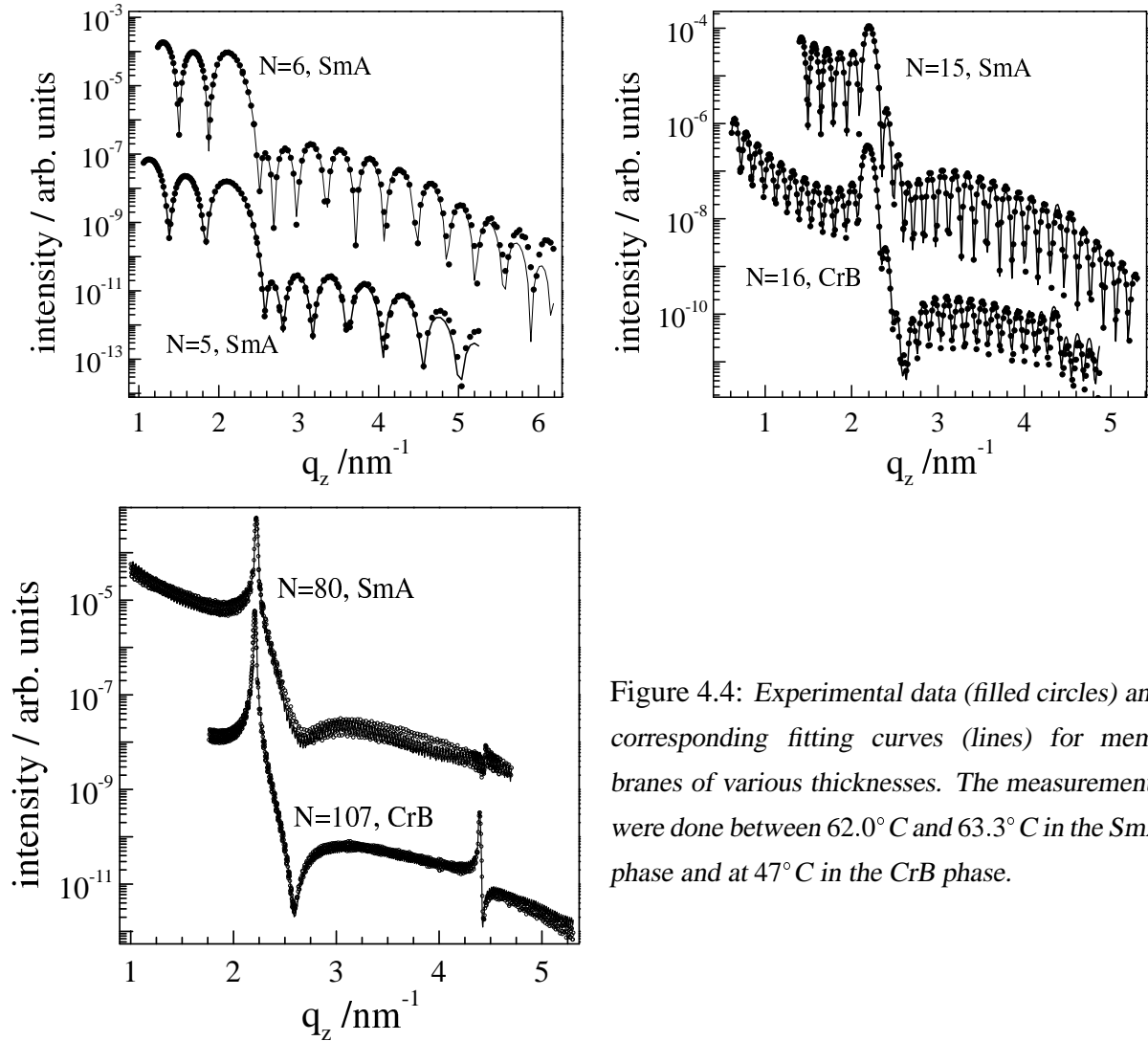
Figure 4.4: *Experimental data (filled circles) and corresponding fitting curves (lines) for membranes of various thicknesses. The measurements were done between 62.0° C and 63.3° C in the SmA phase and at 47° C in the CrB phase.*

electron density profiles, as described in sec. 3.5. Each data set was fitted independently, keeping L_i and ρ_i fixed for the particular set. In contrast σ_i was left free for each smectic layer taking the centro-symmetry of the density profile into account. In order to find a good trial function, initially the q_z-range fitted was limited up to the second Bragg peak. Once the thickness and the overall shape of the profile had been determined for this reduced q_z-range, the minimization was extended to the whole set of measured data. In general, no modifications of the box-model were observed when expanding the fitted range. The attendant changes in the values of σ_i vary from 0.01 nm for the surface layers up to 0.03 nm for the central layers. These numbers are inside the error bars, and we conclude that corrections for the
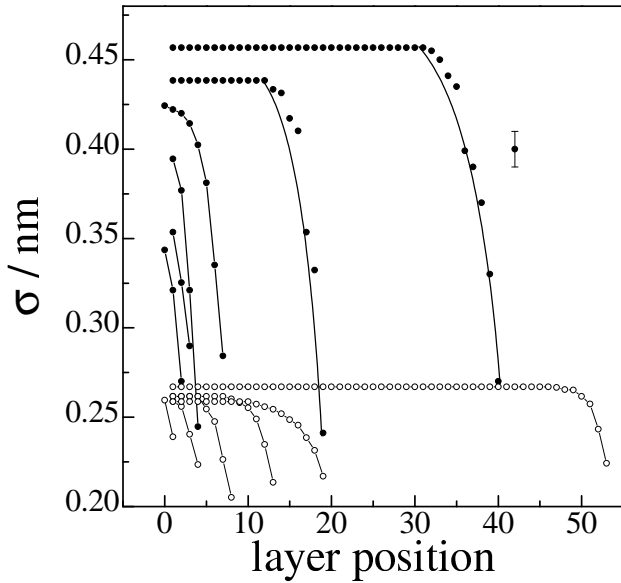
Figure 4.5: *Fluctuation profiles in the SmA phase (filled circles) for 5, 6, 8, 15, 38 and 80-layer membranes, and in the CrB phase (open circles) for 3, 8, 16, 26, 38 and 107-layer membranes as derived from modeling the specular reflectivity data as described in sec. 3.5. A resulting error bar for 95% confidence level is indicated. Only half of the centro-symmetric profiles are shown. The lines are only a guide to the eyes.*

The experimental data and the corresponding fitting curves are shown in fig. 4.4 for various membranes in the SmA and CrB phase. In the absence of reliable data around the critical angle no absolute values of ρ_{core} and ρ_{tail} have been determined. Nevertheless, for the SmA membranes, all calculations converged to $\rho_{core}/\rho_{tail} = 1.57$ and $L_{core}/L_{tail} \approx 2.12$, with $d = 2.85$ nm. The centro-symmetric σ_i profiles are depicted in fig. 4.5, where the origin corresponds to the center of the membrane. The flat top in the SmA profiles of the 38 and the 80-layer membranes is an artifact. The value of σ_i for the central layers was constrained to be constant in order to reduce the number of free parameters. A larger number does not significantly improve the quality of the fitting (i.e. the χ^2 value does not vary more than 1%). The error bar indicates 95% confidence limits as calculated from the differences between the experimental and the model curves.

The amplitude of the fluctuations of the inner layers increases in the SmA phase with film thickness, as shown in fig. 4.5. In contrast, in the CrB phase the amplitude of the fluctuations of the interior layers remains constant. Nevertheless, the fluctuations in the center of the CrB membranes are still relatively large, of the order of 0.25 nm, corresponding to approximately 9% of the smectic layer spacing. There are remarkable similarities between the fluctuations of the surface layers in the two phases. Both for SmA and CrB membranes the surface layer fluctuations are quenched in a similar way, while the resulting σ-values are independent of the membrane thickness.
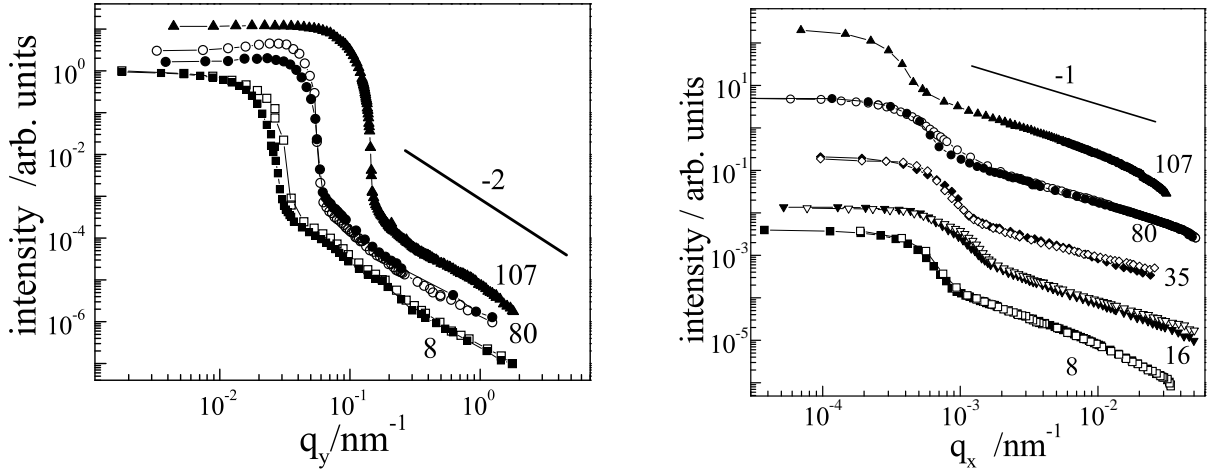
Figure 4.6: δ-*scans (left) and rocking scans (right) of smectic membranes of various thickness; the number of layers is indicated in the picture. Open symbols: SmA phase; filled symbols: CrB phase. All scans have been recorded at $q_z = 2.20$ nm^{-1}, corresponding to the position of the first Bragg peak. The curves have been shifted for clarity. Lines are only a guide to the eye.*

4.4.2 Diffuse reflectivity

Diffuse reflectivity curves for different membrane thickness are shown in fig.4.6. All the curves exhibit a large plateau region at low $q_\perp$-values determined by the resolution, followed by an abrupt fall-off at $q_\perp \sim \Delta q_\perp$ and a smooth negative slope at higher $q_\perp$. The diffuse intensity just after the resolution dominated region decays algebraically with a slope of approximately -1 for rocking scans and approximately -2 for δ-scans (see sec.4.3). The raw data for the SmA and the CrB phase coincide over the whole spectrum probed, see fig.4.6.

The diffuse scattering from SmA membranes has been calculated as discussed in sec.4.3. The solid lines shown in fig.4.7 are best fits to the SmA curves from fig.4.6. All curves could be fitted with the same set of parameters: $\gamma = (2.0 \pm 0.2) \times 10^{-2}$ N/m, $K = (2.5 \pm 1.0) \times 10^{-11}$ N and $B = 1(-0.5, +10) \times 10^7$ N/m^2; the asymmetric error bars for B will be discussed in the next section. In fact, γ is known from the direct measurement of the surface tension in SmA membranes of the similar compound 7O.7 reported in ref. [4]. The elastic constants are compatible with previous results on SmA membranes of 7AB [30] and with values obtained with other techniques for various bulk SmA phases [76–80]. Using eq.4.16 the in-plane crossover from conformal to independent fluctuations can be calculated. From the above parameters we

69
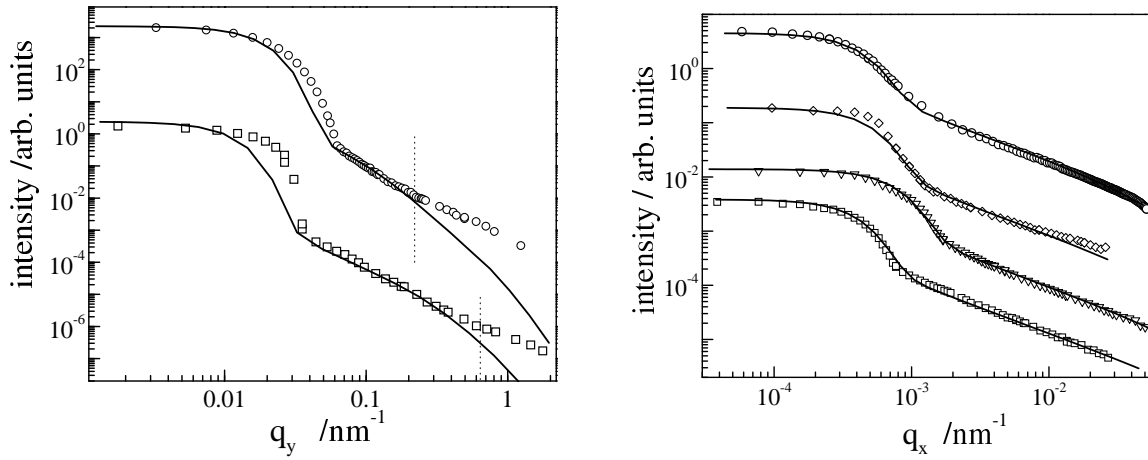
Figure 4.7: *SmA data from fig. 4.6 (open symbols) with corresponding intensity calculations (solid lines) as explained in sec. 4.3. The solid lines were obtained using the parameters reported in tab. 1.1 and varying only the number of layers and the resolution (see sec. 3.4). The dotted vertical lines indicate $2\pi/R_c$, i.e. the crossover from conformal to uncorrelated fluctuations.*

obtain $R_c \approx 31$ nm and $R_c \approx 9$ nm for the 80 and the 8-layer membrane, respectively. The values $2\pi/R_c$ are indicated by vertical dotted lines in fig. 4.7 (left). Agreement of the calculated curves with the experimental data is good for $q_\perp \lesssim 2\pi/R_c$, similarly as found in ref. [29].

The diffuse reflectivities in the CrB phase could be fitted with the same model parameters as used for SmA. Only for the 107-layer CrB membrane it was necessary to increase the surface tension from 0.020 to 0.035 N/m .

4.5 Discussion

4.5.1 Fluctuation profiles in smectic A membranes

In fig. 4.5 the fluctuation profiles of SmA membranes of various thickness as resulting from the analysis of the specular data have been shown. In fig. 4.8 the squared amplitude of the fluctuations in the center of each membrane (σ_{cent}^2) has been plotted as a function of $\ln N$. Neglecting in a first approximation the free surfaces, σ_{cent}^2 should diverge as in bulk SmA phases with $\ln N$, in which the slope depends only on the temperature and the product of the elastic constants
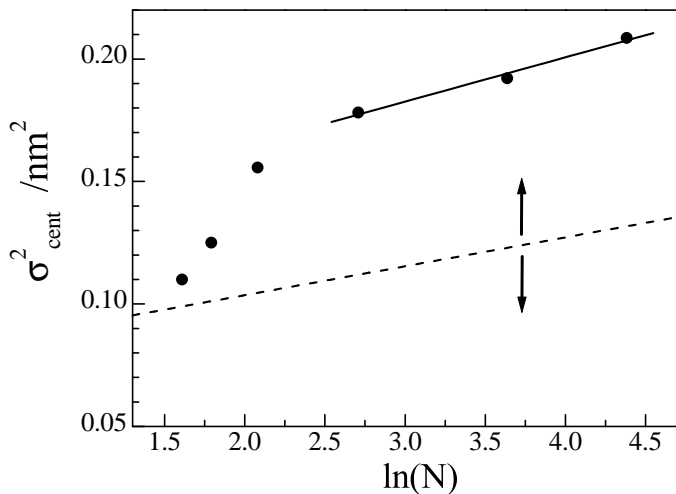
Figure 4.8: *Divergence of σ^2_{cent} as a function of $\ln N$ (Filled circles). The solid line is a linear fit to the data for the three thickest membranes. The dashed line gives the slope calculated for a bulk SmA phase with the Landau-de Gennes theory. The arrows indicate the large uncertainty in the absolute scale.*

(see eq.4.9). The data for the thinner membranes deviate significantly from this behavior. This is not unexpected since in thin membranes the surface tension strongly influences the fluctuations, which effect extends to the central layers. The data for the three thicker membranes do show a $\ln N$ dependence and can be fitted to a slope of $1.8 \cdot 10^{-2}$ nm^2. Inserting the elastic constants known from fitting the diffuse reflectivity data into eq.4.9 we obtain the 'bulk' slope $1.1 \cdot 10^{-2}$ nm^2. Evidently σ_{cent} as measured by x-ray reflectivity in (thin) SmA membranes diverges faster with the number of layers than expected for a bulk SmA phase. Even though the measured divergence is logarithmic for $N \gtrsim 15$, we have not reached the value corresponding to the Landau-Peierls instability. We conclude that, in the range of thickness investigated, the variation of σ_{cent} with increasing N is mainly determined by the decreasing influence of the surface damping. Measurements at much larger N are needed to check whether the variations of σ_{cent} approach the bulk slope.

Next we want to compare the absolute values of the fluctuation profiles with the predictions of the hydrodynamic theory. The hydrodynamic profiles can be calculated from eq.4.14 using the limit

$$\lim_{r_\perp \to \infty} g(r_\perp, z, z') = 2\sigma^2(z) \tag{4.28}$$

for $z = z'$. The integration in eq.4.14 has been performed first along q_z and then along $q_\perp$. For any finite sample the resulting value of $\sigma^2(z)$ diverges also with the in-plane cut-off Λ [68]. Hence, no direct quantitative comparison is possible with the theoretical predictions. In the literature, the value of Λ was fixed to $4\,\mu$m [27,68]. We chose instead $\Lambda = 50\,\mu$m, about equal to the projection of the transverse coherence length of the incoming x-ray beam on the membrane
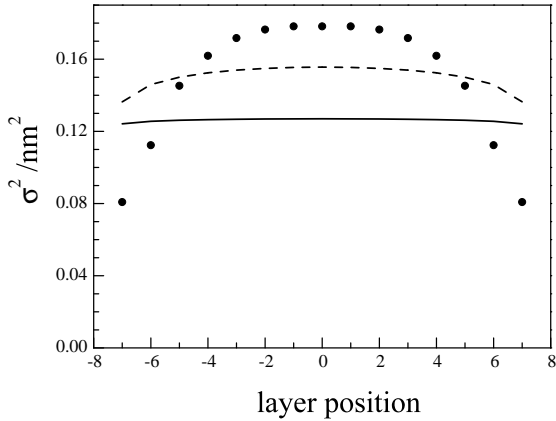
Figure 4.9: *Experimental fluctuation profiles of a 15-layer SmA membrane (filled circles) and theoretical calculations with eq.4.28 using the model parameters from tab.1.1, which lead to $\nu = 1.3$ (full line). The other theoretical curve is obtained for $\nu = 2.5$ (dashed line) as explained in the text.*

surface at an incoming angle corresponding to the first Bragg peak (see sec.2.5.1). In fig.4.9 the hydrodynamic profiles obtained from eq.4.28 are compared to the experimental data for the 15-layer SmA membrane. The model calculation (full line) predicts a much flatter profile than found experimentally. Such differences have been interpreted as due to the additional effect of a profile of the local disorder [30]. In addition to the hydrodynamic fluctuations also local fluctuations exist, leading to a distribution of the centers of mass of the molecules in the smectic layers (see ch.1). Assuming Gaussian distributions, these local fluctuations (σ_{loc}) can be added quadratically to the hydrodynamic ones (σ_{hyd}):

$$\sigma_{tot}^2 = \sigma_{loc}^2 + \sigma_{hyd}^2 \quad . \tag{4.29}$$

The total amplitude of the fluctuations is measured by specular reflectivity. Eq.4.29 has been used succesfully in ref. [27] for membranes of two different liquid crystal compounds. This required a measurement of σ_{loc} by fitting diffuse x-ray reflectivity scans at different q_z positions. In our case, no diffuse scattering data at different q_z values are available. Hence, there is no way to apply directly eq.4.29. However, our data show a similar curvature of the hydrodynamic profile as found in ref. [27] for SmA membranes of 7AB. This seems to confirm the existence of a pronounced profile of the local fluctuations is SmA membranes of 4O.8.

In the following we want to discuss the accuracy of the parameters obtained from the fitting of the diffuse reflectivity. The surface tension is known accurately from a direct measurements as $\gamma = (2.0 \pm 0.1) \times 10^{-2}$ N/m [4]. The accuracy for the two elastic constants can be estimated from fig.4.10, where the rocking scan measured for the 80-layer SmA membrane is shown together with model calculations. For B the error bars are asymmetric. The effect of reducing B half an order of magnitude is much more dramatic than augmenting it one order of magnitude. K
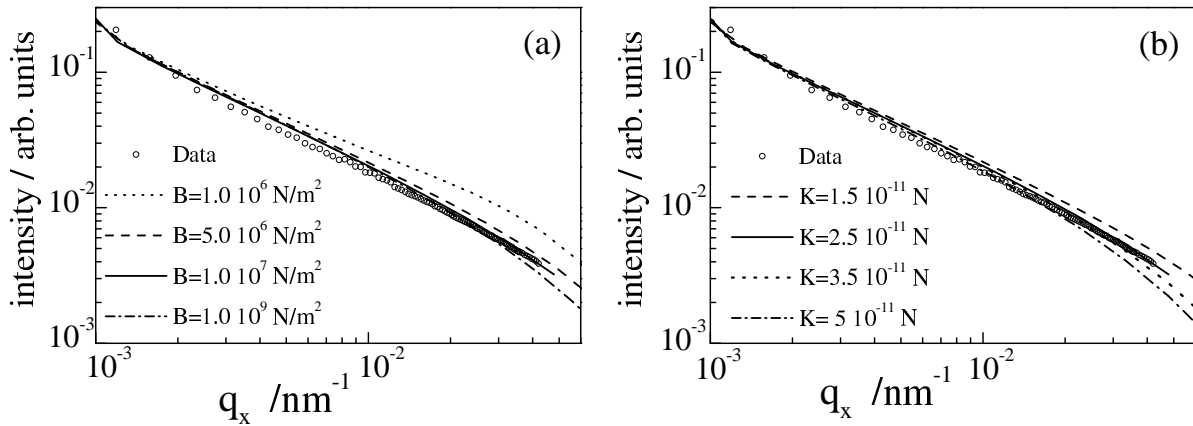
Figure 4.10: *Accuracy of the calculations with the Landau-de Gennes model for the rocking scan of the 80-layer membrane. The best fit is obtained for $B = 10^7 N/m^2$, $\gamma = 0.020$ N/m and $K= 2.5 \cdot 10^{-11}$ N (full line). The other curves differ only in the value of the elastic constant indicated.*

is determined by the curvature of the experimental data at higher q_x values. Small variations of K in both directions provoke significant changes in the calculated curve. The curvature of the hydrodynamic fluctuation profile depends on the value of $v = \gamma/\sqrt{BK}$. Using the smallest values of $\sqrt{BK}$ still compatible with the experiments (see fig. 4.10) a value of $v = 2.5$ is obtained. The resulting profile is displayed as the dashed line in fig. 4.9. Its curvature is still much lower than the experimental one. We conclude that the discrepancy between the fitting of the specular and the diffuse scans is outside of the error bars for the elastic parameters. This supports the earlier assumption of a considerable contribution from local fluctuations with a strong profile over the films.

Finally let us discuss the parameter $v = \gamma/\sqrt{BK}$ in some more detail. So far is has been used for $v > 1$ to describe the surface damping in a smectic membrane. In fact the situation is somewhat more complex. The hydrodynamic fluctuations of a bulk system are fully described by the Landau-de Gennes theory, and the resulting amplitude is determined by the value of $\sqrt{BK}$. 'Cutting' a smectic membrane out of the bulk by introducing two interfaces (for the moment without surface tension), the fluctuation amplitude would increase at the free surfaces because of the absence of an elastic response from the missing material at the outside. This effect will decay towards the center of the sample with a certain correlation length. Hence for membranes with a thickness less than twice this length, also the center of the film will be affected. Intro-
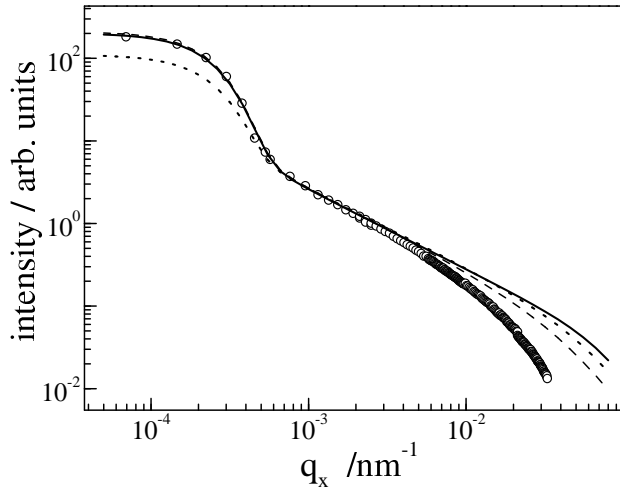
Figure 4.11: *Comparison between three theoretical calculations made with the Landau-de Gennes model for a 107-layer membrane and the experimental data relative to the CrB phase (open dots). The best fitting to the data (full line) is obtained for γ = 0.035 N/m, $B = 1.0 \cdot 10^7$ N/m^2 and $K = 2.5 \cdot 10^{-11}$ N. The dotted line is obtained for γ = 0.020 N/m. The dashed line was obtained for: $B = 10^9$ N/m^2, $K = 2.5 \cdot 10^{-11}$ N and γ = 0.035 N/m.*

ducing now a finite value of γ, the fluctuations at the free surfaces are suppressed with respect to the hypothetical situation with γ = 0. For $\gamma = \sqrt{BK}$ the surface tension exactly compensates for the 'missing material' and the hydrodynamic fluctuation profile is flat. Alternatively we find two other possibilities.

1. $\gamma > \sqrt{BK}$. In this situation the surface tension overcompensates the enhanced surface fluctuations due to missing material, leading to surface damping. As a result the fluctuation profile over a thin membrane will bend downwards at the edges. This case correspond to the case of 4O.8 treated above.

2. $\gamma < \sqrt{BK}$. In this case the fluctuations at the surface will still be enhanced compared to the bulk value. Now the fluctuation profile over a thin film will be concave. Upon increasing the thickness of the membrane, first the fluctuations in the center will decrease (diminishing influence of the surface enhancement), and subsequently increase once the Landau-Peierls effect takes over in thick films. The first part of this scenario has been observed experimentally for the compound FPP [29].

4.5.2 Thermal fluctuations in crystalline B membranes

From fig. 4.6 the spectral dependence of the correlation function in the CrB phase is very similar to that of the corresponding SmA membranes. The diffuse curves measured for CrB membranes can be fitted with almost the same parameters as used for the SmA membranes. Only for the
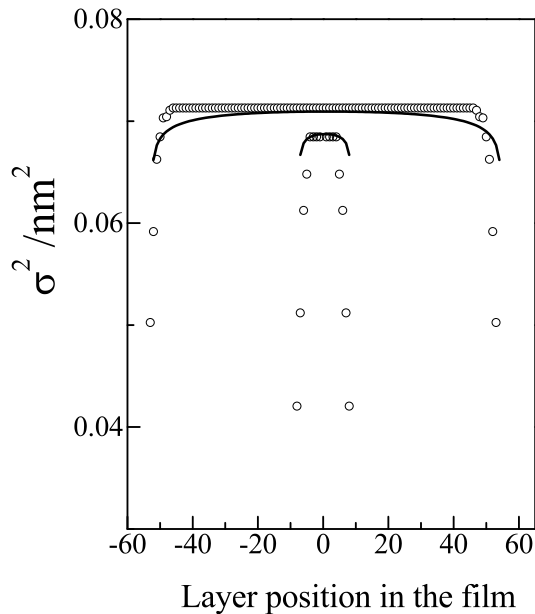
Figure 4.12: *Comparison of the experimental (specular) fluctuation profiles in the CrB phase (open dots) with theoretical calculations (lines) stemming from eq. 4.23 for the 107-layer and the 16-layer membranes. The theoretical profiles were obtained for: $B = 1.0 \cdot 10^7$ N/m^2, $K = 2.5 \cdot 10^{-11}$ N, $\gamma = 0.02$ N/m and $C_{44} = 1.0 \cdot 10^5$ N/m^2.*

thickest membrane (107 layers) the effect of the shear elastic constant C_{44} through a renormalization of γ (eq. 4.24) could be measured. For the 107-layer membrane we find $\gamma_{eff}/\gamma \approx 1.75$. This is about three times larger than the predicted renormalization effect. An independent measurement gives for 4O.8 in the CrB phase $\gamma = 0.027 \pm 2$ N/m [81] which is not far from the value of 0.035 ± 0.002 N/m resulting from fitting the diffuse scattering of the 107-layer CrB membrane. Nevertheless for this thick membrane the agreement with the experimental data becomes problematic at large q_x-values. This could be a general feature: at large q_x values and for membranes with $N \gtrsim 100$ the hydrodynamic theory seems not able to describe the experimental data, as found also in ref. [29] for SmA membranes. Fig. 4.11 shows also a calculation with an increased value of B, which does not help to describe the experimental data significatively better. In order to match the data, a large value of $K \approx 10^{-9}$ N has to be used. In principle such a large value for the bending elastic constant could stem from the positional order in the CrB phase. However, this value of K does not fit the diffuse reflectivity curves of thinner CrB membranes. Unfortunately we have no data for this 107-layer membrane in the SmA phase to compare, because the film thinned during heating.

The hamiltonian for the CrB phase (see sec. 4.2.3) differs from the hamiltonian for the SmA phase only because of an extra term proportional to $(\nabla_\perp u)^2$, which removes the Landau -Peierls instability. In fig. 4.12 we compare the predictions of the theory with the experimental fluctuation profiles from the specular reflectivity. The calculations reasonably reproduce the experi-

mental (flat) profiles, which are now hardly dependent on the number of layers. These results seem to indicate that CrB membranes fluctuate dynamically, rather similarly to SmA ones. Nevertheless the observed damping at the air interface is not fully described by this model. No satisfactory explanation appears at this point.

4.6   Conclusions

Specular and diffuse reflectivity curves have been measured for SmA and CrB membranes of thicknesses ranging from 3 to 107 layers. The thermal fluctuations in the center of the SmA membranes diverge faster than predicted from the Landau-Peierls instability for bulk systems, which is attributed to a strongly diminishing surface influence with increasing N. Our results seem to confirm that in SmA membranes the hydrodynamic contribution to the thermal fluctuations is not predominant, and a considerable contribution of local molecular disorder has to be assumed. The latter contribution should have a profile through the film.

The specular and the diffuse results for the CrB phase indicate that CrB membranes can be considered as dynamically fluctuating systems, rather similar to SmA ones. This conclusion is supported by the dynamic measurements to be discussed in chapter 6.

Chapter 5

Layer-by-layer surface crystallization

Upon decreasing temperature SmA membranes of 4O.8 transform to the CrB phase through successive layer-by-layer steps, starting from the most external layers. Specular x-ray reflectivity has been used to study the changes in the thermal fluctuation profile of an eight-layer membrane after each crystallization step. The crystallization is preceded by the formation of an intermediate layer structure with in-plane SmB ordering. We find an unusually large reduction of the fluctuations after the emergence of only the first SmB top-layer. The fluctuation profiles over the film are in all cases quenched at the surfaces though less so after each crystallization step. This behavior supports theoretical arguments that SmB ordering is reduced by out-of-plane smectic layer fluctuations.

5.1   Introduction

In liquid crystals a free surface usually stabilizes a higher ordered phase that is either observed in the bulk at lower temperatures or not observed in the bulk at all. Such surface induced *ordering* can be contrasted to surface melting which corresponds to surface *disorder* [14]. Outside the field of liquid crystals surface ordering has also been found in linear alkanes and alcohols [15–17]. Naively one would expect a free surface to be more disordered than the bulk material, due to the breaking of molecular binding at the interface ("missing neighbor" effect). However, microscopic interactions close to the surface may be quite different from those deep in the bulk. As a result, the surface may order before the bulk, or may even exhibit ordering phenomena of a different type than in the bulk material. Examples can be found in many liquid crystals. At

T=63.5 °C
SmA membrane

T=50.5 °C
Top layer CrB
Second top layer SmB
Inner layers SmA

T=58.5 °C
Top layer SmB
Inner layers SmA

T=50.2 °C
Two top layers CrB
Inner layers SmA

T=51.5 °C
Top layer CrB
Inner layers SmA

T=48 °C
CrB membrane
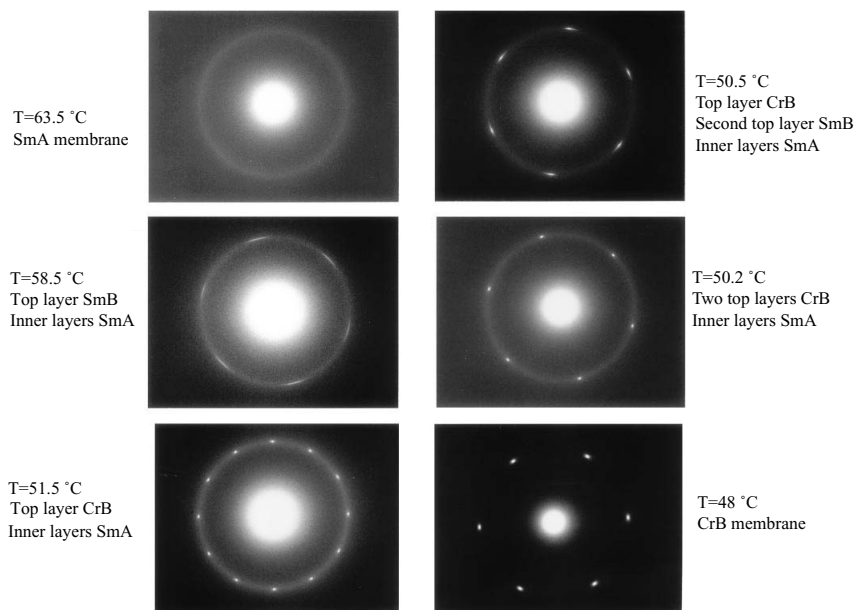
Figure 5.1: *Electron diffraction pattern of a 10-layer 4O.8 membrane (after ref. [24]).*

temperatures somewhat above a nematic-SmA transition usually smectic layers are formed at a free surface [18, 19]. Upon approaching in the isotropic phase the SmA phase from above, either a finite number of successive layering transitions is observed [20] or a continuous growth of the surface SmA phase occurs [21, 22]. In the case of a SmA-SmC transition a free surface usually induces a tilt, causing the SmC phase to grow continuously from the surface into the SmA interior of the film as the bulk transition temperature is approached from above [23].

The compound 4O.8 has long been considered as a prototypical liquid-crystal material which possesses a direct first-order transition from the SmA to the CrB phase [8, 82]. In bulk it undergoes the following phase transformations (in °C): Crystal 33 CrB 48.5 SmA 63.5 N 78 Isotropic. However, mechanical and heat capacity experiments on 4O.8 films have produced unexpected and at first controversial results. Early mechanical measurements with a low frequency torsional oscillator in contact with the film indicated two anomalies in the shear response: at the SmA-CrB bulk transition and about 6°C above this temperature [70, 83]. Later a whole cascade of phase transitions was detected via heat-capacity and optical reflectivity experiments [84], attributed to step-by-step surface crystallization. Subsequently transmission electron diffraction [24] provided evidence of a novel crystallization scenario: the SmA phase proceeds into the CrB phase in a layer-by-layer fashion involving an intermediate hexatic SmB phase, which

78

does not exist in the bulk.

SmA membranes of six layers or more show upon cooling the following typical sequence of diffraction patterns [24]: a diffuse ring, six diffuse arcs on top of a diffuse ring, two sets of sixfold spots on top of a diffuse ring, six spots and six diffuse arcs on top of a diffuse ring, again six spots on top of a diffuse ring, and finally six spots only (see fig. 5.1). These sequences can be interpreted as follows. Above $62°$C the film is in the SmA phase. At about $62°$C the surface layers undergo a transition to the SmB phase, while the interior layers remain in the SmA phase. Interestingly, the directions of the hexatic axes in the top layers at both sides of the film appear to be correlated, though there are liquid SmA layers in between them. At about $55°$C the top layers freeze into the CrB phase. The presence of two sets of six Bragg spots with equal intensity but arbitrary relative orientation, implies that any orientation of the crystalline axes in the top and bottom surface layers is not necessary fully correlated. At about $51°$C the second exterior layers transform into the SmB phase. The 12 diffraction spots have now collapsed into six, which suggests that the subtop SmB layers serve to lock-in the crystalline axes of the top and bottom surface layers. At $50.4°$C the second exterior layers also freeze into the CrB phase. This interpretation is confirmed by the fact that the integrated intensity of the diffraction spots now is about twice that of the crystalline pattern at $T > 51°$C [24]. Finally, after additional layer-by-layer transitions the entire film transforms into the CrB phase.

The above interpretation fits very well to other measurements in 4O.8 films. Firstly, at $T \approx 62°$C, the heat capacity shows a distinct phase transition, but the shear response is absent. Both these observations are consistent with a surface phase transition to an hexatic phase, which does not support a shear deformation. The divergent heat-capacity anomaly at the SmA-SmB transition in the surface layers is consistent with similar observations in other materials [85]. Secondly, at about $55°$C, mechanical measurements detected the onset of shear response of the film. This is consistent with the observation of a SmB-CrB transition in the surface layers. No detectable heat-capacity signal was observed at this transition [84]. The second anomaly observed in heat capacity at about $T = 51°$C corresponds to the SmA-SmB transition in the second exterior layers. Finally, below $49°$C the results are all consistent with the entire film freezing into the CrB phase.

In spite of the results described some important questions still remained open. (1) What is the mechanism driving the cascade of subsequent transitions? (2) How do the correlated directions between lattices in well-separated toplayers arise? These problems are of course related
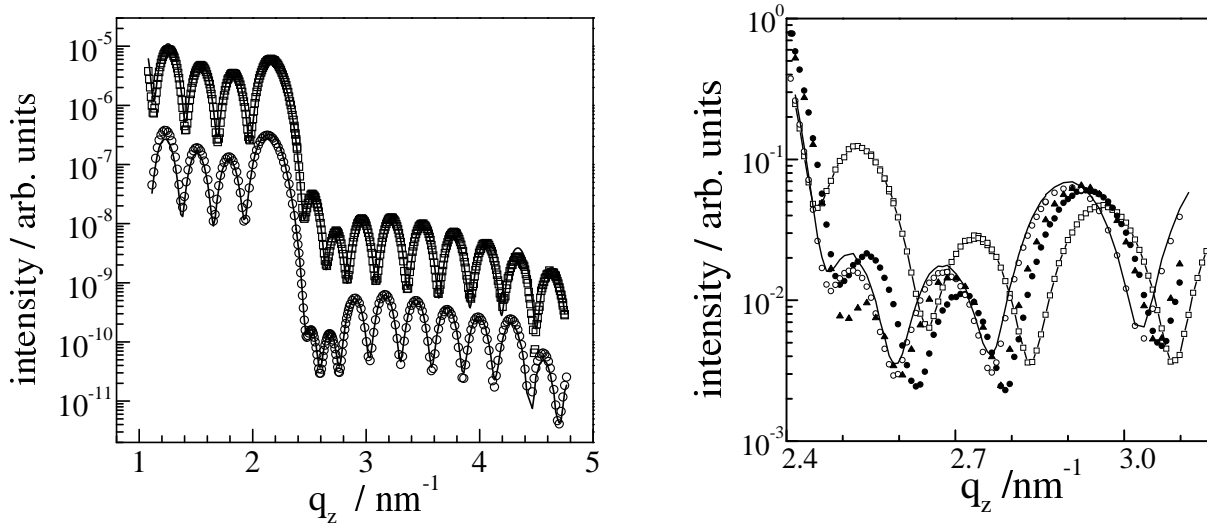
Figure 5.2: Left: *Specular x-ray reflectivity data of an 8-layer film in the SmA phase (62.5° C, upper curve) and in the CrB phase (47.0° C, lower curve). The curves have been shifted one decade for clarity. Solid line is a fit using the box model described in sec. 3.5.*

Right: *Blow up of the experimental curves in the q_z-region above the first Bragg peak: 62.5° C, SmA phase (squares); 52.5° C, one CrB top layer (filled circles); 50.3° C, two CrB top layers (triangles); 49.6° C, two SmA layers left in the middle (open circles); 47.0 °C, CrB phase (solid line).*

to the general interest whether these layer transitions are true examples of a Kosterlitz-Thouless process. In this chapter we provide at least a partial answer to these questions. Specular x-ray reflectivity was used to investigate in detail an 8-layer 4O.8 membrane upon cooling. This provided insight in the changes in the fluctuation profiles in dependence of the number of crystallized layers. The observed behavior supports theoretical arguments [86, 87] that the hexatic order is reduced by the out-of plane smectic layer fluctuations, which means in our situation enhanced at the surfaces compared to the interior of the film.

5.2   Fluctuation profiles upon surface crystallization

In this paragraph we present the results from a series of specular reflectivity scans performed on an 8-layer smectic membrane of 4O.8. From a comparison of the specular scans in the left part of fig. 5.2 it is clear that the intensity in the region just after the first Bragg peak is most sensitive to the development of the crystalline top layers. Hence changes in the shape of the electron density profile through the film are reflected by the deep minimum appearing at about

1	SmA 61.5 SmB 54.5 CrB
2	SmA 51.5 SmB 50.4 CrB
3	SmA 50.1 SmB 49.7 CrB
4	SmA 49.6 SmB 48.0 CrB
5	

Figure 5.3: *Phase transitions of each smectic layer for an 8-layer smectic membrane of 4O.8; the layer number is indicated at the left.*

$2.6 \, \text{nm}^{-1}$. On the right-hand side of fig.5.2 a blow-up of different specular reflectivity scans of this film at different temperatures is displayed. Starting from the SmA phase, the temperature was lowered at a controlled speed ($\sim 0.1°$C/min) while monitoring changes in the density profile of the film by means of fast specular scans around the first Bragg peak. The scans are different after each crystallization of an additional layer. Furthermore, preceding each transition of a SmA into a CrB layer, in the region between 2.5 and 2.7 nm^{-1} small but very reproducible changes in the intensity were detected, interpreted as the intermediary formation of an hexatic SmB phase [24, 88]. In the case of the first layer, such changes stopped about 3°C below the SmA-SmB transition temperature, until a sudden (bigger) jump in the curve was recorded, attributed to the SmB-CrB transition. The same behaviour was recorded upon crystallization of the second inner top layer. The equilibration time of each transition is of the order of seconds and no influence of the cooling speed has been detected. In this way the transition temperatures of the various layers could be determined with an accuracy of the order of 0.1°C. They are displayed in fig.5.3 and are in good agreement with literature indications [24].

The data have been fitted with an iterative matrix solution of the Fresnel equations for the reflectivity of the multilayer system using a slab-model for the electron density profiles, as described in sec.3.5. Each smectic layer has been approximated by the box-like function represented in Fig.3.13. Each data set was fitted independently keeping L_i and ρ_i fixed for the particular set. In contrast σ_i was left free for each smectic layer taking the centro-symmetry of the density profile into account. In the absence of reliable data around the critical angle no absolute values of ρ_1 and ρ_2 have been determined. Nevertheless, all calculations converged to
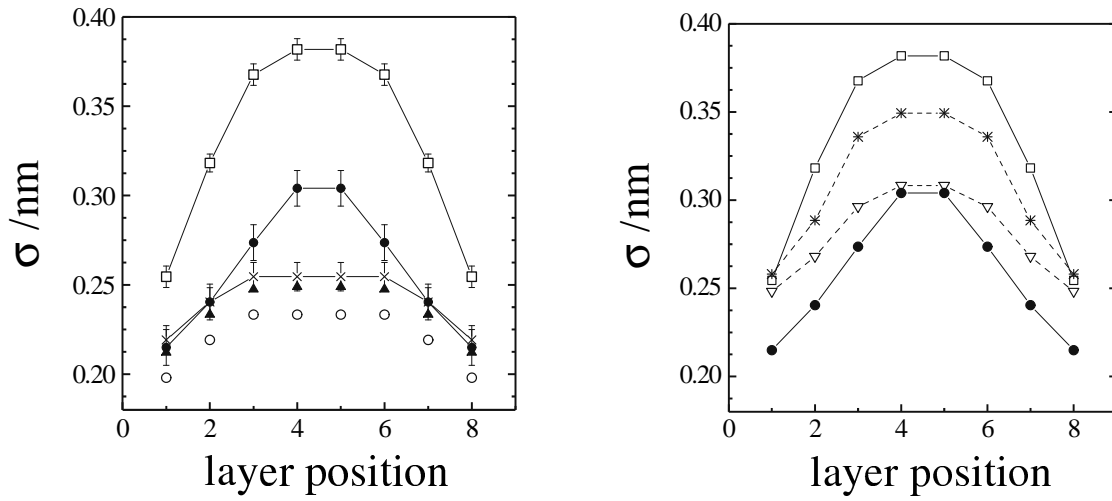
Figure 5.4: Left: *Fluctuation profiles of an 8-layer film: 62.5 °C, SmA phase, (squares); 52.5° C, one CrB top layer (filled circles); 50.3 °C, two CrB top layers (open circles); 49.65 °C, two SmA layers left in the middle (triangles); 47.0° C, CrB phase (crosses).*

Right: *Details of the top layer transitions: SmA phase at 62.5 °C (squares); hexatic SmB top layer at 60.7 °C (at high temperature in the hexatic range, asterisks) and at 55.7 °C (at low temperature in the hexatic range, inverted triangles); CrB top layer at 52.5 °C (filled circles).*

$\rho_2/\rho_1 \approx 1.5$ and $L_2/L_1 \approx 2.1$. The quality of the fitting of the experimental data is shown in fig. 5.2 for two typical curves. The resulting centro-symmetric σ_i profiles are depicted in fig. 5.4. Error bars indicate 95% confidence limits calculated taking the differences between the experimental and the calculated curves into account.

5.3 Discussion

Two effects can be distinguished when discussing surfaces of smectic membranes. The first one is purely geometrical and reflects the breaking of the translational and rotational invariance of the medium at an interface. As a consequence, near the surface the thermodynamic averages of local order parameters will be different from their bulk values. The second effect is the action of the surface field, which may lead to physical modifications of the system. The surface interactions can either suppress or enhance the bulk ordering. The fluctuation profiles over the 8-layer 4O.8 film are presented in fig. 5.4. In the SmA phase the fluctuations are quenched at the surface. Following the first SmA-SmB transition in the top layers, a considerable damping of the

layer displacement fluctuations occurs. Upon further cooling the amplitude of the fluctuations of the interior layers continue to decrease within the temperature range of the hexatic SmB top layers. This behavior suggests that the second stage of the crystallization process (SmB-CrB) evolves by a continuous increase of the in-plane positional order in the hexatic top layers, which in turn provide more rigid boundary conditions for the fluctuations of the film. Once the SmB-CrB transition in the top layers is established, appreciable damping occurs also in the exterior layers of the membrane. The new profile provides the basis for the second series of crystallization transitions in the next-nearest top layers. Once two layers are crystallized at each side, the fluctuations of the remaining four SmA layers are such that the total profile over the film is much flatter. In agreement with this behavior the differences in transition temperatures between the *new* SmA surface layers and those in the center of the film approach each other rapidly (see fig. 5.3). In this picture the cascade of successive SmA-SmB-CrB phase transitions is triggered off by the changing fluctuation profile in the successive layers.

This fluctuation scenario also helps to understand another phenomenon. Electron diffraction of 4O.8 films indicate a coupling of the bond-order directions of the top and bottom layers [24]. This is rather counterintuitive as the intermediate SmA layers still have a liquid in-plane structure. However, earlier x-ray reflectivity studies of smectic films [29, 30] indicate that the hydrodynamic fluctuations in thin SmA membranes are fully conformal. As a consequence any directional interaction between the fluctuation amplitude and the local hexatic lattice [68] will be the same at both sides of the film. Hence conformal fluctuations provide a natural mechanism to correlate lattice directions in top and bottom surface hexatic layers.

The melting scenario in 4O.8 films is unique in the sense that the two-stage melting process occurs successively in one smectic layer after another. Such a melting behavior implies that the interaction between neighboring layers is very small. In the limit of a two-layer 4O.8 film, the whole film attains hexatic order and the SmB phase is stabilized in a temperature range of about 5°C between the SmA and CrB phases [88]. Evidently the hexatic phase is an important component of the melting process in smectic membranes and the results support the two-stage melting scenario predicted by defect-mediated melting theory in two dimensions.

Besides the two-layer 4O.8 film mentioned, also the surface top layers in thicker films may serve as a model system to study the liquid-hexatic-crystal sequence in two dimensions. Though electron diffraction has provided confidence in the structure of the surface induced phases, due to its relatively low resolution little can be said about the development of the positional order in

the successive layers. Grazing incidence X-ray diffraction fills this gap and provides insight via the in-plane scattering profiles during the liquid-hexatic-crystal sequence in the top layers of the film [89]. The results show that the liquid-hexatic transition in the top layers is continuous (within the experimental temperature resolution). This is in agreement with the heat capacity measurement of ref. [85]. Secondly a saturation of the positional correlation length in the surface hexatic layer about has been observed $3°$C below the SmA-SmB transition temperature. This observation correlates well with the observed evolution of the fluctuation profile preceding the outer layer SmB-CrB transition reported in fig.5.4.

To finish this section we want to emphasize that the physical origin of enhanced surface order in smectic membranes is not fully clear yet. Since many phases of different structures can be stabilized at the free surface, the microscopic details of surface interactions appear to be less important. What is common to the tilted SmC phase (with liquid in-plane order) and the orthogonal hexatic SmB phase, that both can be stabilized on a free SmA surface in dependence of the liquid crystal under consideration? A possible explanation might be in the quenching of the layer displacement fluctuations at the SmA surface, which according to theoretical arguments [86, 87], enhances hexatic order. The first stage of a Kosterlitz-Thouless mechanism upon the SmA-SmB transition is driven by the unbinding of disclination pairs. Smectic layer fluctuations are coupled to the hexatic order because of a frustration in the bond-angle field due to the curvature of the smectic layers. As a general result the layer fluctuations decrease the disclination core energy and thus the SmA-SmB transition temperature. Hence if the layer fluctuations in the SmA phase are quenched at the surface (as shown in fig.5.4) the liquid-hexatic transition temperature is correspondingly larger at the surface than in the bulk. We note that in some compounds also the situation $\nu < 1$ has been observed [29, 90]. It would be interesting to investigate whether the associated enhanced surface fluctuations lead indeed to conventional surface melting in these cases [91]. This argument applies equally well to the tilted smectic phases possessing some degree of bond-orientational order as to the orthogonal hexatic SmB phase discussed here. X-ray reflectivity can be the tool to obtain information on the fluctuation profiles, and could be used more systematically.

5.4 Conclusions

Specular x-ray reflectivity has been used to characterize the thermal fluctuation behavior upon layer-by-layer crystallization in 8-layer smectic membranes of 4O.8. The fluctuation profile in the initial SmA film is quenched at the surfaces, supporting theoretical predictions that correlate the onset of hexatic order with decreased layer fluctuations. As the fluctuations can be expected to be fully conformal throughout the film, this process also explains the reported correlation of the crystallographic directions in the top and bottom surface layers. The changing fluctuation behavior in the successive layers triggers off a cascade of successive SmA-SmB-CrB phase transitions per layer.

Chapter 6

Dynamics of fluctuations in smectic A and crystalline B membranes

6.1 Introduction

As discussed in sec. 2.5.3 if coherent radiation is incident on a material, the scattered intensity shows a speckle pattern that reflects the instantaneous configuration of the scatterers. Movement of the scatterers causes a corresponding change in this pattern and thus contains information on the dynamics of the system. Photon correlation spectroscopy or dynamic light scattering measures the time dependent intensity autocorrelation function of the speckle pattern. Using visible light it has developed into a well-established technique since lasers became available. In contrast, correlation spectroscopy with coherent x-rays has only become possible recently at third generation high-brilliance synchrotron sources. A considerable advantage of x-rays is that they do not suffer from multiple scattering problems, so that also opaque systems can be studied. In the context of smectic membranes other differences between the two methods are important. Light-scattering experiments are sensitive either to orientational fluctuations of molecules associated with layer undulations [67, 92] or to fluctuations of the air-liquid interface (as in the case of [93]), but not to the undulations themselves. They also do not probe distances of the order of the layer spacing. In contrast, x-ray scattering or x-ray photon correlation spectroscopy (XPCS) is sensitive to the layer undulations and gives a much better spatial resolution. Most importantly in smectic membranes, the finite size leads to quantization of the fluctuations, producing a set of modes instead of the continuous spectrum expected in bulk systems. In addition surface effects
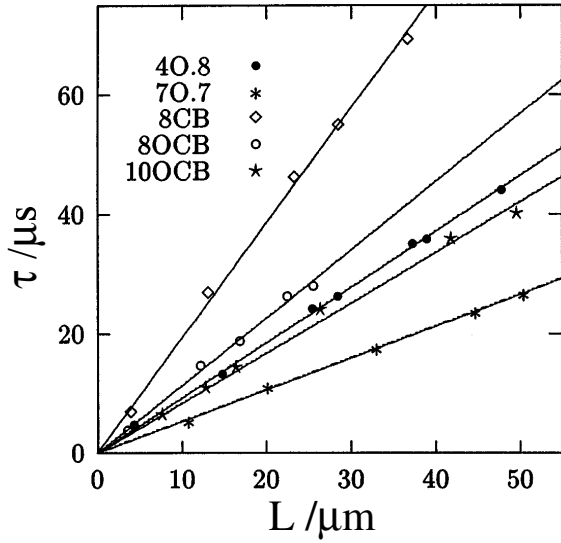
Figure 6.1: *Plot of τ versus film thickness for various liquid crystals. The straight lines are fits to eq. 6.7. (After ref. [6])*

require that one takes the surface tension and perhaps other surface parameters into account.

With respect to smectic membranes there has been recently quite some theoretical interest in the dynamics of the layer fluctuations [6, 40, 94–97]. Experimentally XPCS in the soft x-ray region has recently been applied to $5-50$ μm thick smectic membranes of various compounds (including 4O.8) by Sorensen and coworkers [6]. An exponential decay of the correlation function was found with a relaxation time τ. As shown in fig. 6.1, decay times typically in the range of tens of μs scale linearly with the film thickness (tens of μm). Here we report on our XPCS work using standard ($\sim$ 8 keV) x-rays of thin smectic films. As we shall see in sec. 6.3 we observe in contrast to fig. 6.1 an "oscillatory" behavior of the correlation function, which cannot be described by a simple exponential time-dependence. In the following section we shall first set a framework by summarizing the theoretical predictions for the various modes. In sec. 6.3 and sec. 6.4 follow the experimental results and a discussion, including both smectic A and crystalline B membranes.

6.2 Dynamics of fluctuations, theory

Starting point to discuss the dynamics of fluctuations in smectic membranes is the continuous version of the theory by Shalaginov et al. [40]. The intensity $S(\mathbf{q})$ given by eq. 2.29 depends on the correlation function $g_{mn}(\mathbf{r}_\perp)$, which now has to be generalized to include the time-

88

dependence to

$$g_{mn}(\mathbf{r}_\perp,t) = \langle [u_m(0,0) - u_n(\mathbf{r}_\perp,t)]^2 \rangle. \tag{6.1}$$

To study $g_{mn}(\mathbf{r}_\perp,t)$ the hydrodynamic equations for bulk smectic-A are used to calculate

$$g(\mathbf{r}_\perp,z,z',t) = \langle [u(0,z',0) - u(\mathbf{r}_\perp,z,t)]^2 \rangle, \tag{6.2}$$

where z remains a continuous variable. To calculate the scattering $g_{mn}(\mathbf{r}_\perp,t)$ is set to $g(\mathbf{r}_\perp,z_n,z_m,t)$ where z_m and z_n are the z-coordinates of smectic layers m and n, respectively. To simplify the hydrodynamic equations for a smectic-A liquid crystals first the permeation process is neglected. Secondly two characteristic times are distinguished. The first one is the time required for viscous forces to respond to inertia (*fast mode*). The second time scale comes from the balance between viscous and elastic forces (*slow mode*). Due to the smallness of the parameter $\rho_0 K/\eta_3^2 \lesssim 10^{-6}$ [2], the ratio of inertia to elastic forces, one can consider the slow and fast modes separately in a bulk smectic liquid crystal. Equations for the slow mode are usually obtained from the general hydrodynamic equations by neglecting inertial terms.

6.2.1 Smectic A membranes

The calculation of the relaxation times is based on the solution of the equation of motion which reads:

$$\rho_0 \frac{\partial^2 u(\mathbf{r},t)}{\partial t^2} = \left[\eta_3 \frac{\partial}{\partial t}\Delta_\perp + B\nabla_z^2 - K\Delta_\perp^2 \right] u(\mathbf{r},t). \tag{6.3}$$

in which η_3 is the layer shear viscosity coefficient. The boundary conditions for the surface tension γ at $z = \pm L/2$ are the same as used for the static case. This implicitly assumes that relaxation at the interfaces is much faster than in the bulk (i.e., the viscosity at the interfaces is negligible) and represent the balance of elastic forces at the interfaces.

For the calculation of the correlation function $g_{mn}(\mathbf{r}_\perp,t)$ we refer to the original paper [40]. In case of an infinite system one would obtain a continuous spectrum, with relaxation times $\tau(q_z)$ being continuous functions of wave number q_z in the z-direction. The finiteness of the system in the z-direction leads to quantization and as a result produces a discrete spectrum. The full results for the characteristic times of the system are the roots of the equation [40]:

$$\rho_0 \frac{1}{\tau^2} - \eta_3 q_\perp^2 \frac{1}{\tau} + Kq_\perp^4 + \frac{\gamma^2 q_\perp^4}{B} Z_m^2 = 0. \tag{6.4}$$
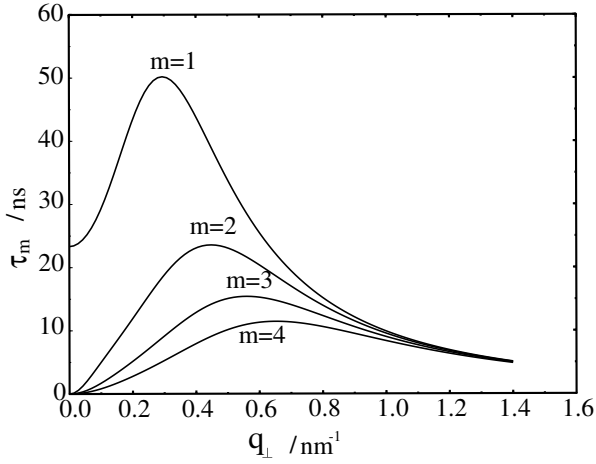
Figure 6.2: *Relaxation times τ_m, $m = 1, 2, 3, 4$ vs the in-plane wave vector transfer for a 5-layer film, calculated with the parameters: $d = 2.8$ nm, $K = 10^{-11}$ N, $B = 2.5 \times 10^6$ N/m², $\gamma = 3 \times 10^{-2}$ N/m, $\eta_3 = 0.1$ kg/(m·s).*

in which the Z_m are the roots of:

$$\tan(wZ) = \frac{2Z}{Z^2 - 1}, \qquad \text{with} \qquad w = \frac{\gamma q_\perp^2 L}{B}. \tag{6.5}$$

Hence for each Z_m we have two characteristic times, of which the larger one corresponds to the slow mode. Neglecting inertia and for small $q_\perp$, the lowest order relaxation time ($m = 1$) can be approximated by [40]:

$$\tau_1 \approx \eta_3 \left[\frac{2\gamma}{L} + \left(1 - \frac{\gamma^2}{3KB} \right) K q_\perp^2 \right]^{-1}. \tag{6.6}$$

This expression is valid only for $q_\perp^2 \ll B/\gamma L$. For $q_\perp = 0$ it agrees with the result of Poniewierski et al. [94]:

$$\tau_1 = \frac{\eta_3 L}{2\gamma}. \tag{6.7}$$

Note that, according to eq. 6.6 in this range of $q_\perp$, τ_1 decreases with $q_\perp$ if $\gamma^2 < 3KB$ and increases if $\gamma^2 > 3KB$. A more detailed consideration shows that for $q_\perp = 0$ only the first relaxation time is non-zero, while all the others vanish in the no-inertia approximation. Fig. 6.2 shows the first few characteristic times versus $q_\perp$.

In the long wavelength limit $\rho_0 K / \eta_3^2$ is not small anymore. The inertia term has to taken into account due to the increasing importance of the surface term. For $m = 1$ and small $q_\perp$ this yields approximately [40]:

$$\frac{1}{\tau_1} \approx \mp \iota \frac{1}{2} \sqrt{\frac{8\gamma}{\rho_0 L}} q_\perp + \frac{\eta_3}{2\rho_0} q_\perp^2. \tag{6.8}$$

The complex behaviour predicted by this equation is illustrated in fig. 6.3. Note that for $q_\perp = 0$ now the relaxation time is not finite anymore.
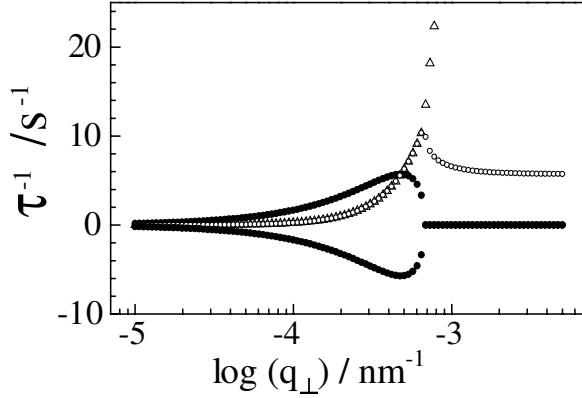
Figure 6.3: *Complex behavior of the first fundamental relaxation mode for an incompressible 50-layer SmA membrane, calculated with* $\gamma = 0.021$ *N/m,* $K = 5 \times 10^{-12}$ *N,* $\eta_3 = 0.05$ *kg/(m·s),* $\rho_0 = 10^3$ *kg/m^3. The triangles and circles show the real part of the relaxation of the fast and the slow branch, respectively; the dots show the imaginary part of the first relaxation time of both branches.*

6.2.2 Crystalline B membranes

In ch.4 it has been shown that the diffuse scattering remains very similar when a SmA film is cooled and becomes a CrB plate. Hence it is of interest to apply the continuous dynamic model to the CrB phase. Again we refer for details to [40]. Here we approximate the results by following the final result of sec.4.2.3 that, in the easy-shear approximation, the main effect of the CrB phase via C_{44} can be incorporated by replacing the surface tension γ by $\gamma_{eff} = \gamma + L\, C_{44}/8$. Making this replacement in eq.6.7 the characteristic time provided by the balance of viscous and elastic forces (no inertia approximation) is for $q_\perp = 0$:

$$\tau_1 = \frac{\eta_3}{2\gamma/L + C_{44}/4} \quad . \tag{6.9}$$

Note that for small values of L the effect of C_{44} can be neglected. Thin CrB membranes behave in the easy-shear approximation exactly as SmA membranes: the correction becomes only appreciable for rather thick films. However, note that γ itself might also increase upon going from SmA to CrB [5].

As already noted for SmA membranes at long wavelength the parameter $\rho_0 K/\eta_3^2$, the ratio of inertia to the elastic force, is not small anymore. This effect is even stronger for CrB membranes where this condition changes to

$$\frac{\rho_0 C_{44}^2}{16 K \eta_3^2 q_\perp^4} \ll 1. \tag{6.10}$$

Taking $C_{44} = 10^5$N/m^2, $K = 10^{-11}$N, $\eta_3 = 10^{-1}$kg/(m·s), $\rho_0 = 10^3$kg/m^3, eq.6.10 gives $q_\perp \gg 1.6 \times 10^{-3}$ nm^{-1}. Hence, for smaller $q_\perp$ one has to keep the inertial term in the dynamical equation, which means that the slow and fast modes again cannot be considered separately.
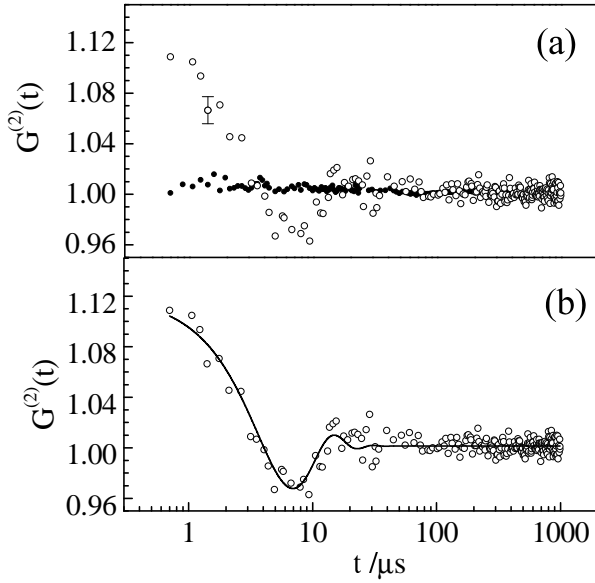
Figure 6.4: *Autocorrelation function at $q_z = 2.2$ nm^{-1} for a 95-layer membrane (thickness 0.27 μm) in the SmA phase at 50.1 °C.*
(a) Raw data (open circles) and reference signal from a NiC multilayer (filled circles).
(b) Normalized correlation function obtained by dividing the raw data by the NiC reference signal; solid line is a fit to eq. 6.12.

Similar to eq. 6.8 one now finds [40]:

$$\frac{1}{\tau_1} \approx \mp \iota \frac{1}{2} \sqrt{\frac{LC_{44} + 8\gamma}{\rho_0 L}} q_\perp + \frac{\eta_3}{2\rho_0} q_\perp^2 \; . \tag{6.11}$$

Thus the resulting curves for the real and and imaginary parts are for thin films and small $q_\perp$ very similar to those predicted by eq. 6.8. In contrast to the no-inertia analysis, the relaxation times do not remain finite as $q_\perp$ vanishes, but diverge to infinity (see also [95, 96]).

6.3 Experimental results

XPCS experiments have been performed at beamline ID10A of the ESRF as described in sec. 3.2.3. Smectic membranes of 4O.8 were investigated both in the SmA phase at 50.1 °C and in the CrB phase at 46.0 °C. Fig. 6.4a displays the intensity-intensity autocorrelation function $G^{(2)}(t)$ in the SmA phase and a reference correlation function; fig. 6.4b gives the resulting normalized correlation function. The error bar is calculated from eq. 3.2. The normalized correlation function shows a decay of the layer fluctuations in the time scale of microseconds and oscillatory behavior in the range of tens of microseconds. The results were fitted to the simplest form of an oscillating exponential decay:

$$G^{(2)}(t) = 1 + A \cos(\omega t) \exp(-t/\tau) \; , \tag{6.12}$$
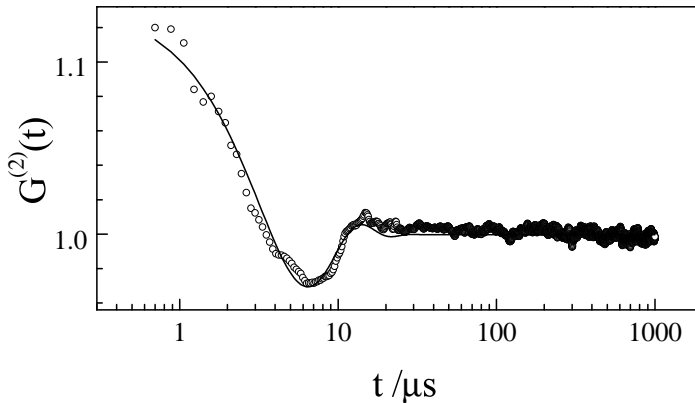
Figure 6.5: *Normalized intensity-intensity autocorrelation function at $q_z = 2.2$ nm^{-1} of a 0.27 μm thick membrane in the CrB phase (T= 46°C).*

where the amplitude A is determined by the degree of coherence. The result gives $A = 0.120 \pm 0.005$, $\tau = 5.8 \pm 0.5$ μs and $2\pi/\omega = 15.9 \pm 0.3$ μs. Similar values were obtained at other temperatures in the SmA phase.

The dynamic nature of the fluctuations in CrB membranes is explicitly demonstrated by the results in fig.6.5 for $G^{(2)}(t)$ in the CrB phase normalized in the same way as before. The displayed correlation function has been normalized as described for the SmA case. The behavior of the correlation function is very similar to in fig.6.4 for SmA membranes. It can again be described by an exponential decay of which the amplitude is modulated by a cosine function. The associated relaxation time is $\tau = 4.9 \pm 0.5$ μs while the oscillatory behavior has a period given by $2\pi/\omega = 15.1 \pm 0.3$ μs. In fact these times hardly change upon heating into the SmA phase.

6.4 Discussion

The results can be understood within the theoretical framework summarized in sec.6.2. First we note that the proportionality between τ_1 and L given by eq.6.7 has been confirmed for thick films by Price et al. as shown in fig.6.1. However, our own results on a thin 4O.8 membrane show a very different behaviour. This can be attributed to the influence of the inertia term that cannot be disregarded anymore. For bulk systems the parameter $\rho_0 K / \eta_3^2$ is small (about 10^{-4} to 10^{-6}) due to the absence of a term proportional to $q_\perp^2$ in the free energy. For thin membranes this situation changes because of the additional surface contribution $\gamma q_\perp^2$. For conformal fluctuations in the long wavelength limit ($q_\perp^2 \to 0$) the latter term prevails over the bending term $K q_\perp^4$ and the inertial term becomes important. Taking values typical for 4O.8: $\gamma = 0.021$ N/m, $\eta_3 = 0.04$
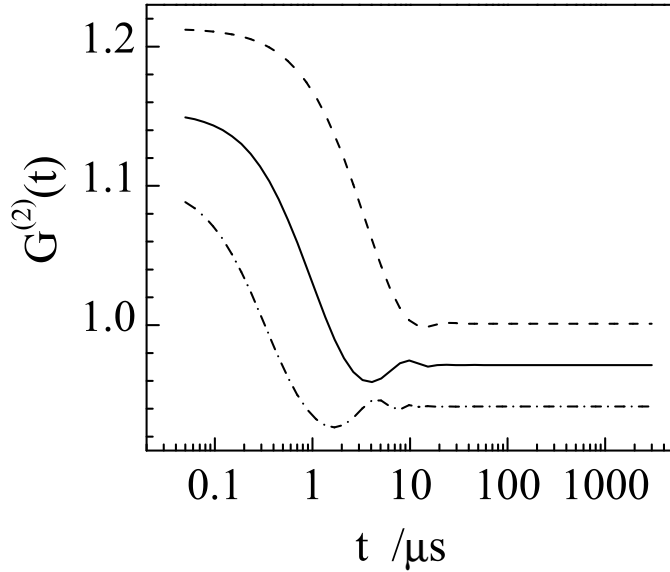
Figure 6.6: *Calculation of the experimental correlation function $G^{(2)}(t)$ with parameters as in fig.6.3 for various film thickness: N= 1000 (dashed line), N=200 (full line), and N=50 (dash-dot-dash line) [40]. The last two curves have been moved down by 0.03 for clarity.*

kg/(m·s), $\rho_0 = 10^3$ kg/m^3 we arrive at a marginal value $q_{\perp,c} \approx 2 \times 10^{-3}$ nm^{-1}. Theoretical results for finite size SmA films calculated taking inertia into account using eq.6.8 have been displayed in fig.6.3 The relaxation time appears to be complex for $q_\perp < q_{\perp,c}$: the real part leads to relaxation while the imaginary part produces oscillations in the correlation function. As our instrumental resolution is of the same order of magnitude as $q_{\perp,c}$, oscillations in $G^{(2)}(t)$ should be observable for sufficiently thin films, in agreement with fig.6.4.

In order to make the complex behavior of the smectic layer relaxation more clear we calculated the time-dependent part of the intensity-intensity correlation function $G^{(2)}(t)$ by convoluting the theoretical correlation function with the experimental resolution. Fig.6.6 shows the results for SmA membranes of different thickness. The oscillatory behavior of non-overdamped layer fluctuations for $q_\perp < q_{\perp,c}$ is well reproduced for thin films. The oscillations become less pronounced with increasing membrane thickness and finally completely disappear for 1000 layers (thickness about 3 μm). The resulting values of τ and $2\pi/\omega$ are of the right order of magnitude; they differ a factor 2 to 3 from the experimental ones. The theoretical results depend strongly on the long wavelength cut-off used. A value of 100 μm has been chosen, which is about the effective (projected) speckle size at the Bragg position. The prediction of disappearing oscillations for thick films is in agreement with the simple exponential decay reported for films between 5 and 50 μm in [6]. Since the completion of this work further XPCS measurements have been done on 4O.8 membranes of various thickness and high-quality uniformity [98]. Fig. 6.7 shows these high-contrast results, which in principle indeed confirm the transition from fig.
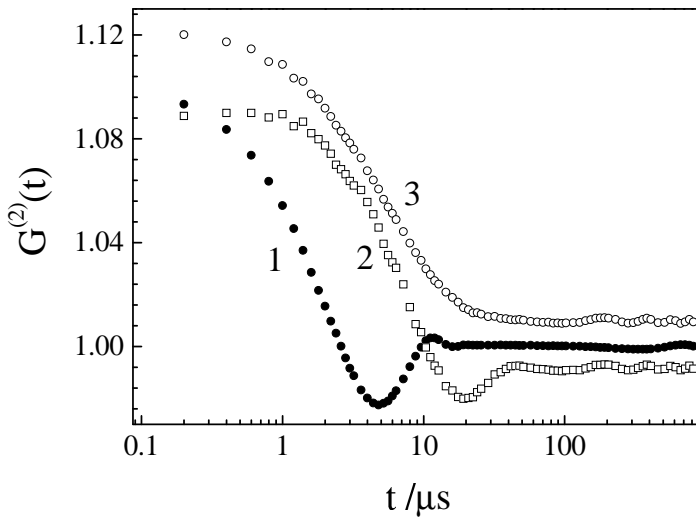
Figure 6.7: *Autocorrelation function of 4O.8 membranes of different thickness measured at $q_z = 2.2$ nm^{-1}: 0.3 μm (filled circles), 4.0 μm (squares) and 7.0 μm (open circles). Curves 2 and 3 are shifted by ± 0.01 for clarity.*

6.6.

In sec.4.5.2 the diffuse reflectivities of SmA and CrB membranes have been compared. The difference between the SmA and CrB results could be accounted for by an increase of the effective surface tension $\gamma_{eff} = \gamma + LC_{44}/8$ from 0.02 to about 0.03 N/m. Using $\gamma = 0.02$ N/m [4] and $C_{44} = 0.10 \times 10^6$ N/m^2 [5] we calculate that the correction becomes appreciable for rather thick films and that the term $LC_{44}/8$ is equal to γ for about 450 layers. However, γ itself might also increase upon going from SmA to CrB. The observed increase in γ_{eff} does not allow one to discriminate between these two possible contributions.

The dynamic nature of the fluctuations in CrB films has been explicitly demonstrated by a measurement of the intensity-intensity autocorrelation function, see fig.6.5. The oscillatory behavior of the correlation function is very similar to that reported for SmA films and the associated times hardly change upon heating into the SmA phase. This is in agreement with eq.6.9, which has been derived by again replacing γ by γ_{eff}. Hence the fluctuations in CrB films can be described essentially by the same hydrodynamic model as used for SmA membranes.

6.5 Conclusions

X-ray photon correlation spectroscopy has been used to characterize thermal fluctuations in smectic A membranes. We have demonstrated the feasibility of XPCS experiments with standard 8 keV x-rays on thin films leading to relaxation times in the microsecond range. For such thin SmA membranes we resolved both an oscillatory and a damping behavior of the intensity-

intensity correlation function. In agreement with recent theory this indicates that the inertial term in the dynamic equations cannot be disregarded anymore in thin films for which the surface contribution becomes important. In addition the dynamic nature of the CrB fluctuations has been confirmed by XPCS.

Bibliography

[1] G. Vertogen and W. H. de Jeu, *Thermotropic Liquid Crystals - Fundamentals*, Springer Verlag, Berlin, 1985.

[2] P. G. de Gennes and J. Prost, *The Physics of Liquid Crystals*, Clarendon Press, Oxford, 1993.

[3] P. M. Chaikin and T. C. Lubensky, *Principles of Condensed Matter Physics*, Cambridge University Press, Cambridge, 1995.

[4] P. Mach et al., Langmuir **14**, 4330 (1998).

[5] M. Cagnon and G. Durand, Phys. Rev. Lett. **45**, 1418 (1980).

[6] A. C. Price, L. B. Sorensen, S. D. Kevan, J. Toner, A. Poniewierski, and R. Holyst, Phys. Rev. Lett. **82**, 755 (1999).

[7] A.J. Leadbetter, J.C. Frost, and M.A. Mazid, Journ. Phys. (France) Lett. **40**, 325 (1979).

[8] D. E. Moncton and R. Pindak, Phys. Rev. Lett. **43**, 701 (1979).

[9] A. J. Leadbetter, *The molecular Physics of Liquid Crystals*, chapter 13, p. 284, Academic Press, London, 1979, Edited by G. R. Luckhurst and G. W. Gray.

[10] W. L. McMillan, Phys. Rev. A **6**, 936 (1972).

[11] M. Born and E. Wolf, *Principles of Optics*, Pergamon Press, Bath, second edition edition, 1964.

[12] J. Als-Nielsen, J. D. Litster, R. J. Birgeneau, M. Kaplan, C. R. Safinya, A. Lindegaard-Andersen, and S. Mathiesen, Phys. Rev. B **22**, 312 (1980).

[13] C. R. Safinya, D. Roux, G. S. Smith, S. K. Sinha, P. Dimon, N. A. Clark, and A. M. Belloq, Phys. Rev. Lett. **57**, 2718 (1986).

Bibliography

[14] H. Dosch, *Critical Phenomena at Surfaces and Interfaces*, volume 126 of *Springer Tracts in Modern Physics*, Springer, Berlin, 1992, Chapter 5.2.

[15] B. M. Ocko, X. Z. Wu, E. B. Sirota, S. K. Sinha, O. Gang, and M. Deutsch, Phys. Rev. E **55**, 3164 (1997).

[16] B. M. Ocko, E. B. Sirota, M. Deutsch E. di Masi, S. Coburn, J. Strzalka, Songyan Zheng, Andrey Tronin, Thomas Gog, and Chitra Venkataraman, Phys. Rev. E **63**, 32602 (2001).

[17] O. Gang, B. M. Ocko, X. Z. Wu, E. B. Sirota, and M. Deutsch, Phys. Rev. Lett. **80**, 1265 (1998).

[18] J. Als-Nielsen, F. Christensen, and P. S. Pershan, Phys. Rev. Lett. **48**, 1107 (1982).

[19] P.S. Pershan, A. Braslau, A.H. Weiss, and J. Als-Nielsen, Phys. Rev. A **35**, 4800 (1987).

[20] B.M. Ocko, A. Braslau, P. S. Pershan, J. Als-Nielsen, and M. Deutsch, Phys. Rev. Lett. **57**, 94 (1986).

[21] P. Lucht and Ch. Bahr, Phys. Rev. Lett. **78**, 3487 (1997).

[22] P. Lucht, P. Marczuk, Ch. Bahr, and G.H. Findenegg, Phys. Rev. E **63**, 041704 (2001).

[23] Ch. Bahr, C.J. Booth, D. Fliegner, and J.W. Goodby, Phys. Rev. Lett. **77**, 1083 (1977).

[24] C. Y. Chao, C. F. Chou, J. T. Ho, S. W. Hui, A. Jip, and C. C. Huang, Phys. Rev. Lett. **77**, 2750 (1996).

[25] A. Fera, B. I. Ostrovskii, D. Sentenac, I. Samoilenko, and W. H. de Jeu, Phys. Rev. E **60**, R5033 (1999).

[26] S. Pankratz, P. M. Johnson, R. Hołyst, and C. C. Huang, Phys. Rev. E **60**, R2456 (1999).

[27] E. A. L. Mol, *Fluctuations in freely suspended smectic A films*, PhD thesis, FOM Institute AMOLF, Amsterdam, 1997.

[28] R. Holyst, Phys. Rev. A **42**, 7511 (1990).

[29] E. A. L. Mol, J. D. Shindler, A. N. Shalaginov, and W. H. de Jeu, Phys. Rev. E **54**, 536 (1996).

[30] E. A. L. Mol, G. C. L. Wong, J. M. Petit, F. Rieutord, and W. H. de Jeu, Phys. Rev. Lett. **79**, 3439 (1997).

[31] G. Friedel, Ann. de Phys. (Paris) **18**, 273 (1922).

[32] A. A. Sonin, *Freely suspended liquid crystalline films*, Wiley & sons, Chichester, 1998.

[33] R. Pindak, D. E. Moncton, S. C. Davey, and J. W. Goodby, prl **46**, 1135 (1981).

[34] P. S. Pershan, *Structure of liquid crystal phases*, World Scientific, Singapore, 1988.

[35] P. Pieranski, L. Beliard, J. P. Tournellec, X. Leoncini, C. Furthlehner, H. Dumoulin, E. Riou, B. Jouvin, J.-P. Fenerol, P. Palaric, J. Heuving, B. Cartier, and I. Kraus, Physica A **195**, 364 (1993).

[36] E. I. Demikhov, V. K. Dolganov, and K. P. Meletov, pre **52**, R1285 (1995).

[37] J. Daillant and A. Gibaud, *X-ray and Neutron Reflectivity: Principles and Applications*, Springer Verlag, Berlin, 1999.

[38] M. Tolan, *X-ray Scattering from Soft-Matter Thin Films*, Springer Verlag, Berlin, 1998.

[39] V. Holý, U. Pietsch, and T. Baumbach, *High-Resolution x-ray scattering from thin films and multilayers*, Springer Verlag, Berlin, 1999.

[40] A. N. Shalaginov and D. E. Sullivan, Phys. Rev. E **62**, 699 (2000).

[41] J. Als-Nielsen, D. Jacquemain, K. Kjaer, F. Leveiller, M. Lahav, and L. Leiserowitz, Phys. Rep. **246**, 251 (1994).

[42] L. G. Parrat, Phys. Rev. **95**, 259 (1954).

[43] S. K. Sinha, E. B. Sirota, S. Garoff, and H. B. Stanley, Phys. Rev. B **38**, 2297 (1988).

[44] Jens Als-Nielsen and Des Mc Morrow, *Elements of modern x-ray physics*, Wiley and Sons, Chichester, 2000.

[45] D. L. Abernathy, G. Grübel, S. Brauer, I. McNulty, G. B. Stephenson, S. G. J. Mochrie, A. R. Sandy, N. Mulders, and N. Sutton, J. Synchrotron Rad. **5**, 37 (1998).

[46] Z. H. Cai, B. Lai, W. B. Yun, I. McNulty, K. G. Huang, and T. P. Russel, Phys. Rev. Lett. **73**, 82 (1994).

[47] S. B. Dierker, R. Pindak, R. M. Fleming, K. I. Robinson, and L. Berman, Phys. Rev. Lett. **75**, 449 (1995).

Bibliography

[48] S. G. J. Mochrie, A. M. Mayes, A. R. Sandy amd M. Sutton S. Brauer, G. B. Stephenson, D. L. Abernathy, and G. Grübel, Phys. Rev. Lett. **78**, 1275 (1997).

[49] I. Krauss, P. Pieranski, I. Demikov, H. Stigmeier, and J. Goodby, Phys. Rev. E **48**, 1916 (1993).

[50] J. D. Shindler and R. M. Suter, Rev. Sci. Instrum. **63**, 5343 (1992).

[51] H. Schulte-Schrepping, J. Heuer, and B. Hukelmann, J. Synchrotron Rad. **5**, 682 (1998).

[52] G. Gompper and M. Schick, *Self-Assembling Amphiphilic Systems, Phase Transitions and Critical Phenomena*, Academic, London, 1994.

[53] S. K. Sinha, M. Tolan, and A. Gibaud, Phys. Rev. B **57**, 2740 (1998).

[54] N. Bernhoeft, A. Hiess, S. Langridge, A. Stunault, D. Wermeille, C. Vettier, G. H. Lander, M. Huth, and H. Jourdan Adrian, Phys. Rev. Lett. **81**, 3419 (1998).

[55] A. Gibaud, G. Vignaud, and S. K. Sinha, Acta Cryst. A **49**, 642 (1993).

[56] W. H. de Jeu, J. D. Shindler, and E. A. L. Mol, J. Appl. Cryst. **29**, 511 (1996).

[57] E. Vlieg, J. Appl. Cryst. **30**, 532 (1997).

[58] D. Sentenac, A. N. Shalaginov, A. Fera, and W.H. de Jeu, J. Appl. Crystall. **33**, 130 (2000).

[59] D. Sentenac, A. Fera, R. Opitz, B. I. Ostrovskii, O. Bunk, and W.H. de Jeu, Physica B **283**, 232 (2000).

[60] N. G. V. Kampen, *Stochastic processes in physics and chemistry*, North-Holland, Amsterdam, 1981.

[61] J. Daillant, K. Quinn, C. Gourier, and F. Rieutord, J. Chem. Soc. Faraday Trans. **92**, 505 (1996).

[62] C. Fradin, A. Braslau, D. Luzet, M. Alba, C. Gourier, J. Daillant, G. Gruebel, G. Vignaud, J. F. Legrand, J. Lal, J. M. Petit, and F. Rieutord, Physica B **248**, 310 (1998).

[63] S. Gierlotka, P. Lambooy, and W. H. de Jeu, Europhys. Lett. **12**, 341 (1990).

[64] I. I. Samoilenko, B. M. Shchedrin, and L. A. Feigin, Physica B **221**, 542 (1996).

[65] I. I. Samoilenko, O. V. Konovalov, L. A. Feigin, B.M. Shchedrin, and L. G. Yanusova, Cryst. Rep. **44**, 310 (1999).

[66] D. J. Tweet, R. Holyst, B. D. Swanson, H. Stragier, and L. B. Sorensen, Phys. Rev. Lett. **65**, 2157 (1990).

[67] A. N. Shalaginov and V. P. Romanov, Phys. Rev. E **48**, 1073 (1993).

[68] R. Holyst, Phys. Rev. A **44**, 3692 (1991).

[69] R. Holyst, D. J. Tweet, and L. B. Sorensen, Phys. Rev. Lett. **65**, 2153 (1990).

[70] R. Pindak, D. J. Bishop, and W. O. Sprenger, Phys. Rev. Lett. **44**, 1461 (1980).

[71] E. Dubois-Violette, B. Pansu, P. Davidson, and A. M. Levelut, J. Phys. II France **3**, 395 (1993).

[72] A. Poniewierski and R. Holyst, Phys. Rev. B **47**, 9840 (1993).

[73] A. Caillé, C. R. Acad. Sci. Ser. B **247**, 891 (1972).

[74] L. Gunther and Y. Imry, Phys. Rev. A **22**, 1733 (1980).

[75] L. D. Landau and E. M. Lifshitz, *Theory of Elasticity*, Pergamon, Oxford, 1986.

[76] S. Garg and K. A. Crandell, Phys. Rev. E **48**, 1123 (1993).

[77] W. H. de Jeu and W. A. P. Claassen, J. Chem Phys. **67**, 3705 (1977).

[78] W. H. de Jeu and W. A. P. Claassen, J. Chem Phys. **68**, 102 (1978).

[79] M. R. Fisch, P. S. Pershan, and L. B. Sorensen, Phys. Rev. A **29**, 2741 (1984).

[80] M. Benzekri, J. P. Marcerou, H. T. Nguyen, and J. C. Rouillon, Phys. Rev. B **41**, 9032 (1990).

[81] K. Miyano, Phys. Rev. A **26**, 1820 (1982).

[82] P.S. Pershan, J.D. Litster G. Aeppli, and R.J. Birgeneau, Mol. Cryst. Liq. Crys. **67**, 205 (1981).

[83] J.C. Tarczon and K. Migano, Phys. Rev. Lett. **46**, 1191 (1981).

[84] A. J. Jin, T. Stoebe, and C. C. Huang, Phys. Rev. E **49**, R4761 (1994).

[85] T. Stoebe and C. C. Huang, Int. J. Mod. Phys. B **9**, 2285 (1995).

[86] J. V. Selinger, J. Phys. (France) **49**, 1387 (1988).

Bibliography

[87] R. Holyst, Phys. Rev. B **46**, 15542 (1992).

[88] C. F. Chou, A. Jin, C. Y. Chao, S. W. Hui, C. C. Huang, and J. T. Ho, Phys. Rev. E **55**, R6337 (1997).

[89] W. H. de Jeu et al., *to be published* .

[90] E. A. L. Mol, G. C. L. Wong, J. M. Petit, F. Rieutord, and W. H. de Jeu, Physica B **248**, 191 (1998).

[91] R. Geer, T. Stoebe, C. C. Huang, R. Pindak, G. Srajer, J. W. Goodby, M. Cheng, J. T. Ho, and S. W. Hui, Phys. Rev. Lett. **66**, 1322 (1991).

[92] S. Sprunt, M. S. Spector, and J.D. Litster, Phys. Rev. A **45**, 7355 (1992).

[93] A. Bottger and J. H. Joosten, Europhys. Lett. **4**, 1297 (1987).

[94] A. Poniewierski, R. Holyst, A. C. Price, L. B. Sorenson, S. D. Kelvan, and J. Toner, Phys. Rev. E **58**, 2027 (1998).

[95] A. Poniewierski, R. Holyst, A. C. Price, and L. B. Sorensen, Phys. Rev. E **59**, 3048 (1999).

[96] H. Y. Chen and D. Jasnow, Phys. Rev. E **61**, 493 (2000).

[97] V. P. Romanov and S. V. Ulyanov, Phys. Rev. E **63**, 031706 (2001).

[98] I. Sikharulidze, I.P. Dolbnya, A. Fera, A. Madsen, B.I. Ostrovskii, and W.H. de Jeu, Phys. Rev. Lett. (*submitted*).

Summary

In the smectic A (SmA) phase the elongated molecules are aligned along a particular direction defined by the director (**n**) and arranged in stacks of two-dimensional liquid layers in the direction perpendicular to **n**. The positional order of such smectic layers decays algebraically with distance. Upon cooling a SmA phase, a hexatic smectic B (SmB) phase may occur. It shows long-range bond-orientational order while positional order is limited to a finite correlation length. The centers of mass of the molecules are organized in clusters, which have a triangular lattice in the plane of the layers. The orientations of the clusters possess longer-range ordering, called bond-orientational order. When cooling down a SmB phase, the translational freedom of the clusters disappears and the crystalline B phase (CrB) is formed. This is a truly 3D crystalline phase with long-range positional and orientational correlations in and between the layers. Due to their layered structure, smectic phases can be freely suspended over an aperture in a frame, similar to soap bubbles. In such a film the smectic layers align parallel to the two outermost free surfaces; moreover the film tends to be flat due to the surface tension, which minimizes the surface area. Freely suspended films can be considered as *smectic membranes* consisting of stacks of smectic layers.

Because of their reduced dimensionality, SmA phases are characterized by strong thermal fluctuations. Such fluctuations can be described in terms of the thermally excited elastic modes corresponding to bending and compression of the smectic layers. For the case of SmA membranes, the contribution from the free surfaces is included in the hamiltonian of the system by adding the boundary terms depending on the surface tension. The model predicts that thermal fluctuations can be either damped or enhanced at the free surfaces. Both cases have been confirmed experimentally in the past.

All the experiments presented in this thesis have been carried out on smectic membranes

Summary

of N-(4-*n*-butoxy-benzilidene)-4-*n*-octylaniline, abbreviated as 4O.8. The thermal fluctuation profiles of SmA membranes of various thicknesses measured by *specular* x-ray reflectivity are shown in chapter 4. This technique probes the density modulation along the normal to the smectic layers. The analysis of the specular reflectivity data shows very pronounced thermal fluctuation profiles over the membrane thickness. Moreover, the amplitude of the fluctuations of the central layers diverges with membrane thickness. These results have been compared to *diffuse* x-ray reflectivity experiments by which the in-plane spectral dependence of the thermal fluctuations can be probed. For SmA membranes of various thicknesses the diffuse data can be satisfactorily described by the hydrodynamic theory extended with surface terms. On the other hand, the specular profiles of the thermal fluctuations are more pronounced than predicted by the hydrodynamic theory. In order to explain this discrepancy, a considerable additional contribution from local fluctuations has to be assumed. We also present specular and diffuse reflectivity results for CrB membranes of various thicknesses. The diffuse reflectivity results show a spectral dependence rather similar to the corresponding SmA membranes. Conversely, the profile of the thermal fluctuations through the film shows no dependence on the thickness of the membranes. The results suggest that the CrB membranes are fluctuating dynamically, rather like SmA ones. This can be explained by assuming "easy-shear" of the crystalline layers on top of each other.

SmA membranes of 4O.8 crystallize in a layer-by-layer fashion starting at the outermost interface. Each of the steps is preceded by the formation of an intermediate layer structure with in-plane SmB ordering. In chapter 5 the changes in the thermal fluctuation profile following each crystallization step are shown for eight-layer membranes. We find an unusually large reduction of the fluctuations after the emergence of only one hexatic top layer. The fluctuation profiles through the membrane are quenched at the surfaces. This behavior supports theoretical arguments that the onset of hexatic ordering is hindered by out-of-plane layer fluctuations. After crystallization of the outermost layers, the fluctuations are still quenched at the interface with the solid phase, thus providing the basis for the next crystallization step.

The time dependence of thermal fluctuations has been studied by X-ray Photon Correlation Spectroscopy (XPCS) (chapter 6). We demonstrate the feasibility of XPCS experiments with 8 keV x-rays on relatively thin membranes, for which the relaxation times are in the microsecond range. For SmA membranes, we could resolve both an oscillatory and an exponential damping behavior of the intensity-intensity correlation function. This contrasts with thick film results

reported in the literature for which only a simple exponential decay was found. The oscillatory behavior can be attributed to inertial effects that become pronounced for thin membranes. In agreement with these theoretical predictions we observed a transition to exponential decay as a function of membrane thickness. Finally, XPCS of CrB membranes shows similar results as for SmA. This proves the dynamic nature of the thermal fluctuations in this 3D-ordered phase.

Summary

Samenvatting

In de smectische A (SmA) fase wijzen de langwerpige moleculen in een specifieke richting, gedefinieerd door de vector (**n**), en zijn ze geordend in stapels van twee-dimensionale vloeibare lagen in de richting loodrecht op **n**. De positionele ordening van zulke smectische lagen valt algebraïsch af met afstand. Wanneer een SmA fase wordt afgekoeld, kan een hexatische smectische B (SmB) fase optreden. Deze vertoont een lange afstands band-oriëntatie ordening terwijl positionele ordening is gelimiteerd tot een eindige correlatie-lengte. De massamiddelpunten van de moleculen zijn georganiseerd in clusters, die een driehoekig rooster in het vlak van de lagen hebben. De oriëntaties van de clusters hebben lange afstands ordening, band-oriëntatie ordening genaamd. Als een SmB fase wordt afgekoeld, verdwijnt de translationele vrijheid van de clusters en wordt de kristallijne B (CrB) fase gevormd. Dit is een echte 3D kristallijne fase met lange-afstands oriëntationele and positionele correlaties in en tussen de lagen. Als gevolg van de gelaagde structuur, kunnen smectische fases vrij opgehangen worden aan een frame, zoals zeepbellen. In zo'n film richten de smectische lagen zich parallel aan de buitenste vrije oppervlakken; bovendien neigen de films er naar plat te zijn door de oppervlaktespanning, die het oppervlak minimaliseert. Die soort van films kunnen beschouwd worden als *smectische membranen* die bestaan uit stapels smectische lagen.

Als gevolg van de gereduceerde dimensionaliteit, worden SmA fasen gekarakteriseerd door sterke thermische fluctuaties. Zulke fluctuaties kunnen beschreven worden in termen van de thermisch aangeslagen elastische modes die overeenkomen met buiging en compressie van de smectische lagen. In het geval van de SmA membranen, wordt de bijdrage van de vrije oppervlakken verdisconteerd in de Hamiltoniaan van het systeem door de randvoorwaarden die afhangen van de oppervlaktespanning. Het model voorspelt dat thermische fluctuaties ofwel gedempt ofwel versterkt worden bij de buitenste oppervlakken. Beide gevallen zijn in het verleden experimenteel bevestigd.

Samenvatting

Alle experimenten gepresenteerd in dit proefschrift zijn uitgevoerd op smectische membranen van N-(4-*n*-butoxy-benzilideen)-4-*n*-octylaniline, afgekort als 4O.8. De thermisch fluctuatie profielen van SmA membranen van verschillende diktes, gemeten met *speculaire* röntgenreflectiviteit, worden getoond in hoofdstuk 4. Deze techniek meet de dichtheidsmodulatie langs de normaal op de smectische lagen. De analyse van de experimentele data toont uitgesproken thermische fluctuaties profielen door de membraandichtheid. Bovendien divergeert de amplitude van de fluctuaties van de centrale lagen met membraan-dikte. Deze resultaten zijn vergeleken met *diffuse* röntgenreflectiviteit experimenten, waarmee de spectrale afhankelijkheid van de thermische fluctuaties in de richting van het oppervlak gemeten kunnen worden. Voor SmA membranen van verscheidene diktes kan de data bevredigend worden beschreven met de hydrodynamische theorie uitgebreid met oppervlakte termen. Aan de andere kant, zijn de speculaire profielen van de thermische fluctuaties meer uitgesproken dan voorspeld door de hydrodynamische theorie. Om deze discrepantie te verklaren, moet een aanzienlijke additionele bijdrage van locale fluctuaties aangenomen worden. We presenteren ook resultaten van speculaire en diffuse reflectiviteitsexperimenten voor CrB membranen van verschillende diktes. De diffuse reflectiviteit experimenten tonen een spectrale afhankelijkheid die tamelijk gelijk is aan die van SmA membranen. Daarentegen toont het profiel van de thermische fluctuaties door de film geen afhankelijkheid van de dikte van de membranen. De resultaten wijzen erop dat CrB membranen dynamisch fluctueren, net als de SmA membranen. Dit kan verklaard worden door *easy-shear* van de op elkaar liggende kristallijne lagen te veronderstellen.

SmA membranen van 4O.8 kristalliseren op laag-voor-laag, beginnend bij de buitenste. Elke stap wordt voorafgegaan door de vorming van een tussen structuur met SmB ordening. In hoofdstuk 5 worden de veranderingen in het thermisch fluctuatie profiel getoond die volgen op elke kristallisatie stap voor membranen van acht lagen. We vinden een ongewoon grote afname van de fluctuaties na het ontstaan van maar één enkele hexatische bovenlaag. De fluctuatie profielen door het membraan zijn gedempt aan de oppervlakken. Dit gedrag ondersteunt het theoretische argument dat het begin van hexatische ordening belemmerd wordt door fluctuaties in de richting loodrecht op het vlak. Na kristallisatie van de buitenste lagen, zijn de fluctuaties nog steeds gedempt op het grensvlak, waarmee een basis voor de volgende kristallisatiestap verschaft wordt.

De tijdsafhankelijkheid van thermische fluctuaties is bestudeerd met *X-ray Photon Correlation Spectroscopy* (XPCS) (hoofdstuk 6). We laten haalbaarheid van XPCS experimenten met

8 keV straling op relatief dunne membranen, waarvoor de relaxatietijden in het microseconde domein liggen zien. Voor SmA membranen konden we zowel oscillatoir als exponentieel dempingsgedrag onderscheiden van de intensiteit-intensiteit correlatiefunctie. Dit staat in contrast met experimenten op dikke films in de literatuur waar alleen exponentieel dempingsgedrag geobserveerd werd. Het oscillatoir gedrag kan worden toegeschreven aan inertia effecten die belangrijk worden voor dunne membranen. In overeenstemming met deze theoretische voorspellingen observeren wij een overgang naar exponentieel verval als functie van membraan-dikte. Tot slot geven XPCS experimenten op CrB membranen dezelfde resultaten als die op SmA membranen. Dit bewijst dat de thermische fluctuaties in deze 3D geordende fase dynamisch zijn.

Samenvatting

Acknowledgements

During my PhD project I had the chance to interact with lots of people, from many different countries. It is almost impossible to thank them all, so that if I fail to mention your name, remember: this does not mean I am less grateful ... !!!

I would like to thank my supervisor, Prof.dr.ir. Wim H. de Jeu, for the careful guidance in these years, for his keen sense of timing and assessing valuable projects worthwhile to be investigated, and for his unsurpassed discipline that he was able to impose on this rebel student.

I profited very much from the close collaboration with Dr. Boris I. Ostrovskii, who not only was able to discuss with me many secrets of soft-condensed matter thanks to his vast knowledge and experience, but who also always succeeded in making me forget the clock and keep listening and learning from him. Finally, I feel the need to thank him for never altering his quiet expression with a smile for one of the many stupid questions that suddenly, in a burst of excitement, I dared to bother him with.

I always was very happy to listen and learn from Dr. Arcadi N. Shalaginov, who was able in a few words to disentangle for me the secrets of his models, and was always there when I needed another explanation.

Shorter, but certainly not less important, were also the collaborations with Dr. Ivan Samoilenko and Dr. Alexei Val'kov. I would also like to thank Dr. Liesbeth Mol and Dr. Daniel Sentenac for their important contributions in the earlier stages of my PhD project.

Without the valuable and creative technical support of Ernst Prins and, before him, of Jan Commandeur, some of the experiments reported in this thesis simply would not be present. I also wish to acknowledge Wim Brouwer, Wim Barsingerhorn and all the staff of the AMOLF workshop.

I would like to thank Prof.dr. Harm Geert Muller for his inventive collaboration in the first XPCS experiment reported here, and to have revealed to me some of the deepest secrets of time-correlators. This line of research was taken over extremely successfully and promisingly about

Acknowledgements

Curriculum Vitae

Andrea Fera was born the sixth of March 1972 in Cagliari, Italy. He obtained in 1995 a degree in Chemistry at the Department of Analytical Chemistry of the University of Cagliari, with a thesis on the resistance to corrosion of metallic amorphous alloys, under the supervision of Prof.dr. A. Rossi and Prof. D. de Filippo. Between August 1995 and August 1996 he spent a year of compulsory civil service in Italy. In January 1997 he started studying liquid crystalline membranes by means of x-ray reflectivity techniques for his PhD, at the FOM- Institute for Atomic and Molecular Physics, in Amsterdam (NL), under the supervision of Prof.dr.ir. W.H. de Jeu. The results of this research are published in this thesis. In January 2002 he will begin a 2-year project granted by a Marie-Curie Fellowship of the European Community at the Institut Curie in Paris. The project aims at understanding the modifications in the fluctuations spectrum of lamellar vescicles when the incorporated proteins are active.